CALIFORNIA STATE UNIVERSITY, NORTHRIDGE

RAYLEIGH WAVE PHASE VELOCITIES BENEATH THE OCEANIC AND CONTINENTAL MARGIN OF THE NORTH AMERICAN AND PACIFIC PLATE BOUNDARY

A thesis submitted in partial fulfillment of the requirements
For the degree of Master of Science in Geology,
Geophysics

By

Lennin de Jesus Escobar

December 2013

The thesis of Lennin de Jesus Escobar is approved:

Dr. Monica Kohler	Date
Dr. Gerald Simila	Date
Dr. Dayanthie Weeraratne, Chair	Date

California State University, Northridge

TABLE OF CONTENTS

SIGNATURE PAGE……ii

TABLE OF CONTENTS iii

List of Figures v

ABSTRACT vi

Chapter 1 Introduction 1

1.1 Motivation 1

1.2. Tectonic Background 2

1.3. Previous work deep ocean 9

Chapter 2 Seismic Data 13

2.1 OBS Deployment and Retrieval 13

2.2 Land Stations 15

2.3 Data Corrections 15

2.4 Earthquakes 18

Chapter 3 Surface Wave Method 21

Chapter 4 Results 24

4.1 Phase velocity results 24

4.1.1 1-D uniform phase velocity results 24

4.1.2 Phase velocity in 3 regions 27

4.2 2-D maps 28

4.2.1 Lateral velocity variations in continental California 31

4.2.2 Lateral velocity variations in the Borderland 32

4.2.3 Lateral velocity variations in the deep seafloor 32

4.3 Anisotropy results 34

4.3.1 Average anisotropy 34

4.3.2 Anisotropy in three regions 35

Chapter 5 Discussion 39

5.1 Velocity structure in the deep seafloor 39

5.2 Oceanic versus continental lithosphere 40

5.3 Velocity structure in the Borderlands 41

5.4 San Andreas, Garlock, and Murray transform faults 41

5.5 The Western Transverse Ranges 42

Chapter 6 Conclusion 44

References 45

Appendix A: Amplitude Correction Plots 49

Appendix B: 2D Maps 64

Appendix C: Seismograms 78

List of Figures

Figure 1.1 Simplified map of the Borderlands 4

Figure 1.2 Seafloor magnetic isochron map 12

Figure 2.1 ALBACORE OBS deployment area 13

Figure 2.2 Behavior of amplitudes with increasing depths 17

Figure 2.3 Azimuthal distribution of earthquakes 19

Figure 2.4 Ray path coverage for the study area 20

Figure 3.1 Grid node configuration 23

Figure 4.1 Average phase velocity as a function of period 26

Figure 4.2 Average phase velocity as a function of period in three regions 28

Figure 4.3 Phase velocity maps 30

Figure 4.4 Average anisotropy as a function of period 34

Figure 4.5a Anisotropy deep seafloor 36

Figure 4.5b Anisotropy in the Borderland 36

Figure 4.5c Anisotropy in the land 37

Figure 4.6 Phase residuals as a function of period 38

ABSTRACT

RAYLEIGH WAVE PHASE VELOCITIES BENEATH THE OCEANIC AND CONTINENTAL MARGIN OF THE NORTH AMERICAN AND PACIFIC PLATE BOUNDARY

BY

Lennin de Jesus Escobar

Master of Science in Geology, Geophysics

The Pacific-North America plate boundary, located in Southern California, presents a unique opportunity to study tectonic stability and deformation of the Pacific and North America plates from a migrating oceanic spreading center and its subduction beneath the North American plate up until 30 Ma (Atwater, 1989). The ongoing rotation of the Transverse ranges and Borderlands following this event make this an active plate boundary that presents tectonic stresses and seismic hazards for the local area. I consider offshore seismometer coverage to the west side of the plate boundary system. I use Rayleigh waves recorded by an array of 34 ocean bottom seismometers deployed offshore southern California for 12 month duration from August 2010 to September 2011. The array recorded teleseismic earthquakes filtered for 16 s – 78 s at distances ranging from 30° to 120° with good signal-to-noise ratios for magnitudes Mw ≥ 5.8. The inversion technique considers non-great circle path propagation by representing the arriving wave field as two interfering plane waves. Phase velocities averaged over the study area are 1.3% lower than the velocities found by other surface wave studies of a seafloor ages of 20-52 Ma. Phase velocities offshore southern California in the oceanic mantle align in the N-S direction and show increasing velocities with older seafloor ages to the west at periods of up to 45 s. At 55 s, the velocity structure changes to an E-W

alignment indicating a transition from oceanic lithospheric below 40 s (53 km depth) to asthenospheric mantle flow aligned with Pacific plate motion above 55 s (73 km depth).). Variations in the N-S pattern of velocities that increase with age indicate a slightly sinusoidal pattern consistent with spacing between offshore fracture zones that suggests these surface features involve deformation at lithospheric depths to at least 50 km. Anisotropy is consistent with Pacific plate motion, N 78.5˚ W, in a NW-SE direction for all regions in my study area, except for the periods above 40 s in the Borderland where anisotropy demonstrates N-S alignment. Phase velocities at lithospheric depths are 5 % higher in the oceanic mantle compared to the continental mantle indicating compositional and structural differences due to formation history in the two tectonic environments.

Chapter 1 Introduction

1.1 Motivation

The plate boundary between the Pacific plate and the North American plate in southern California presents a very unique opportunity to study the tectonic interaction of a spreading center and a trench. The East Pacific Rise migrated around 30 million years ago eastward to the subduction zone located at the western margin of the North American plate (Atwater, 1989). The spreading center itself was subducted beneath the continental plate. This tectonic event also marked a change from a convergent zone to a transform boundary (Atwater, 1970). This created one of the few examples of a transform fault on land which separates an offshore oceanic and continental plate. Formation of the San Andreas fault was later followed by a rotational event that translated the N-S oriented coastal Peninsular ranges over 90° in a counter wise (CW) direction to form the E-W trending Transverse Ranges we see today (Luyendyk, 1991). It is not clear whether the Transverse range structure extends offshore beyond the coastline. This tectonic rotation is responsible for the opening of the Borderland continental margin, as well as a series of fracture zones west of the Patton escarpment. Geodedic measurements indicate rotation is still active today.

Much work has been done to understand the tectonic evolution of this active region on the continental side of the plate boundary which is now a highly populated urban region including the Los Angeles metropolitan area. Little is known about the oceanic plate offshore due to limited access to deep water and marine instrumentation. Thus tectonic events such as plate-scale deformation and onshore-offshore fault stresses are not well understood across the plate boundary. Here I present seismic results from a marine

deployment of 34 ocean bottom seismometers offshore southern California, the ALBACORE (Asthenospheric and Lithospheric Broadband Architecture from the California Offshore Region Experiment) project, to study the west side of the Pacific-North America plate boundary. Recent studies (Legg et al., 2012) from new bathymetry data offshore (from the ALBACORE project) indicate at least two major sets of faults offshore that mimic the shape and bend of the San Andreas and may indicate seismic hazards offshore as well as on land. Understanding the tectonic structure of the crust, lithosphere, and plate motion stresses identified by off-shore, seismic surface wave tomography may help understand the points of seismic risk.

1.2. Tectonic Background

The tectonic reconstruction of the seafloor was studied in previous work from magnetic lineations (Engebretson et al., 1984, Atwater, 1989). At about 110 Ma the East Pacific Rise (EPR) was an active spreading center in the central Pacific that divided the Pacific and Farallon plates (Atwater, 1989). The oldest edge of the Farallon plate was simultaneously subducting beneath the western margin of North America at a rate faster than it was spreading at the EPR, causing eastward migration of the spreading center (Atwater, 1989).

The Pacific plate grew and the Farallon plate diminished in size as the Farallon plate moved the NE direction and was subducted. In the late Cretaceous, about 80 Ma, the Farallon plate fractures, designating the Kula plate in the north Pacific seafloor and begins to subduct beneath northern Canada and the Aleutian island trench (Atwater, 1989). The Kula plate remained intact until the Eocene when the last portion of it was subducted. The Farallon plate continued moving to the east until about 55 Ma, when it

experienced its first disruption documented by the abrupt change in direction of the Surveyor, Mendocino, and Pioneer fracture zones (Atwater, 1989). This change is interpreted as the breakup of the northern portion of the Farallon, which continued to migrate to the north and later became the Vancouver plate (Atwater, 1989). Then, during the late Eocene, about 37 Ma, the western side of the North American plate was reorganized again. The EPR spreading center reached the trench of the western margin of the North American plate near Baja and southern California and began subducting (Atwater, 1989). This event also initiated a transform fault on land marking the beginning of the San Andreas Fault (Atwater, 1989). In the middle Miocene, at about 17 Ma, the western Transverse Ranges (WTR) begin to rotate in a CW direction when the Pacific-North American plate boundary zone sheared dextrally and extended as the Pacific plate moved northward with respect to North America (Luyendyk, 1991). The total rotation is at least 93° and the WTR is oriented in EW direction today. It is not clear whether the WTR continues offshore to the south or west across the coastline.

Convergence along the edge of North America during Mesozoic and Paleogene time created an active arc-trench system (Crouch and Suppe, 1993), which included the Franciscan accretionary wedge, the underlying Coast Range ophiolites, the Great Valley forearc-basin sequence, the accreted arcs and mélanges of the Western Foothills belt, and the magmatic arc of the Sierra Nevada-Peninsular ranges, (Crouch and Suppe, 1993). Disruption of central California took place in the Cretaceous, during the subduction event including rotation of the WTR, opening of the Los Angeles basin and the Borderland region offshore southern California (Atwater, 1970, 1989).

The present configuration of the California Borderland consists of four main geologic belts which divide the zone into the western Transverse Ranges block, the Patton accretionary belt and Nicholas forearc belt (Outer Borderland), and the Catalina Schist belt (the Inner Borderland) (Figure 1.1) (Bohannon and Geist, 1998).

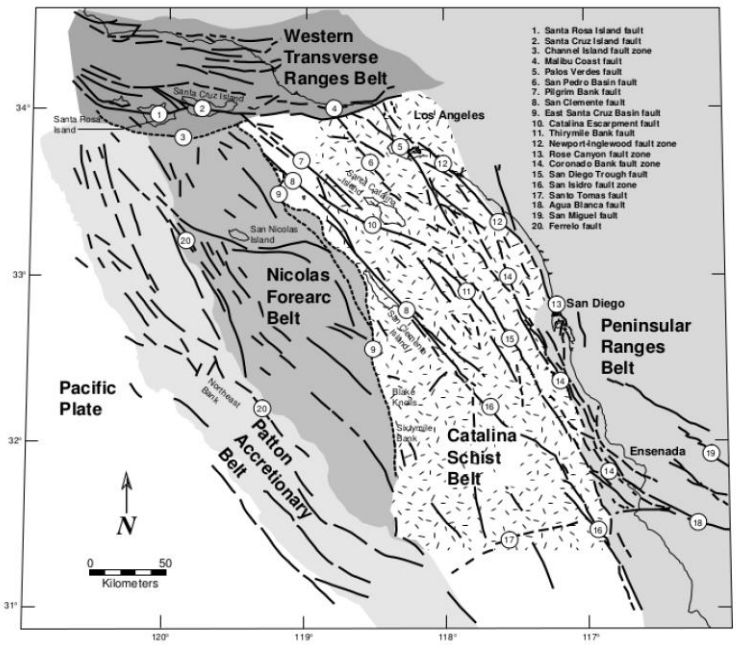

Figure 1.1: Simplified map of the main geologic structures found in the California Borderland. (Bohannon and Geist, 1998).

The tectonic evolution of California's borderland began in early Miocene after the subduction of the Farallon plate beneath the North America plate (Atwater, 1989). At this instance, relative motions between the Pacific and North American plates over the transform boundary had induced horizontally transmitted stress from one plate to another across a wide zone of deformation that includes the Borderland (Atwater, 1970). Major tectonic events during the middle Miocene such as the cessation of subduction fragment under California and the capture of the Monterrey fragment at 20-18 Ma. as well as the subduction of the Arguello fragment until approximately 17.5 Ma. (Nicholson et al.,

1994) marked a time that was characterized by extension and rifting.

The Catalina Schist was uplifted from middle crustal levels and exposed during a major event of extensional tectonism that started in early-middle Miocene time along with about 100° of CW rotation of the WTR belt causing the displacement of the Nicolas forearc belt to the west (Bohannon and Geist, 1998; Luyendyk, 1991). The rotation of the WTR and the translation of the Nicolas forearc belts are associated with a large amount of uplift that it probably involved strong footwall flexural deformation (Bohannon and Geist, 1998). Extension in the Borderland continued during and after middle Miocene and as a result most of the Borderland was further deformed into numerous ridges and basins during this stage of oblique extension (Bohannon and Geist, 1998).

Numerous studies have been done to determine the crustal and lithospheric thicknesses as well as investigate the crustal-upper mantle structure and current mantle flow beneath the continental side of the plate boundary in southern California. Studies using iteration of thermalmechanical models (Saleeby, 2012; Gilbert, 2012) predict the process of delamination of the arclogite root of the Sierra Nevada batholith is in progress. On the other hand, crustal thickness is estimated (Zhu and Kanamori, 2000; Kohler and Davis, 1997) using teleseismic travel time residuals from the LARSE experiment which determined a crustal thickness of 40 km beneath the San Gabriel Mountains (Zhu and Kanamori, 2000; Kohler and Davis, 1997). Results from teleseismic receiver function modeling estimate a crustal thickness of 29 km beneath the central Transverse Ranges. The Inner Continental Borderland (ICB) is found to have a crustal thickness of 19 to 23 km (ten Brink et al., 2000). The crustal thickness at the continental margin beneath the Los Angeles basin decreases rapidly over a short distance from 30 km under the

Transverse Ranges to about 20 km beneath the ICB (Zhu and Kanamori, 2000). The location of this transition spans a width of 20-25 km with 13 km of this section existing offshore (Nazareth and Clayton, 2003).

Lithospheric thickness was estimated recently by surface waves studies (Yang and Forsyth, 2006a) showing that lithospheric thickness beneath southern California is approximately 90 km. Studies from P wave travel time inversions indicate that the thickness of the lithosphere under the San Gabriel Mountains and San Andreas fault is 60-80 km (Kohler, 1999). A more recent study, which uses scattering of teleseismic shear waves, indicate important variations in the lithosphere-asthenosphere boundary (LAB) (Lekic et al., 2011). The study reveals an abrupt change in lithospheric thickness from approximately 70 km beneath the Los Angeles Basin to 50 km under the Inner Borderland. Likewise, a transition from the western Transverse Ranges into the Inner Borderland exhibits an LAB shallowing of approximately 20 km. The study also images a thicker lithosphere of approximately 90 km for the Outer Borderland. Recent work by using P to S converted phases identify a Moho signature at 19 km (+/- 2 km) in the ICB and 30 km (+/- 4 km) in the OCB (Reeves et al., 2013). Rotation of the Transverse Ranges was first identified by paleomagnetic observations.(Luyendyk, 1991). Seismic studies using inversion of teleseismic P travel-time residuals later found evidence for a CW rotation of a high velocity anomaly with increasing depth from an EW orientation at a depth of 50 km to NNE-SSW at a depth of 190 km (Kohler et al., 2003). Seismic anisotropy studies using measurements of SKS splitting indicate that the fast polarizations directions for stations east of the San Andreas including the Mohave Desert area are roughly E-W (80-95° east of north) (Liu et al., 1995). Stations west of the San

Andreas (including regions south of the Great Valley) appear to shift to a NE-SW azimuth (approximately 53° east of north) over the southern end of the Great Valley. Anisotropy is 82° east of north, in the western Transverse Ranges and northern Peninsular Ranges, 94° east of north in the Mojave Desert, and 70° east of north on San Clemente Island. Results from SKS splitting measurements show that fast polarization directions are approximately E-W across a broad area in southern California (Polet and Kanamori, 2002) and is consistent with azimuthal anisotropy from surface wave studies averaged over southern California (Yang and Forsyth, 2006a). On the other hand, close to the Santa Barbara bay area, the fast velocities exhibit a NW-SE direction and WNW direction over the region of the Channel islands; southern of the Santa Barbara bay, (Polet and Kanamori, 2002). A recent combined study of SKS and surface wave splitting predicts N112^{o}W for Rayleigh wave fast directions for the lithosphere in a depth range of 33-100 km (Kosarian et al., 2011). According to this finding, the direction of anisotropy from surface waves is approximately parallel to the San Andreas Fault, a result that contrasts with the N80^{o}E fast direction for SKS splitting fast directions from the same study. The study suggests that at least two layers of anisotropy are required to explain the contrast between the results, the first in the depth range of 33-100 km (mantle lithosphere), and a second in a depth range of about 300-400 km. The contrasting pattern suggests, therefore, that anisotropy for southern California twists in a CCW direction with increasing depth (Kosarian et al., 2011).

Mantle flow offers good insight into plate tectonic behavior at this plate boundary as well as the lithospheric structure and stability in general. Silver and Holt (2002) using surface motion and mantle deformation data from Global Positioning System (GPS) and

seismic anisotropy respectively, find that mantle flow is only weakly coupled to the motion of the surface plate which produces a small drag force. Another study done by Zandt and Humphreys (2008), which uses seismic tomography and kinematic reconstruction based on plate velocity and anisotropy, states that a toroidal mantle flow is present beneath a wide region of western North America. The mantle flow spans ~1000 km in diameter including Nevada, Utah, Arizona, southern Oregon, and California driven by plume flow around the plate edge or remnants of Farallon plate subduction. This toroidal pattern predicts flow in the NW-SE direction offshore southern California. Whether plate velocity is dictated by absolute plate motion (APM) of the Pacific plate (55° NW), the North America plate (63° SW) or rotation, studies of shear traction suggests that the lower mantle will respond actively to mantle drag (e.g. Liu and Bird, 2002). Other studies indicate that the anisotropy pattern observed in southern California is a direct result from the alignment of the a-axis of olivine crystals (E-W fast directions), nearly perpendicular to the World Stress Map vectors (N-S direction) of lithospheric shortening (Polet and Kanamori, 2002), whereas (Kosarian et al., 2011), suggests SKS splitting is due to drag on the asthenosphere by the absolute plate motion of the overriding plates. In summary, the geodynamic models predict that the dominant direction of anisotropy in our OBS stations in the Borderland and deep ocean should be E-W and NW-SE respectively. The latter is expected to be consistent with previous predictions for pure Pacific plate motion (N 55° W).

I present results from Rayleigh wave analysis of marine and land based data filtered from 16 s – 78 s using 48 earthquake events to obtain Rayleigh phase velocities and azimuthal anisotropy results to differentiate between the geodynamic models described

above. I have found that phase velocities for periods above 40 s are 1.3% lower than previous studies (Nishimura and Forsyth, 1988) which may indicate a difference in seafloor age considered in their (20-52 Ma) of their study. I find that 2-D tomography results show that the Sierra Nevada range has a very deep structural root to at least 100 km depth. Azimuthal anisotropy averaged over the study area indicates fast directions which are parallel to Pacific plate motion, N 78.5˚ W. Fast directions in the Inner Continental Borderland demonstrate a change to N-S alignment at periods longer than 40 s. Higher velocities are observed at long periods which sample the oceanic mantle compared to the continental mantle indicating a difference in structure that may be related to formation history of the lithosphere in the two environments.

1.3. Previous work deep ocean

A model of sea-floor-spreading (Hess, 1962) reveals that the structures of the Pacific basin were basically formed due to normal growth and cooling during propagation of the sea-floor from a spreading ridge. The oceanic lithosphere is formed as a part of plate tectonic cycle in which new oceanic lithosphere is created by the upwelling and partial melting of material from the asthenosphere at the oceanic spreading ridges. Once the oceanic lithosphere is formed, it cools as it spreads away from the ridge and is reheated when it returns to the mantle at subduction zones. Two models have been postulated to account for the variation in depth and heat flow with increasing age as oceanic lithosphere cools. One model, the simple cooling model, states that the lithosphere behaves as the cold upper boundary layer of a cooling halfspace which predicts a linear relation between depth and $age^{1/2}$, or heat flow and $age^{-1/2}$ of the ocean floor (Turcotte and Schubert, 2002). The second, the Plate model, states that the lithosphere is treated as a

cooling plate with an isothermal lower boundary, where it cools conductively until it reaches a predetermined limit. According to the Plate model, the plate thickness has an asymptotic thermal thickness of 125 km for the Pacific oceanic lithosphere (Parsons and Sclater, 1977; Stein and Stein, 1992). According to the conductive cooling models the seafloor subsides and cools conductively until approximately 80 Ma where data from bathymetry, gravity and heat flow data indicate a departure from this prediction.

Several studies have identified the variation in phase velocities with age. The MELT experiment, for example, indicates that the change in average phase velocity from the youngest sea floor, less than 4-5 Ma, to the average phase velocity in the next age zone is two times larger than could be explained by conductive cooling of the mantle (Harmon et al., 2009). Rayleigh wave studies show that phase velocity increases, moving away from the ridge, with increasing age with a minimum of 3.68 km/s at 25 s (Forsyth, 1998). Another study from the Glimpse experiment finds that the phase velocities are higher for seafloor ages between 5-9 Ma. with minimum values of 3.78 km/s at periods between 20-40 s (Weeraratne et al., 2007). Previous studies in the Pacific also indicate that Rayleigh wave phase velocities increase as a function of age. Phase velocity values range between 3.94 - 4.16 km/s for a period range of 20-125 s and ages between 20-52 Ma (Nishimura and Forsyth, 1989).

The study area discussed here covers an oceanic lithosphere region characterized by complex breakup and fracture of the Pacific plate near shore where at least one fracture zone is found offshore. Transform faults which delineate the Monterey, Morro, Arguello and Patton fracture zones are indicated by deformed magnetic anomalies show offshore deformation following subduction of the EPR spreading center. My study also covers

oceanic seafloor far to the west that is not fracture and has formed at a uniform rate that should follow the conductive cooling models for lithospheric formation. The overall range of ages for the area is between 18-32 Ma. with an unknown lithospheric thickness. However, a previous Pacific ocean study; the GLIMPSE study (Weeraratne et al., 2007), carried out on young sea-floor (5-9 Ma.) west of the East Pacific Rise using Rayleigh wave dispersion suggests the area to have a thicker lithosphere of ~40 km than the lithosphere observed near the EPR (~20 km) indicating lithospheric growth with increasing sea-floor age.

The Murray Fracture Zone is defined as a series of fault scarps extending across the Pacific from the outer Hawaiian Ridge toward the California coastline. This fracture is a linear feature which separates two distinctly different areas of sea floor (Huene, 1968) The fracture zone can be dated by means of paleogeographic reconstruction of the late Cretaceous-Early Tertiary coastal sequence which suggests that the formation of the Murray Fracture Zone was later than Late Cretaceous time, but no later than middle Eocene time (Yeats, 1968). The fracture zone is mainly characterized by an age offset which is observed from the magnetic lineations (Figure 1.2) that is slightly older on the north side compared to the south side of the fracture (Atwater, 1989). Areas of thicker lithosphere or colder material are expected to be found on the north side of the Murray Fracture zone, whereas areas of thinner lithosphere are expected to be found on the south side.

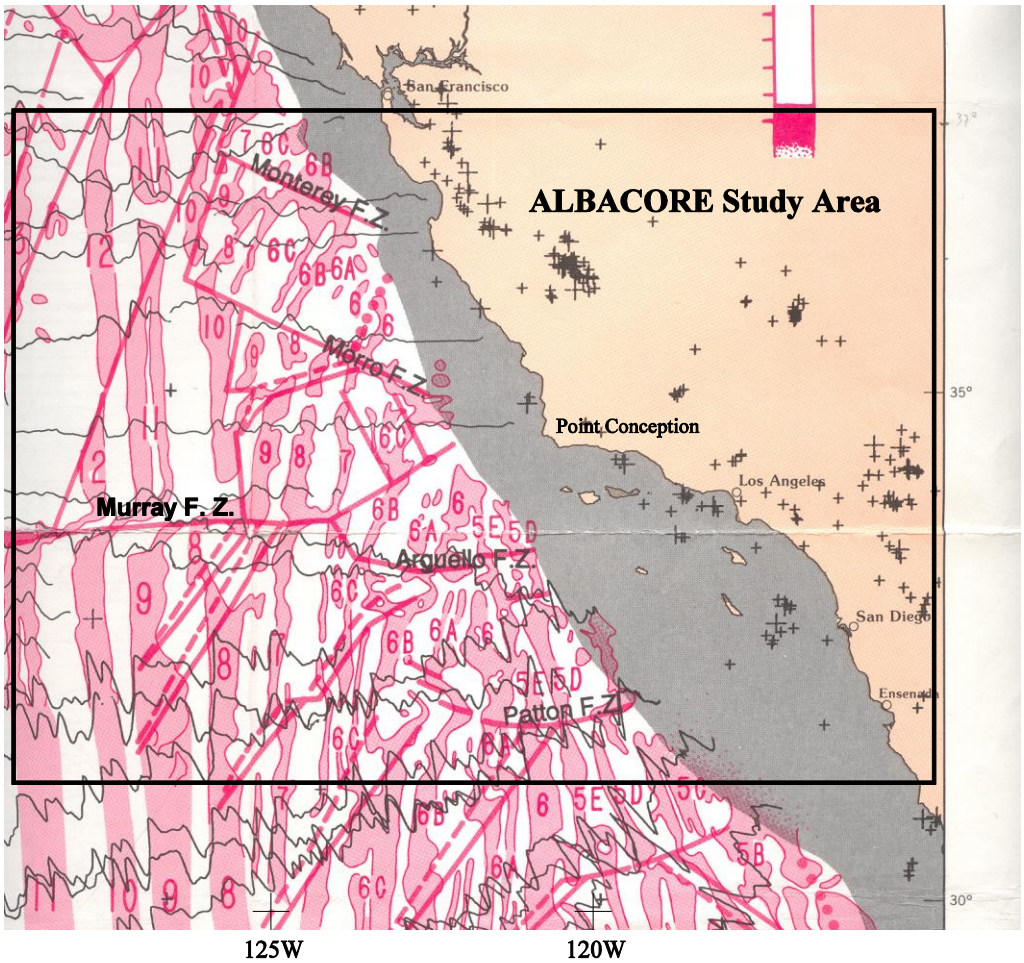

Figure 1.2: Seafloor magnetic isochron map (Atwater, 1989). Black box shows the study area for our marine seismic deployment.

Chapter 2 Seismic Data

2.1 OBS Deployment and Retrieval

The ALBACORE experiment involved collection of seismic data from a long-term teleseismic deployment of 34 ocean bottom seismometers (OBSs) recording from August 2010 to September 2011. The seismic array consisted of 24 long-period (LP) OBSs and 10 short- period (SP) OBSs which were deployed in an array 150 km north-south by 400 km east west off the coast of southern California (Figure 2.1).

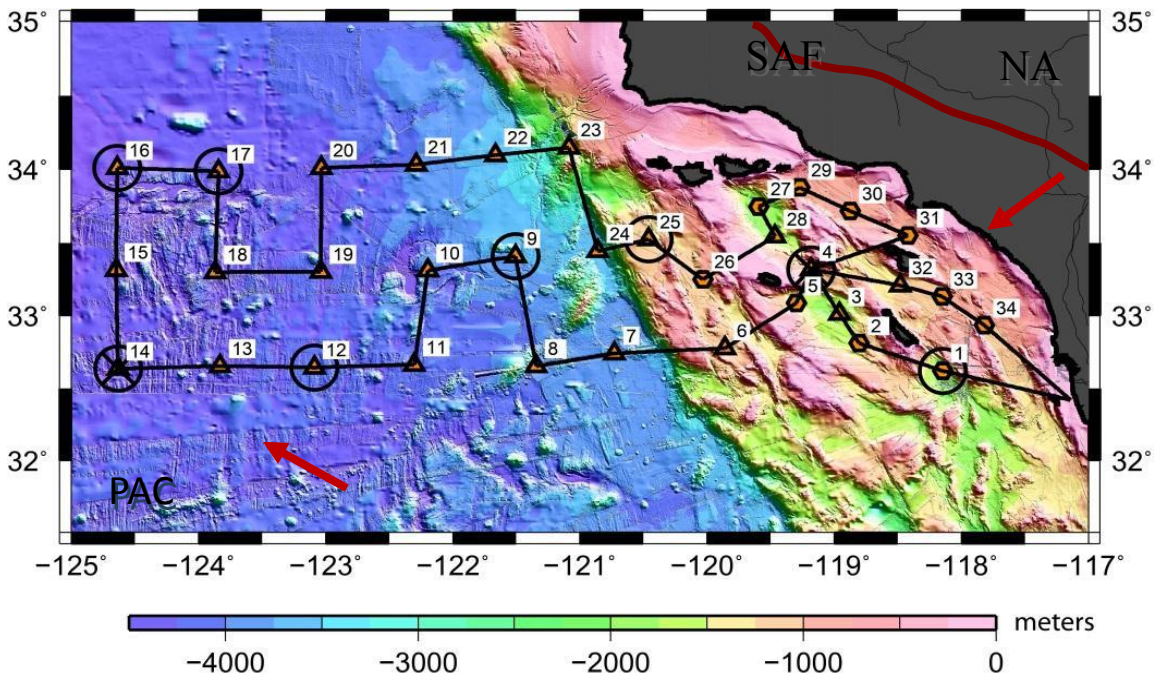

Figure 2.1: ALBACORE OBS deployment area with bathymetry compiled by N. Shintaku (2010, AGU abstract). Ship tracks shown for Sept. 7-16, 2011 recovery cruise on the R/V New Horizon. Bathymetry is a compilation of ship track data sets from the NGDC, USGS, 2010 ALBACORE deployment cruise (Shintaku et al., 2010, AGU abstract), and global data (Smith and Sandwell, 1997). Circles indicate stations with limited or no seismometer data. Coastlines are outlined in black and gray including the Channel Islands. Red arrows represent the absolute plate motion vectors. Red line on the NE quadrant marks the approximate location of the SAF. Triangles and hexagons represent long period and short period instruments respectively.

The seismic instruments used in this experiment consisted of three types, 21 long-period (LP) Trillium T-240 sensors, 3 long-period (LP) Trillium T-40 sensors, and 10 short-period (SP) Sercel L-28 sensors. All LP instruments were equipped with differential pressure gauges (DPGs) and all SP's included a hydrophone. All the OBS stations were set to record at a sample rate of 50 samples per second (sps) (Kohler, 2010, cruise report).

The cruise for the deployment phase took place on R/V Melville from the San Diego port. The instrument locations were selected such that the station spacing was approximately uniform. In shallow-water in the Continental Borderland region, station spacing was approximately 50 km, and on deeper-water seafloor, the station spacing was approximately 75 km. The depth range for the OBSs was between 1000 and 4500 m which was designed deliberately to avoid biological and sediment interference and to reduce the risk of instrument loss and damage as well as noise from shallow-water currents.

For the recovery phase, the cruise took place on R/V New Horizon and it departed out of San Diego on September 7 in 2011 and arrived back in San Diego on September 16 in 2011. During this process the team was able to recover only 32 out of 34 OBSs. Station OBS 14 was never recovered successfully due to problems with communication likely due to damage of glass flotation balls during deployment in the high pressure deep water of this deep location (4374 m). Station OBS 4 communicated successfully but would not release from the seafloor possibly due to sediment burial or other obstruction. Although 32 OBSs were recovered; only 26 seismic stations produced useful data. Stations OBS 25, 16, 12, and 9 did not record any seismic data from the sensors. Station OBS 17 only recorded the first 3 months of data. I obtained 76% total data return from the marine

deployment.

2.2 Land Stations

In this study, I combined our OBS stations with land stations from a permanent network in western California and on the Channel Islands. I use 82 land stations from the California Integrated Seismic Network (CISN) between -116° to -125° longitude and 32.5^{o} to 37.5^{o} latitude (Figure 2.4). Seven of these stations were operating on the Channel Islands during our experiment. Stations used from the CISN network consisted of 5 different high gain broad-band seismometers including 5 STS-1 (0.0027-10 Hz) seismometers, 3 STS-2.5 (0.0083-50 Hz) seismometers, 55 STS-2 (0.0083-50 Hz) seismometers, 7 CMG-3ESP (0.0083-50 Hz) seismometers and 12 CMG-3T (0.0083-50 Hz) seismometers. Station spacing for the selected land stations is approximately 35 km. However near the coast it reduces to 20 km because I used all operating stations along the coast.

2.3 Data Corrections

In this study an important element for the Rayleigh wave inversion procedure is the correction for instrument responses. This is especially important because we are combining OBS and land stations with many different sensor types. Rayleigh wave analysis incorporate amplitudes in the solution for velocity, thus amplitudes must be comparable between stations. After applying each instrument response correction, I found that all short period OBS (SP) were significantly larger (200%) than the long period OBS (LP). I then applied a second constant amplitude correction to rectify this by determining an empirical fit by comparing a group of SP data to a group of LP data.

I then corrected all seismograms with respect to the response of a common reliable

instrument type (STS-2) from the California Integrated Seismic Network (CISN). After this step, I found that all OBS amplitudes were smaller by two orders of magnitude in amplitude compared to all land stations. We thus added a final constant amplitude correction to the OBS data by following the procedure mentioned above. A second correction of 0.00063 was made to the short period OBSs since the amplitudes were still off compared with the amplitudes obtained after the first correction.

After windowing and filtering for periods between 16 s and 78 s an initial data set, I performed a preliminary inversion to solve for any additional amplitude corrections which takes into account the excellent azimuthal distribution of earthquakes as well as the large number of events we use in this study. Figures 2.2 and A1 show that the long period OBS's, located on deep seafloor, demonstrate a frequency-dependent amplitude problem for periods below 40 s. Since this does not occur for stations located in shallow water in the Borderland, I suggest that is not due to problems with the station or the station response file, but rather to significant structural changes across the study including increasing water depth, crustal thickness and lithospheric thickness and velocities. Since this same pattern is observed for 12 LP OBS's only located in deep seafloor, all of which have the same instrument response, this may be due to structural changes in the study area such as varying water depth with age or variations in the physical elastic properties of the crust and lithospheric with age.

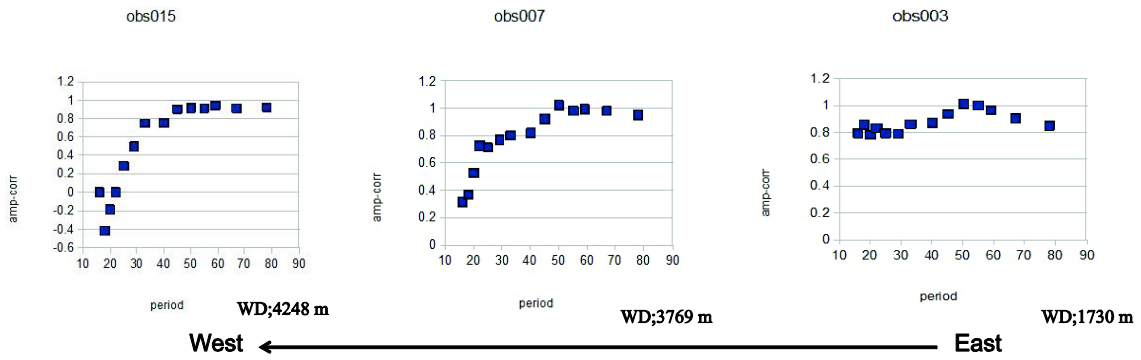

Figure 2.2: Behavior of the amplitudes with increasing depth. A correction of 1.0 indicates no correction is needed. This graph shows how the OBS amplitudes decrease dramatically at short periods for stations that are located in the west or in deep ocean water.

In this study, I temporarily omit the OBS data that demonstrates frequency-dependent amplitudes which is most evident in stations located on deep seafloor west of the Patton Escarpment. Land stations such as GRA, IDO, SRI, SCZ2, MOP, TA2 and STG and OBS stations such as 2, 6 and 17 were completely omitted in this study since they exhibited frequency-dependent amplitudes, except for OBS 6, which was omitted due to a mistake of location during the processing of the data . For LP stations 7, 8, 10, 11, 13, 15, 18, 19, 20, 21, 22, we only use data above 40s. For SP stations 5, 29, 30, 31, 34, we only use data at periods below 30s. This inversion also revealed that SP OBS's such as 05, 26, 27, 29, 30, 31, 33, and 34 had reverse amplitude polarity and were corrected.

The SNCC land station required large constant correction of 6.0 to match on land data. Land stations such as JEM, DGR, PLM, DNR required constant corrections of 1.1 and stations SDD, GOR and MUR had constant corrections of 1.15, 1.08 and 1.2 respectively. I applied additional constant amplitude corrections of 0.6 -1.0 to these stations: CIA, CLC, CWC, DPP, DGR, DNR, FMP, GATR, GOR, GSC, ISA, JEM, LCP, LGB, MPM, MUR, OLP, OSI, PHL, PLM, RPV, SCI2, SDD, SDG, SDR, SMI, SMW, SNCC,VES, as well as OBS03, OBS07, OBS08, OBS010, OBS011, OBS013, OBS015,

OBS017, OBS018, OBS019, OBS020, OBS021, OBS022, OBS023, OBS028, OBS029, OBS030 and OBS032

2.4 Earthquakes

I use vertical-component Rayleigh wave data since they are ideal in marine studies where the horizontal components are often noisier than the verticals due to seafloor currents and wave action. A total of 48 teleseismic events at distances ranging from 30° to 120° with magnitude (M_w) greater than 5.8 were selected, with a good azimuthal distribution (Figure 2.3), however, few events occur at NW and SW azimuths. The signal-to-noise ratio of the data set is high; above 3, and the raypath coverage is very good (Figure 2.4) which allowed me to obtain phase velocities at 14 different periods ranging between 16-78 s.

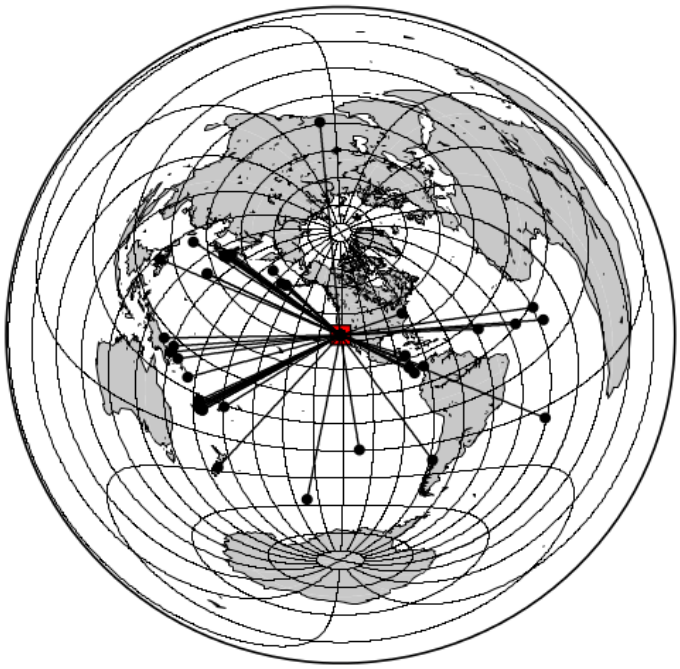

Figure 2.3: Azimuthal distribution of 48 earthquakes that I use in this study projected in an equidistant plot with our study area (red square) plotted at the center. The straight lines represent the great circle ray paths (black lines) followed by each earthquake (black filled circle) from the source to the center of the seismic array.

The ray path coverage for the study area when an optimal set of 100 events is considered is shown in the Figure 2.4. In this case raypaths cover a large extension of the NW quadrant of the area, as well as the SW and SE quadrants of it. Lack of raypath coverage can be detected north of the area due to a poor seismicity on the continental side.

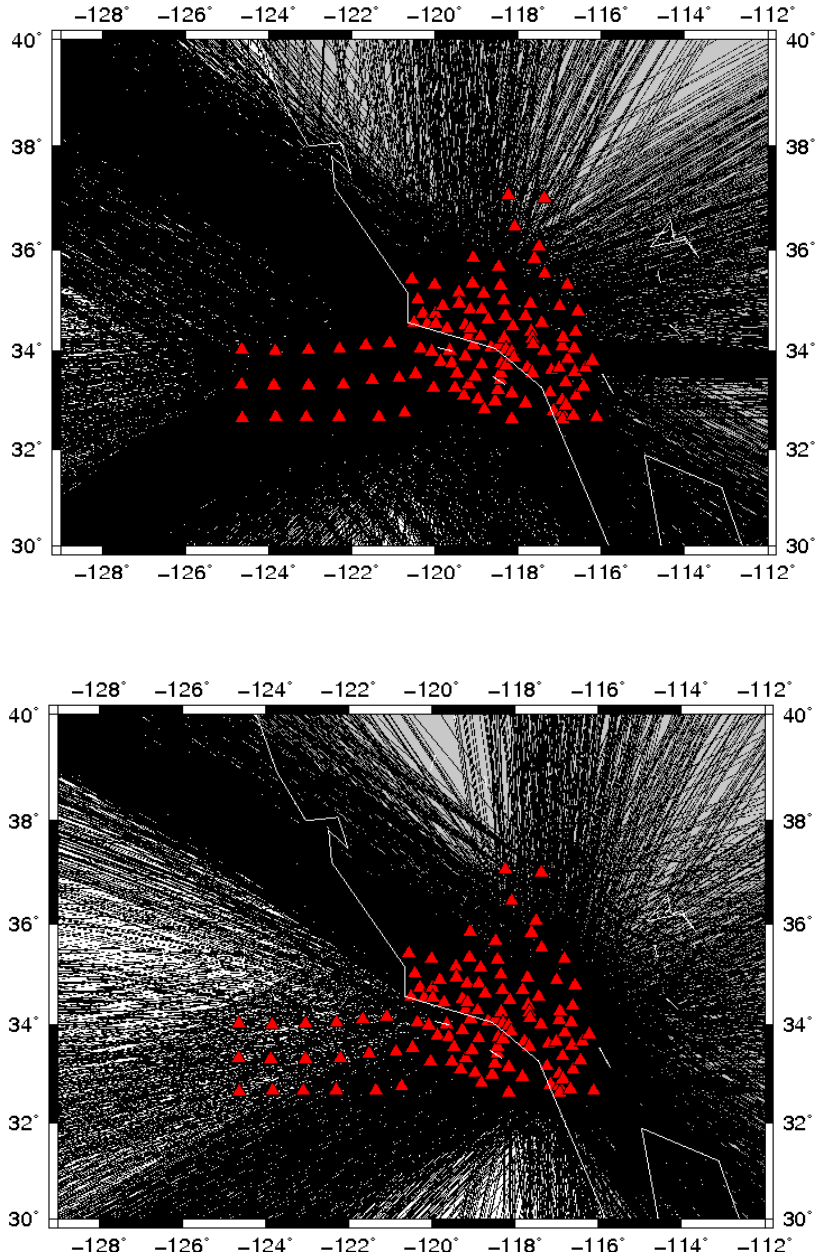

Figure 2.4: Raypaths coverage for the study area considering an optimal 100 events. Only 48 events are used in the data set presented here but have an even azimuthal distribution so the pattern of coverage is the same with slightly lower density. The black lines are raypaths from the source to the station. Red triangles mark the location of the seismic stations which include OBS's and land stations. The coastline is shown in white lines. (Two plots were required to plot the full 20,000 raypaths.)

Chapter 3 Surface Wave Method

The measurement of phase velocities from Rayleigh wave data crossing a seismic array is a powerful approach to detect variations in lithospheric and asthenospheric structure. In this tomographic inversion for phase velocity, I take into account perturbations in the wave field due to non-great circle path propagation with a two-plane wave approximation (Forsyth and Li., 2005). This approximation allows for complexity in the incoming wave field not considered in traditional tomographic techniques. Finite- frequency effects are also considered when we solve for phase velocities (Yang and Forsyth, 2006b)

The incoming wave field is represented by the interference of two plane waves of the form

$$U_z = A_1(\omega)e^{-i(k_1x-\omega t)} + A_2(\omega)e^{-i(k_2x-\omega t)} \qquad (1)$$

where A is the amplitude, k is the wavenumber, t the time and x is the position vector for each wave. Thus the incoming wave field at frequency ω is described by six parameters including the amplitude, phase and direction of each of the two waves. The inversion solves for the phase, amplitude, and propagation direction for both of the two plane waves that represent each event, as well as the averaged phase velocity (1-D), regional phase velocity (2-D), and parameters for azimuthal anisotropy.

This approach considers constructive and deconstructive interference of two plane waves across the seismic array which means that at any instant if the waves interfere constructively they are in phase, and when they interfere destructively they are out of phase.

The surface wave phase velocity is given by,

$$c(\omega,\theta) = A_0(\omega) + A_1(\omega)cos(2\theta) + A_2 sin(2\theta) \qquad (2)$$

where ω is the angular frequency, θ is the azimuth, A_o is the azimuthally averaged phase velocity and A_1, A_2, are azimuthal anisotropic coefficients in which we have neglected terms of higher order (Smith and Dahlen, 1973; Weeraratne et al., 2007)

In the data analysis, each seismogram is decimated to a sample rate of 5 sps. I filter the Rayleigh wave with a 10-mHz-wide, zero-phase-shift band pass filter centered at the frequency chosen. Second, we window each seismogram around the Rayleigh wave to avoid noise and other body waves phases. Then, I determine the phase and amplitude using Fourier analysis. I solved for the parameters of each incoming wave including phase, amplitude and direction, using a non-linear inversion (1). And finally, I obtained phase velocity coefficients at grid nodes spaced 1° apart throughout the study area (Figure 3.1) in a linear inversion (2) that compares predicted and observed phases in a least squares sense. An outer region of more sparsely spaced grid nodes is used in a subset of inversions that absorb outliers and deviations from the 2-plane wave approximation.

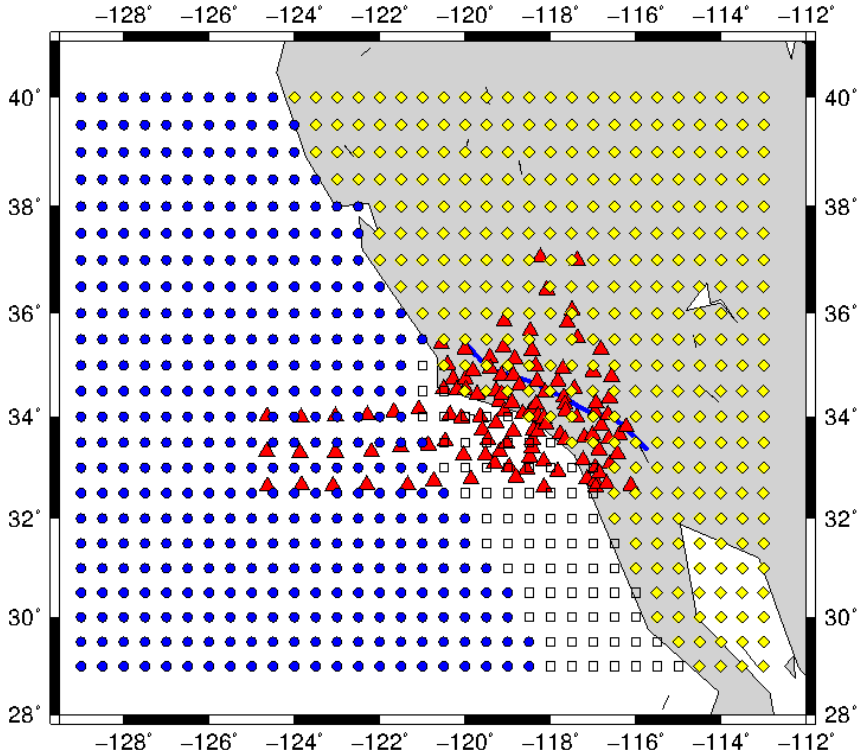

Figure 3.1: Grid node configuration used to solve for phase velocities within the study area. Red triangles mark locations of the OBS's and land stations used in this study. A dense spacing of nodes in the center marks region where we have our best coverage. The less dense outer nodes absorb deviations from the 2 plane wave approximation. Seafloor is designated by blue circles, Borderland is designated by white squares and land is designated by yellow diamonds. Blue line is the location of the San Andreas Fault.

Chapter 4 Results

4.1 Phase velocity results

4.1.1 1-D uniform phase velocity results

I present inversion results for Rayleigh wave phase velocities and anisotropy for both onshore and offshore southern California. The inversion procedure involves a multi-step procedure in which all inversions are based on least squares minimization which implicitly assumes a Gaussian distribution of errors (Forsyth and Li., 2005). In the first step we perform an inversion for isotropic phase velocity averaged across the entire study area and station amplitude corrections using a given starting model. Here I use an *a priori* velocity model based on previous studies (Nishimura and Forsyth, 1989) in 20-52 Ma seafloor (dashed line, Figure 4.1). I checked all station amplitudes for corrections (see section 2.3) before proceeding. In the second step I invert for phase velocity and anisotropy simultaneously using the results from step 1 as a starting model. Here velocity and anisotropy are averaged over the entire study area. This starting model takes advantage of *a priori* information and reduces our need for excess damping. In the third step, I invert for phase velocities averaged within 3 regions (based on geological observations) and use the velocity result from step 2 as a starting model. In step 4, I perform a final set of inversions for lateral variations in velocity which produces 2-D maps. Here, I explore several starting models including a uniform velocity from step 2 as well as the velocity in 3 regions from step 4. Doing a multi-step process where each result builds on the previous step improves the stability of the inversion.

I begin with the first inversion that solves for the average Rayleigh wave phase velocity dispersion curve for the entire region. As a starting model for the inversion, I use velocity data based on previous results of Rayleigh wave phase velocities (Nishimura and

Forsyth, 1989) for an area of 20-52 Ma (dashed line in Figure 4.1). The starting model uses velocities of 3.94 km/s for 16 s, 3.95 km/s for 18 s, 3.96 km/s for 20 s, 3.97 km/s for periods of 22-59 s, and 3.98 km/s for periods of 67 and 78 s. The resulting velocity dispersion curve after running the first inversion is shown in Figure 4.1. When considering velocities without anisotropy (red circles), phase velocities increase sharply from 16 s to 30 s with phase velocities from 3.42 to 3.81 km/s. (It is important to note here that the OBS data for these periods on deep seafloor west of the Patton escarpment is temporarily removed from this data set.) Thus these velocities are controlled by the stations on land and the Borderland and dominantly represent crustal structure in these areas. For periods above 40 s the slope of the dispersion curves changes and velocities increase slowly to a constant of approximately 3.89 km/s. This change in slope is due to change in sensitivity of Rayleigh waves from the crust at short periods below 40 s to the mantle lithosphere at long periods above 40 s. This change in slope which occurs at ~33 s (corresponding to a peak depth of sensitivity of 30-40 km) indicates that the data at short periods dominantly samples continental crustal structure.

I performed a second inversion which solves for phase velocity and anisotropy simultaneously averaged across the study area. Here I use the starting model from the previous result (red circles, Figure 4.1). The phase velocity results are shown by the blue squares in Figure 4.1 they indicate that when anisotropy is considered, phase velocity is slightly reduced. This is due to tradeoffs between velocity and anisotropy in our inversion (see equation 2). For example, for periods between 25 s and 40 s, the anisotropic phase velocity is reduced by 0.8 %, and for periods between 40 and 59 s the phase velocity is reduced by 0.4 %.

Phase velocities for our study area are slower than velocities observed in previous studies (Nishimura and Forsyth, 1988) for all periods. For long periods above 40 s, our velocities are 2% lower than previous studies. Below 40 s, our data mostly sample crustal structure in the Borderland and on land and don't give a useful comparison to Pacific seafloor data.

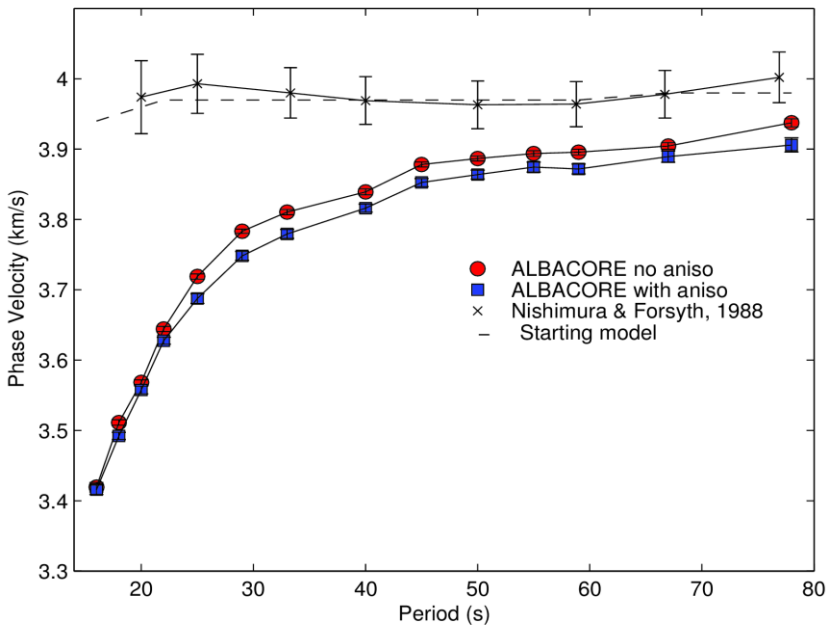

Figure 4.1: Average phase velocity as a function of period. Vertical bars on the data points indicate two standard deviations; note that some of them are smaller than the symbols. The dispersion curves represented by red circles and blue squares refer to isotropic and anisotropic phase velocities respectively. The red circles shows the dispersion curve from a first inversion that solves for isotropic phase velocity and the blue squares shows the results from a second inversion that solves for anisotropic phase velocity and anisotropy simultaneously for an area with a seafloor age of 18-32 Ma. The cross data points show results from previous studies (Nishimura and Forsyth, 1989) for and area with a seafloor age of 20-52 Ma., and the dashed line represents the starting model used for the first inversion based on these results.

4.1.2 Phase velocity in 3 regions

A third inversion allows me to solve for the average isotropic phase velocity in 3 regions (Figure 4.2). I chose the 3 regions based on geological and structural data where the boundaries of the deep seafloor, Borderland, and continental coastline are observed (Figure 3.1). I selected respective grid nodes which lie in each region. The inversion obtains an average phase velocity for all the nodes in that group.

Phase velocities at short periods below 30 s are highest for the Borderland region (open squares) compared to all other regions by 2.9 %. Most of the short-period data for the deep seafloor and land do not differ because very little OBS data contributes to the blue points in this data set. Above 40 s, the highest phase velocities are in the deep seafloor (blue circles) compared to other regions. Phase velocities for the Borderland and land regions; white squares and yellow diamonds respectively, increase very gradually for periods above 55 s with velocities of 3.88 to 3.92 km/s. The phase velocities are 2 % higher compared to studies from Yang and Forsyth (2006), and 2.3 % lower compared to Nishimura and Forsyth (1988) results. The difference between our results and the former, may be that they cover a larger area including eastern California, Nevada, and Arizona east of our study area which may have thicker crust and also contains the Basin-Range province.

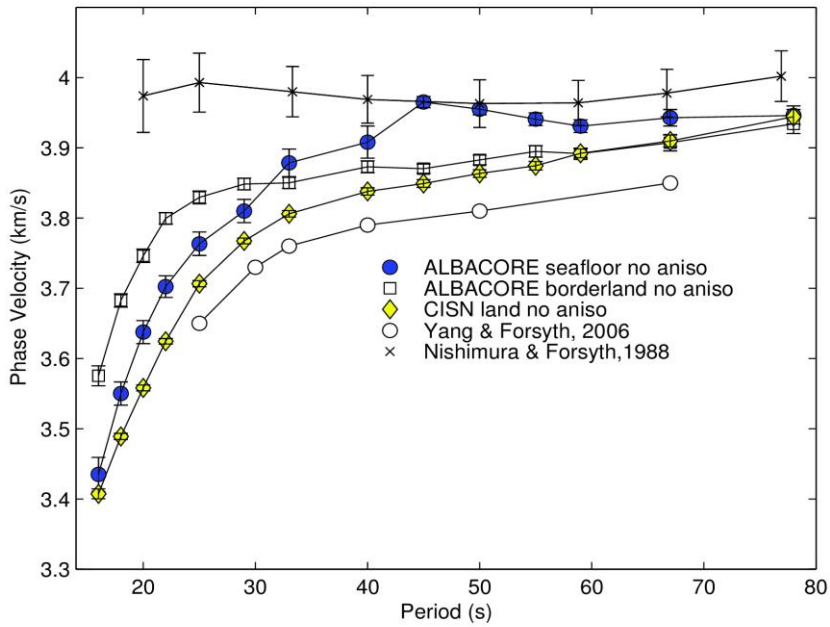

Figure 4.2: Average phase velocity as a function of period in three regions. Deep seafloor is designated by blue circles, borderland is designated by white squares, and land is designated by yellow diamonds. Vertical error bars on the data points indicate two standard deviations and some of them are smaller than the symbols. The dispersion curves represent the average phase velocity for three regions of the study area. The cross data points show results from previous studies (Nishimura and Forsyth, 1989). Previous studies from Yang and Forsyth, (2006); white circles, confirm the behavior of the dispersion curves found on the study area.

4.2 2-D maps

I performed a fourth inversion which allows velocity to vary at each grid node in our study area. This increases our data parameters significantly to 500-700 unknowns, not including anisotropic terms; however this project has sufficient number of stations and earthquake records to resolve these parameters. The velocities obtained for the 3 regions; deep seafloor, Borderland and land, are used as starting velocities for their respective nodes in this inversion. Here I incorporate finite-frequency sensitivity kernels that use an 80 km smoothing length and uniform grid of nodes to solve for lateral variations in phase velocity and anisotropy simultaneously. In my two dimensional inversion, I account for

frequency-dependent scattering in the wave field (Gudmundsson, 1996), using a characteristic smoothing length (Lw) for each period which is calculated using the equation

$$L_w = x_f / 2\sqrt{2} \tag{3}$$

where x_f is the width of the Fresnel zone.

The data are masked to show only information in the areas that are considered reliable within two standard deviations based on the distribution of the standard errors in error maps shown in Figure 4.3. The results show the behavior of the velocity structure for the entire study area at different periods.

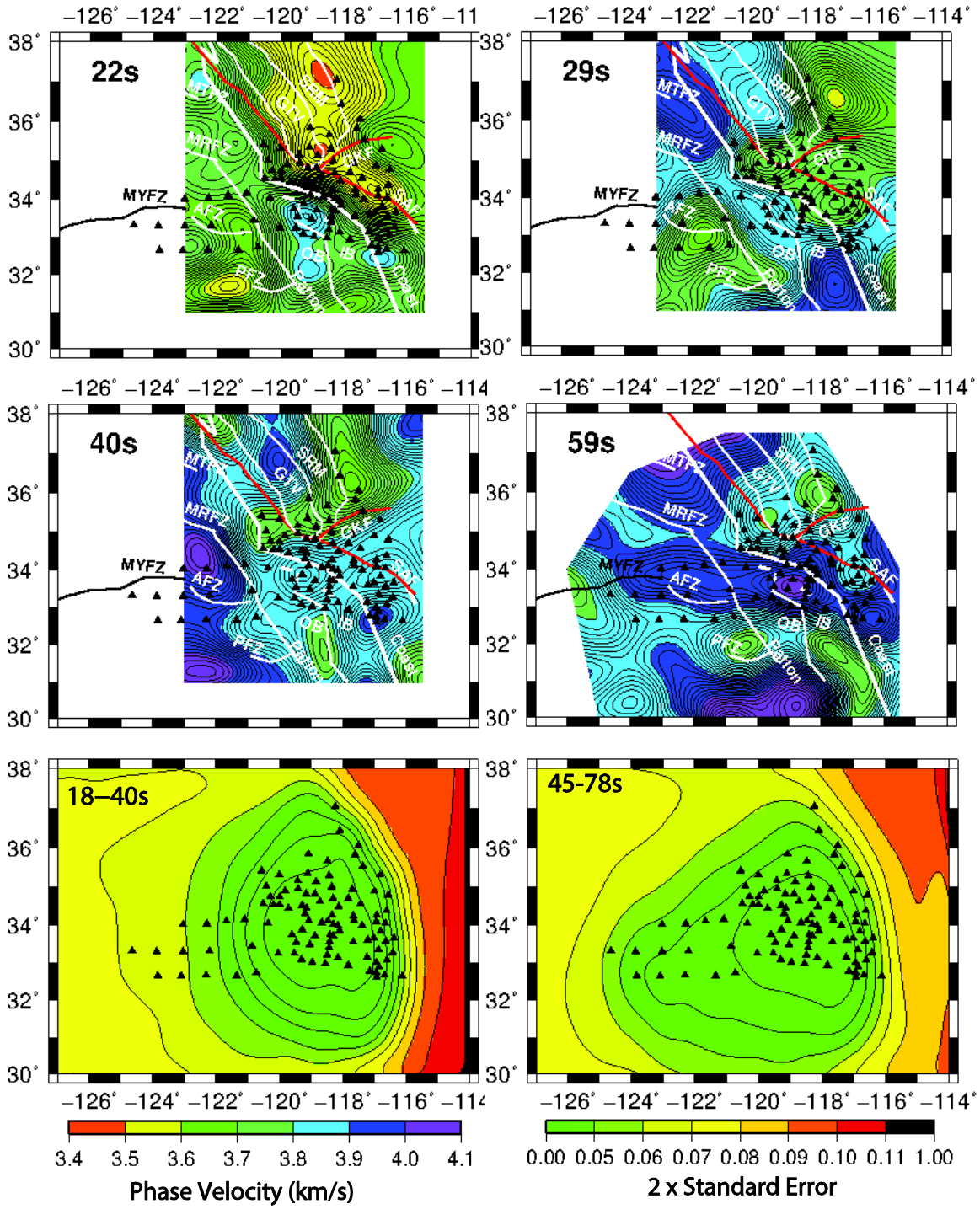

Figure 4.3: Phase velocity maps for periods of 22 s, 29 s, 40 s, 59 s. The data are masked to show only reliable information based on the distribution of the standard errors. The first row, from left to right, shows 2D-maps for periods of 22 s and 29 s. The second row shows 2D-maps for the period of 40 s and 59 s. The third row shows the distribution of the errors for the respective periods. All velocity maps above 40 s have an expanded area of resolution as indicated for errors at 59 s due to inclusion of all Broadband OBS data for the long period data. Contour intervals are 0.1 km/s. The geologic structures shown here are: the Monterrey Fracture Zone (MTFZ), Morro

Fracture Zone (MRFZ), Murray Fracture Zone (MYFZ), Arguello Fracture Zone (AFZ), Patton Fracture Zone (PFZ), Patton Escarpment (Patton), Coast line (Coast), Inner Borderland (IB), Outer Borderland (OB), Sierra Nevada Mountains (SRM), Great Valley (GTV), Garlock Fault (GKF), and San Andreas Fault (SAF).

4.2.1 Lateral velocity variations in continental California

The strongest and most persistent feature in our study areas is a low-velocity anomaly in the NE corner of our study area that is 6 -9 % lower than the surrounding regions observed between 16 s to 78 s periods. This anomaly is located beneath the southern tip of the Sierra Nevada Mountains. Phase velocities beneath the Great Valley region are higher than velocities beneath the Sierra Nevada for all periods.

A low- velocity anomaly is also present under the San Andreas fault (SAF) where the bend is located near the intersection with the Garlock fault near 35o latitude with a 9 % difference with to the surrounding regions . The anomaly is observed at periods from 16 s to 67 s. The anomaly shifts from its location slightly east of the SAF at 22s moving to the west with increasing period and as is slightly west of the SAF at 40 s. For periods above 55s, this anomaly appears to extend offshore west of Point Conception.

A low-velocity anomaly is observed on the north side of the SAF SE of the bend near 34° latitude located beneath the San Bernardino Mountains at periods from 16 s – 33 s. At a period of 25 s, a high velocity anomaly appears between these two low velocity anomalies as a thin feature that trends in NE-SW direction perpendicular to the SAF. This linear high velocity anomaly gets longer and wider with period up to 78 s, extending offshore. This observation is consistent with previous studies (Yang and Forsyth, 2006). This may be the extension of the Transverse Ranges feature offshore (Kohler et al. 2003).

4.2.2 Lateral velocity variations in the Borderland

A small high-velocity anomaly is observed in the northern region of the Inner Borderland that is 3% higher than the surrounding regions. It is centered beneath the region that includes the Santa Cruz Basin and Santa Rosa and Santa Cruz Channel Islands. The anomaly is present at all periods. (This anomaly changes at periods of 22 s - 25 s and becomes more diffuse extending NW-SE through Borderland.). At the longest periods above 55 s, this high velocity anomaly shifts to the east beneath the coastline.

I observe a high-velocity anomaly that lies at the southern end of the Outer Borderland (on the east side of the Patton escarpment) that is 6 % higher than surrounding regions. The anomaly is observed for periods between 16 s and 45 s. This anomaly extends west of the Borderlands and follows along the northern side of the Patton Fracture zone at periods for 33 s- 45 s,

4.2.3 Lateral velocity variations in the deep seafloor

A high-velocity anomaly is observed along or west of the coastline north of Point Conception beneath the Monterey fracture zone. The anomaly is 3 % higher than the surrounding regions. The anomaly is present at periods up to 33 s and gets wider and extends further offshore with increasing periods.

Significantly higher velocity anomalies are located north of the Murray fracture zone, compared to the region south of this boundary for periods from 22 s to 55 s. This may be due to the offset of seafloor age across this fracture zone which is older on the north side predicting high density, colder, and thicker lithosphere producing higher seismic velocities. This velocity difference is not present above 45 s indicating that the lithospheric thickness does not extend beyond these periods corresponding to about 60

km (±25 km) depth.

I observe a low-velocity anomaly located on the western side of the Patton escarpment beneath OBS stations 20, 21, and 22 for short periods from 16 s to 20 s.. The anomaly is 6 % lower than the surrounding regions. This may be due to a layer of sediments deposited as a submarine alluvial fan from the continental shelf fed by submarine channels identified by new bathymetry from our marine survey. This anomaly changes to a high velocity anomaly at 20 - 22 s but is on the edge of our resolution limits for the short period maps.

For periods above 29 s - 45 s, isolated velocity anomalies in the deep seafloor change to a systematic pattern where velocities form parallel lines aligned with magnetic anomaly orientation (see Figure 1.2) trending in a NS direction. These linear velocity bands increase in velocity towards the west corresponding to increasing seafloor age. In the deep seafloor, the increasing pattern of velocities which are approximately parallel to the magnetic lineations (oriented NS) for periods up to 45 s, change to a NW-SE trend for all periods above 50 s. This may indicate alignment with Pacific plate motion in the lower lithosphere or asthenosphere and also mark the base of the LAB (lithosphere-asthenosphere boundary.

While velocities increase on average from east to west in the deep seafloor, they do so in a slightly sinusoidal pattern (e.g. 3.9 km/s contour line at 40 s). The sinusoidal pattern coincides with the spacing between the surface location of offshore fractures zones offshore (Monterey, Morro, Murray, Arguello, and Patton fractures zones) as shown in the velocity map at 40 s in Figure 4.3. This pattern produces lower phase velocities on the north side of the fracture zone compared to the south side in every case

except the Murray fracture zone where this relationship is reversed (higher velocities are observed on the north side).

I observe a high velocity anomaly at periods between 40 s - 59 s located at the southern edge of our study area. The location of this anomaly is not well resolved due to lack of stations here.

4.3 Anisotropy results

4.3.1 Average anisotropy

Average anisotropy is also obtained with the inversion for phase velocity (blue squares in Figure 4.1).The inversion solves simultaneously for azimuthal anisotropy averaged over the entire study area. Azimuthal anisotropy (Figure 4.4) is well resolved from zero for all periods. The results show that the strength of anisotropy is consistent at 1.5 % ± 0.09 % for nearly all periods within error with the exception of the data point at 16s, which may have some sampling of the water layer. The average azimuth of the anisotropy for all periods is approximately N 73° W ± 2°. Note that the short period data below 40 s do not include the deep seafloor region in this data set and dominantly indicate sampling of Borderland and continental structure.

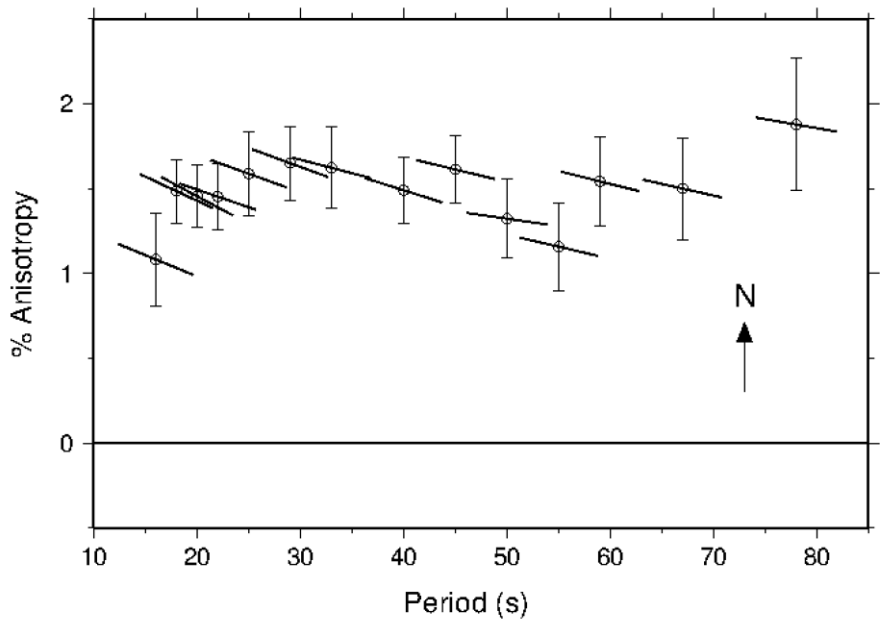

Figure 4.4: Average anisotropy within the area of study as a function of period. The error bars indicate two standard deviations, 95 % confidence. Thick lines indicate the direction of the anisotropy in map view with reference to North.

4.3.2 Anisotropy in three regions

I solve for anisotropy in three regions in inversions which consider 2D variations in phase velocity. In the deep seafloor (Figure 4.5a) anisotropy is consistent in a NW-SE direction for nearly all periods except a few cases that are not resolvably different within error. The strength of anisotropy may increase with increasing period, however, the removal of data at short periods may influence this result.

For the case of the Borderlands (Figure 4.5b) we observe the direction of anisotropy trends in a NW-SE direction for all periods below 40 s. The fast direction of anisotropy rotates to a N-S azimuth for periods above 50 s. The mid-periods between 45 s - 50 s may represent a transition from these 2 dominant directions due to overlap in Rayleigh sampling at adjacent periods. The magnitude of anisotropy for the shortest

periods (16-20 s) on average is 1.3%. The magnitude decreases to 0.5% for periods from 22 s -33 s. The magnitude increases again up to 1.4% for the longest periods. The decrease in the strength of anisotropy from 20 s - 45 s may be due to Rayleigh wave sampling of two structures which have a boundary at approximately the peak sensitivity depth of 40 km depth (± 20 km).

Lastly, in the case of continental region (Figure 4.5c), the direction of anisotropy is trending EW for all periods below 30 s with the exception of 18 s which is close to zero and displays small magnitude. The magnitude of anisotropy below 30 s is 1.0 %. Above 30 s, the direction of anisotropy changes to NW-SE for all periods except 40 s and 67 s. For periods above 30 s, the magnitude of anisotropy fluctuates between 0.9 % and 1.4% within error.

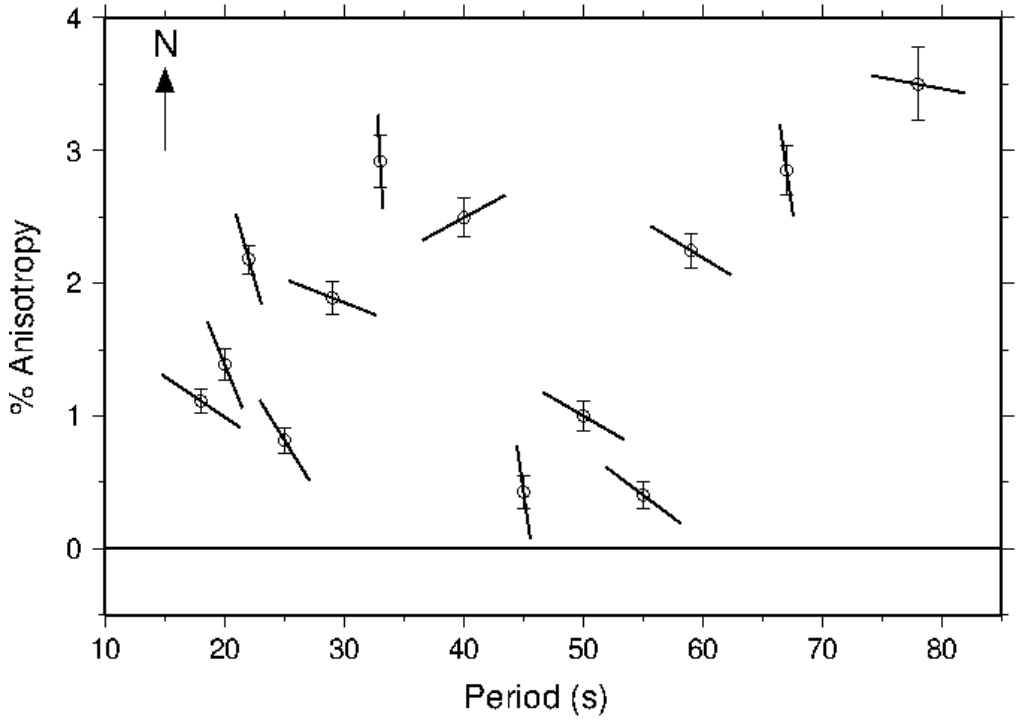

Figure 4.5a: Anisotropy in the deep seafloor area. The error bars indicate two standard deviations, 95 % confidence. Short lines indicate the direction of the strength of the anisotropy for fast directions.

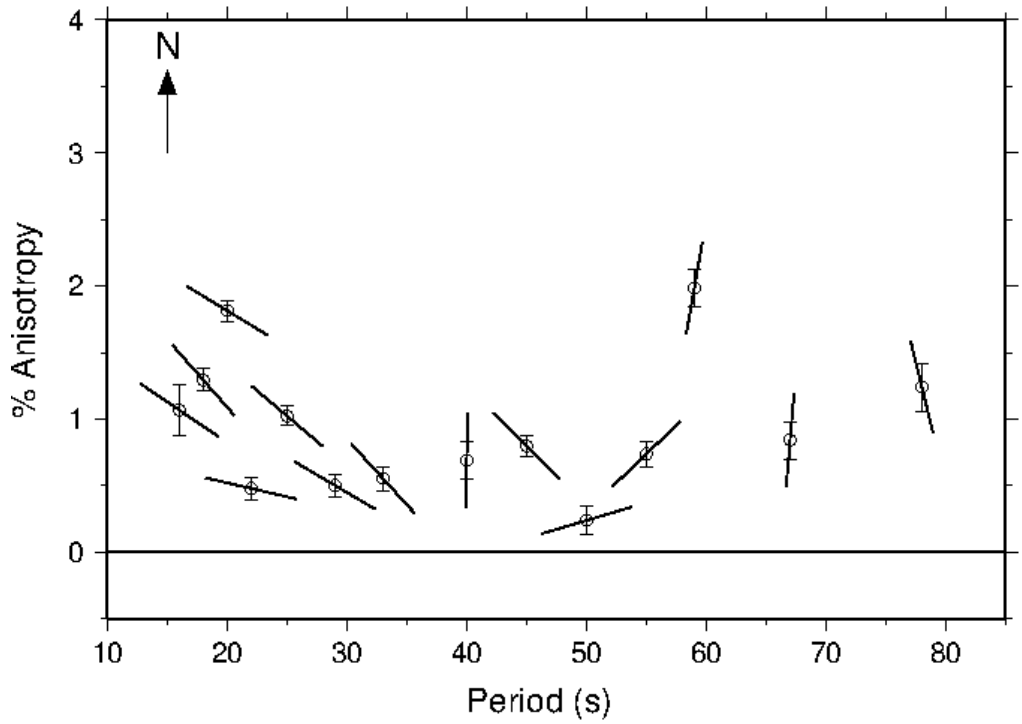

Figure 4.5b: Anisotropy in the borderland. The error bars indicate two standard deviations, 95 % confidence. Short lines indicate the direction of the strength of the anisotropy for fast directions.

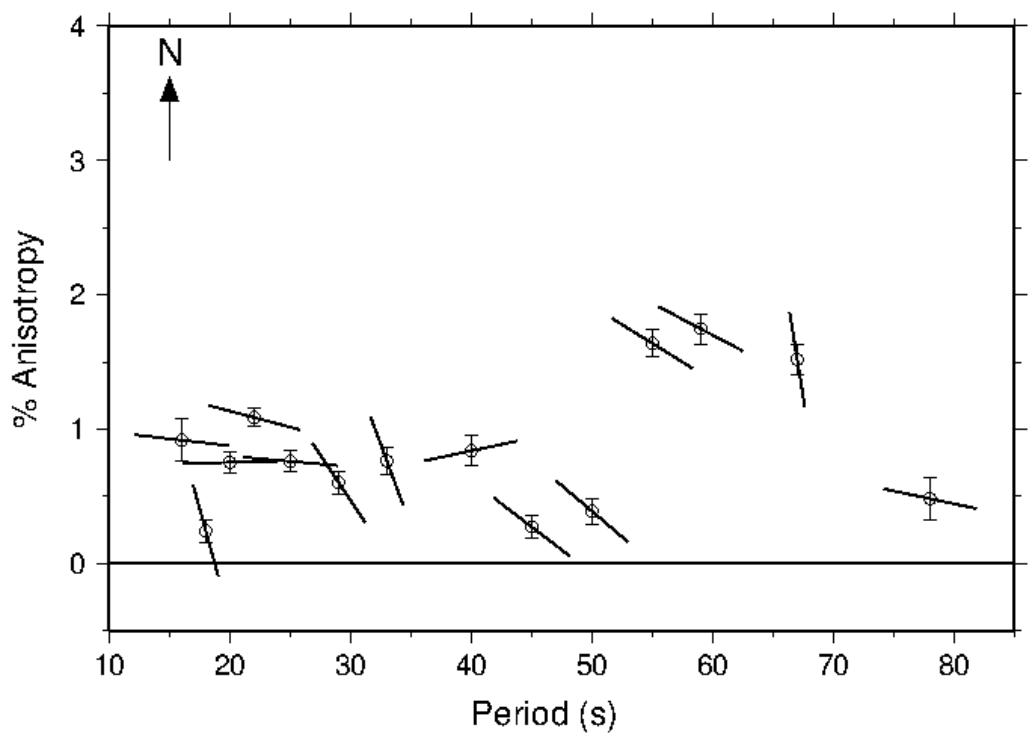

Figure 4.5c: Anisotropy in the land. The error bars indicate two standard deviations, 95 % confidence. Short lines indicate the direction of the strength of the anisotropy for fast directions

The multi-step inversion process I use helps stabilize our final results for 2-D velocities and anisotropy overall taking advantage of *a priori* information from each successive inversion. The residuals from each inversion are shown in Figure 4.6. Notice that this multi-step process shows that although I increase the number of data parameters (unknowns) significantly from ~ 10 in the inversion for three regions (white circles) to 759 in the inversion for 2-D velocity (yellow circles), that the RMS phase misfit goes down by 35 %. This also suggests that allowing for lateral velocity variations is important in this area where lateral structure has strong variations across this continental margin.

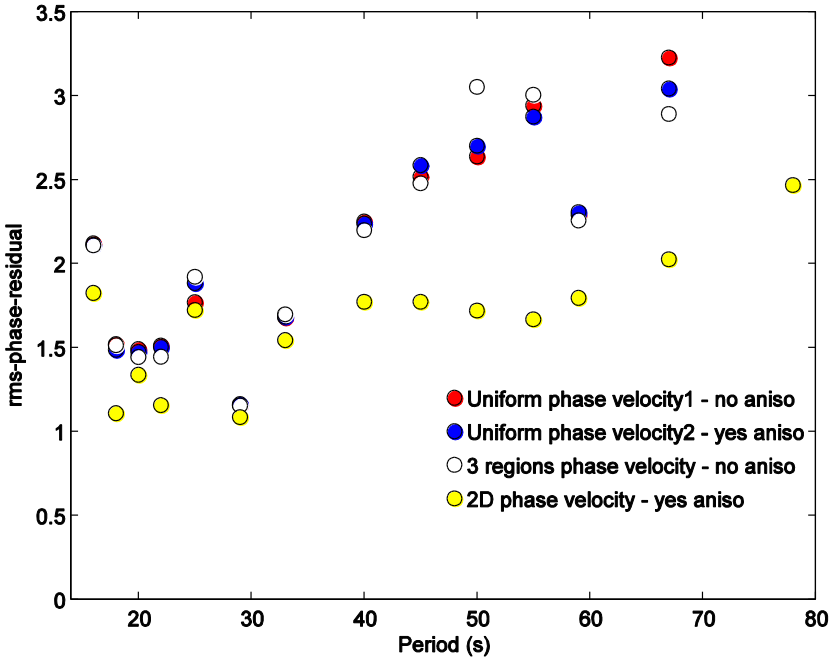

Figure 4.6: Phase residuals as a function of period. Inversion that solves for uniform phase velocities is designated by the red circles, inversion that solves for averaged phase velocity and anisotropy is designated by blue circles, inversion that solves for phase velocity in three regions is designated by the white circles, and inversion that solves for 2-D maps with anisotropy is designated by yellow circles.

Chapter 5 Discussion

5.1 Velocity structure in the deep seafloor

I observe phase velocities which are 1.3% lower than the velocities found by Nishimura and Forsyth, (1988) on seafloor with age of 20 - 52 Ma (Figure 4.1). This is likely due to the younger age seafloor in our study area of 18 – 32 Ma. However, the fact that they use land stations with paths that cross through the ocean compared with my study that uses OBS's, a very focused high resolution study, may also influence in this result. On the other hand, according to studies of Rayleigh phase waves on the seafloor (Forsyth et al., 1998), phase velocities increase systematically with increasing age of the seafloor which is consistent with what I found after solving for phase velocities in my study area.

This N-S alignment of velocity structure observed at periods from 29 s - 45 schanges to a NW-SE alignment at longer periods to become parallel to Pacific plate motion. This indicates lithospheric growth by cooling processes at depths associated with periods below 45s. Fabric alignment or flow of lower lithosphere or asthenospheric material at periods below 45 s may be caused by mantle drag from plate motion in the NW direction (Liu and Bird, 2002) This change in velocity structure at 40-45 s may correspond to the base of the lithosphere which will be confirmed in future work where phase velocity data isinverted for shear wave structure.

While velocities increase on average from east to west in the deep seafloor, they do so in a slightly sinusoidal pattern (e.g. 3.9 km/s contour line at 40 s). The sinusoidal pattern coincides with the spacing between the surface location of offshore fractures zones offshore (Monterey, Morro, Murray, Arguello, and Patton fractures zones) as shown in the velocity map at 40 s in Figure 4.3. This pattern produces lower phase

velocities on the north side of the fracture zone compared to the south side in every case except the Murray fracture zone where this relationship is reversed (higher velocities are observed on the north side). This is consistent with the age offset across fracture zone indicated by magnetic anomalies (see Figure 1.2). The Murray fracture zone is a large major fracture zone that extends a great distance west of our study into the central Pacific and exhibits older seafloor north of this boundary everywhere along its axis. However, the smaller fracture zones near the California coast (Monterey, Morro, Arguello, and Patton fracture zones) have all experienced rotation in a clockwise direction compared to the undisturbed Pacific seafloor immediately to the west of these features. This rotation places slightly younger seafloor north of every fracture zone that has experienced rotation. This is consistent with our observation of lower velocities on the north side of the small fractures zone associated with younger lithosphere. These features are only observed to 45 s period. This suggests there is deformation or rotation of at lithospheric depths associated with the rotation of these fracture zones. Previous studies indicate forces from plate capture may have produced these non-uniform fracture zone shapes (Atwater, 1989).

5.2 Oceanic versus continental lithosphere

Phase velocities are higher in deep seafloor lithosphere at periods above 40 s compared to the Borderland and land regions (Figure 4.2). This may be due to the different formation processes of oceanic and continental lithosphere. On one hand, oceanic lithosphere is formed by cooling with time and age. At the spreading center lithosphere forms from melting of magmas derived from the depleted mantle asthenosphere (Workman and Hart, 2004). The continental lithosphere in California

(western U.S.), by comparison, is formed by melting processes that are generated at the subduction zone. Continental lithospheric growth at a convergent margin is accomplished by tectonic accretion of intra-oceanic island arcs or magmatic additions at continental arcs (Rudnick, 1995). These formation processes, therefore, may create continental lithosphere that is more hydrated and rich in hydrous phases where phase velocities will travel slower compared to a region with a more depleted dry oceanic lithosphere (e.g. Evans et al., 2005) where phase velocities can travel faster.

5.3 Velocity structure in the Borderlands

There is a consistent observation of a high velocity anomaly in the northern region of the inner Borderland at all periods. This is distinct from a high velocity anomaly in the southern region of the outer Borderland indicating a division or tectonic boundary between these two regions. Phase velocities for the Borderland are higher than land, which may be due to crustal accretion or underplating of sequences like the Catalina Schist (Bohannon and Geist, 1998) during rifting and extension. On the other hand, differences between our results and Yang and Forsyth (2006a), where the phase velocities are higher by 2%, may be due to the coverage of a larger area including eastern California, Nevada, and Arizona east of our study area which may have thicker crust and also contains the Basin and Range province.

5.4 San Andreas, Garlock, and Murray transform faults

Another feature is observed at periods between 16 s- 67 s located on the bend of the San Andreas fault. This feature is reported by other surface wave studies on the continental side (Yang and Forsyth, 2006a) and this may be related to the Garlock fault intersection with the San Andreas at this location. However sensitivity to 67 s is at least

70 km depth below the expected depth for fault structures. Other possibilities are hydrothermal infiltration through pore spaces at the fault surfaces, however, this would also be a fairly shallow feature. It may be a significant structure at mantle depths perhaps associated with subduction of the Murray fracture zone or seafloor topography at this location.

5.5 The Western Transverse Ranges

The high velocity anomaly located beneath the coastline at 67 s may indicate the existence of a remnant section of slab broken off during the previous convergent margin event (Atwater, 1989). The fracturing of remnant slabs is also reported by studies using surface wave tomography beneath the North American plate along the California, Mexico coastline (Wang et al., 2013). In this study, inversions for shear wave velocity indicate this structure extends to a depth of 70 km beneath the Transverse range as well as a similar structure in the Baja region (Wang et al., 2013). The structure located near the Transverse ranges coincides with the high velocity linear anomaly than extends offshore which I observe in the 2D map for a respective depth of 80 km. Body wave tomography studies indicate this may extend even deeper to 150 km depth (Kohler et al., 2003).

Anisotropy for continental southern California (Figure 4.5c) is approximately N 33° W and is consistent with previous studies which used land instruments only (Yang and Forsyth, 2006a) for periods below 60 s. Our results differ above 60 s, however, where I show a rotation to the NNW direction. Again, note that for the deep seafloor area (Figure 4.5a) all data is controlled by the Borderland and land data since no OBS data is used here.

Anisotropy is consistent with Pacific plate motion, N 78.5˚ W, (Gripp and Gordon,

2002) in a NW-SE direction for all regions in our study area, except for the periods above 40 s in the Borderlands. At sub-Moho depths in the Borderland, the NS azimuth that is observed may be parallel to the ancient direction of the subduction zone between the Pacific and the North American plate over 30 Ma.

For periods below 30 s in the continental region, the fast directions are consistent with previous shear waves splitting results (Polet and Kanamori, 2002) which indicates that the anisotropy pattern observed in southern California is a direct result from the alignment of the a-axis of olivine crystals (E-W fast directions), nearly perpendicular to the World Stress Map vectors (N-S direction) of lithospheric shortening.

5.6 The Sierra Nevada Mountains

Maps of Rayleigh wave phase velocities for periods between 16 s and 78 s show a low-velocity anomaly located on the NE corner of my study area. The feature extends down to a depth of approximately 100 km which I associate with a high heat flow due to the removal of mantle lithosphere from beneath the southern Sierra Nevada region (Saleeby et al., 2012; Gilbert et al., 2012). More specifically, the results from thermomechanical modeling and observational data (Saleeby et al., 2012) suggest that a complex array of positive and negative epeirogenic transients migrated across the southern Sierra Nevada region in late Neogene-Quaternary time, in response to initial mantle lithosphere mobilization, and then a rapid delamination of the arclogite root that developed in the Cretaceous beneath the Sierra Nevada batholith (Saleeby et al., 2012).

Chapter 6 Conclusion

The results obtained for phase wave velocities are consistent with previous results from surface wave studies (Nishimura and Forsyth, 1998). Phase velocities are slower by 1.3 % for periods above 40 s, a result that confirms the fact that phase velocities systematically increase as they travel through older seafloor (Forsyth et al., 1998). On the other hand, phase velocities results for the three regions has the same behavior compared to previous results from Yang and Forsyth (2006a), however, my results are higher by 2 %.

Phase velocity maps show that The Sierra Nevada range has a high heat flow to approximately a depth of at least 100 km or greater (Saleeby et al., 2012; Gilbert et al., 2012). Phase velocities offshore southern California in the oceanic mantle align in the N-S direction and show increasing velocities with older seafloor ages to the west at periods of up to 45 s. At 55 s, velocity structure changes to an E-W alignment indicating a transition from oceanic lithospheric below 40 s to asthenospheric mantle flow aligned with Pacific plate motion above 55 s. Velocity anomalies also show that beneath the coastline, at a period of 67 s, the possible existence of a remnant section of slab broken off during the time when the area had an active subduction zone.

Most of our anisotropy results indicate fast directions that are consistent with Pacific plate motion. The only exception is at long periods in the Borderland region above 40s where a consistent NS azimuth is observed. This azimuth is parallel to the ancient subduction zone axis. On the continent, anisotropy for periods below 30 s indicates EW fast directions at crustal depths which shift to NW-SE at longer periods below the Moho.

References

Atwater, T., Implications of plate tectonics for the Cenozoic tectonic evolution of Western North America, *Geol. Soc. Am. Bull., 81*, 3513-3536, 1970.

Atwater, T., Plate tectonic history of the northeast Pacific and western North America, i*n The Eastern Pacific Ocean and Hawaii,* edited by E. L. Winterer, D. M. Hussong, and R. W. Decker, pp. 29 –72, *Geol. Soc. of Am*., Boulder, Colo., 1989.

Baher, S. A, P. M. Davis and G. Fuis, Separation of site effects and structural focusing in the damage zone from the Northridge earthquake, *Bull Soc. Seis. Am.*, *92*, 3134-3151, 2002.

Bohannon, R. G., and E. Geist, Upper crustal structure and Neogene tectonic development of the California Continental Borderland, *Geol. Soc. Am. Bull*., 110, 779 – 800, 1998.

Crouch, J. K., and J. Suppe, Late Cenozoic tectonic evolution of the Los Angeles Basin and inner California borderland: a model for core complex-like crustal extension, *Geol. Soc. Am. Bull., 105*, 1415-1434, 1993.

Engebretson, D. C., A. Cox, and R. G. Gordon, Relative motions between oceanic plates of the Pacific basin, *J. Geophys. Res., 89.B12,* 10,291-10,310, 1984.

Evans, R.L., G. Hirth, K. Baba, D. Forsyth, A. Chave, and R. Mackie, Geophysical evidence from the MELT area for compositional controls on oceanic plates, *Nature*, 437, 249-252, 2005.

Forsyth, D. W., S. C. Webb, L. M. Dorman, and Y. Shen, Phase velocities of Rayleigh waves in the MELT experiment on the East Pacific Rise, *Science, 280*, 1235-1238, 1998.

Forsyth, D. W., and A. Li, Array-analysis of two-dimensional variations in surface wave phase velocity and azimuthal anisotropy in the presence of multi-pathing interference, in *SeismicEarth: Array analysis of Broadband Seismograms, Geophys. Monogr. Ser*., vol. 157, edited by A. Levander and G. Nolet, pp. 81-97, AGU, Washington, D. C., 2005.

Gilbert, H., Yang, Y., Forsyth, D.W., Jones, C., Owens, T., Zandt, G., and Stachnik, J., 2012, Imaging lithospheric foundering in the structure of the Sierra Nevada: Geosphere, doi:10.1130/GES00790.1.

Hess, H. H., History of ocean basins, *Petrologic Studies: A volume to honor A. F. Buddington*, 599 –620, 1962.

Harmon, N., D.W. Forsyth, D.S. Weeraratne, Thickening of young Pacific lithosphere

from high-resolution Rayleigh wave tomography: A test of the conductive cooling model, Earth and Planet. Sci Lett., 278, 96-106, 2009.

Huene, R. V., Geologic structure between the Muray fracture zone and the Tranverse Ranges, *U.S.G.S, Menlo Park, Calif., marine geol*., 7, 475-499, 1969

Kohler, M. D., and P. Davis, Crustal thickness variations in southern California from Los Angeles Region Seismic Experiment passive phase teleseismic travel time, *Bull. Seismol. Soc. Am*., 87, 1330 –1344, 1997.

Kohler, M. D., Lithospheric deformation beneath the San Gabriel Mountains in the southern California Transverse Ranges, *J. Geophys. Res.*, Vol 104, No.B7, 15,025-15,041, 1999.

Kohler, M. D., H. Magistrale, and R. W. Clayton, Mantle heterogeneities and the SCEC Three-Dimensional Seismic Velocity Model Version 3, *Bull. Seis. Soc. Am.*, *93*, 757-774, 2003.

Kohler, M. D., ALBACORE OBS deployment cruise report, R/V Melville Cruise MV1010, August 14-27, 2010.

Kohler, M. D., ALBACORE OBS Recovery Cruise Report, R/V New Horizon Cruise NH1111, September 7-16, 2011

Kosarian, M., P. M. Davis, T. Tanimoto, and R. W. Clayton,The relation between uppper mantle anisotropic structures beneath California, transpression, and absolute plate motions, *J. Geophys*. *Res.,*Vol 116 , B08307, doi:10.1029/2010JB007742, 2011.

Legg, M. R., M. Kohler, D. Weeraratne, and N. Shintaku, High-resolution mapping and analysis of borderland faults using multibeam bathymetry data, Annual SCEC Meeting Proceedings and Abstracts, 2012.

Lekic, V., S. W. French and K. Fischer, Lithospheric thinning beneath rifted regions of southern California, *Science, 334*, 783, doi:10.1126/science.1208898, 2011.

Liu, Z., and P. Bird, North America plate is driven westward by lower mantle flow, *Geophys*. *Res. Lett.,*Vol 29 , No. 24, 2164, doi:10.1029/2002GL016002, 2002.

Liu, H., P. M. Davis, and S. Gao, SKS splitting beneath Southern California*, Geophys Res. Lett., 22*, 767-770, 1995.

Luyendyk, B. P., A model for Neogene crustal rotations, transtension, and transpression in southern California, *Geol. Soc. Am. Bull., 103*, 1528-1536, 1991.

Nazareth, J. J., and R. Clayton, Crustal structure of the Borderland-Continent transition

zone of southern California adjacent to Los Angeles, *J. Geophys*., 108, B8, 2404 doi:10.1029/2001JB000223, 2003.

Nicholson, C., C. C. Sorlien, T. Atwater, J. C. Crowell, and B. P. Luyenkyk, Microplate capture, rotation of the western Transverse Ranges, and initiation of the San Andreas transform as a low-angle fault system, *Geology, 22*, 491-495, 1995

Nishimura, C. E., and D. W. Forsyth, Rayleigh wave phase velocities in the Pacific with implications for azimuthal anisotropy and lateral heterogeneities, *Geophys. J., 94*, 479-501-327, 1988.

Parsons, B., and J. G. Sclater, An analysis of the variation of ocean floor bathymetry and heat flow with age, *J. Geophys. Res.,* Vol. 82, No. 5, 803-827, 1977.

Polet, J., and H. Kanamori, Anisotropy beneath California: shear wave splitting measurements using a dense broadband array, *Geophys. J. Int., 149*, 313-327, 2002.

Rudnick, Roberta L., Making Continental Crust, Nature, vol. 378, 571-578, 1995.

Silver, P. G., and W. E. Holt, The mantle flow field beneath western North America, *Science, 295*, 1054-1057, 2002.

Shintaku, N., D. S. Weeraratne, and M. D. Kohler, Seafloor bathymetry and gravity from the ALBACORE marine seismic experiment offshore southern California, AGU Fall Meeting abstract, 2010.

Saleeby, J., Le Pourhiet, L., Saleeby, Z., and Gurnis, M., 2012, Epeirogenic transients related to mantle lithosphere removal in the southern Sierra Nevada region, California, part I: Implications of thermomechanical modeling Geosphere, doi:10.1130/GES00746.1

Smith, W. H. F., and D. T. Sandwell, Global seafloor topography from satellite altimetry and ship depth soundings, Science, v. 277, p. 1957-1962, 26 Sept, 1997.

Smith, M. L., and F. A. Dahlen, The azimuthal depence of Love and Rayleigh wave propagation in a slightly anisotropic medium, *J. Geophys. Res., 78*, 3321-3333, 1973.

Stein, C. A., and S. Stein, A model for the global variation in oceanic depth and heat-flow with lithosphere age, *Nature, 359*, 123-129, doi:10.1038/359123a0, 1992.

ten Brink, U. S., J. Zhang, T. M. Brocher, D. A. Okaya, K. D. Klitgord, and G. S. Fuis, Geophysical evidence for the evolution of the California Inner Continental Borderland as a metamorphic core complex, *J. Geophys. Res., 105*, 5835-5857, 2000.

Tutcotte, D.L., and G. Schubert, Geodynamics, 2nd ed., Cambridge Univ. Press, 2002

Weeraratne, D. S., D. W. Forsyth, Y. Yang, and S. C. Webb, Rayleigh wave tomography beneath intraplate volcanic ridges in the South Pacific, J. Geophys. Res., 112, B06303, doi:10.1029/2006JB004403, 2007.

Yang, Y., and D. W. Forsyth, Rayleigh wave phase velocities, small-scale convection, and azimuthal anisotropy beneath southern California, *J. Geophys. Res., 111*, B07306, doi:10.1029/2005JB004180, 2006a.

Yang, Y., and D. W. Forsyth, Regional tomographic inversion of the amplitude and phase of Rayleigh waves with 2-D sensitivity kernels, *Geophys. J. Int., 166*, 1148–1160, 2006b.

Yeats, R. S., Souther California structure, Sea-Floor-spreading, and history of the Pacific basin, *Geol. Soc. Am. Bull.,* v. 79, 1693-1702, 1968

Zandt, G., and E. Humpreys, Toroidal mantle flow through the western U.S. Slab window, *Geol. Soc. Am*, v.36; no.4; p. 295-298; doi:10.1130/G24611A, 2008

Zhu, L., and H. Kanamori, Moho depth variation in Southern California from teleseismic receiver functions, *J. Geophys. Res*., *105,* 2969-2980, 2000.

Appendix A: Amplitude Correction Plots

Ocean Bottom Seismometer (OBS)

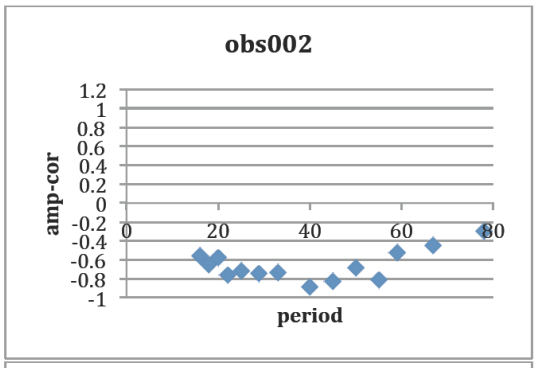

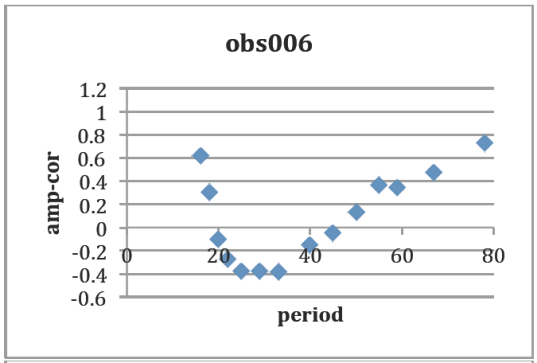

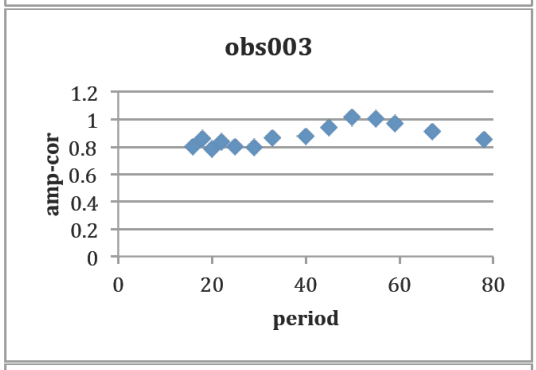

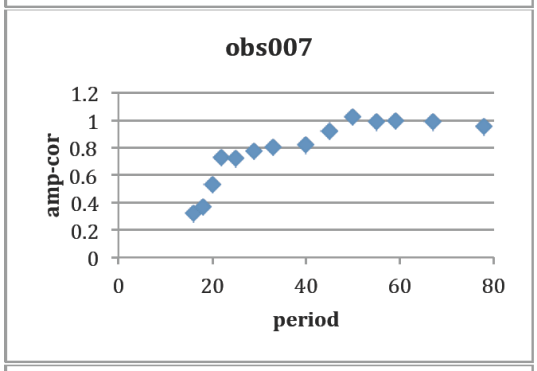

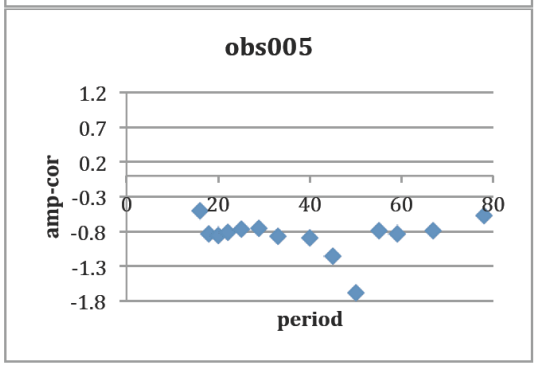

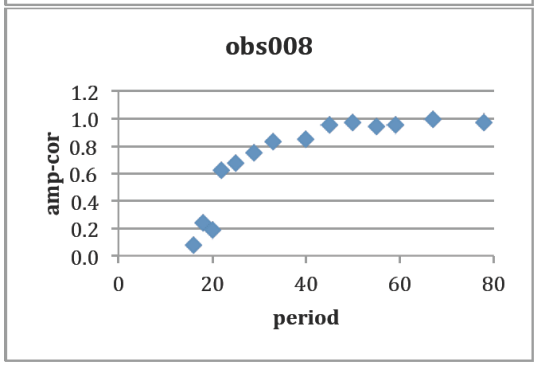

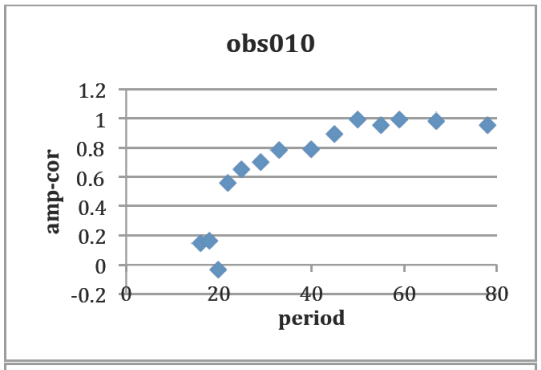
obs010
amp-cor
period

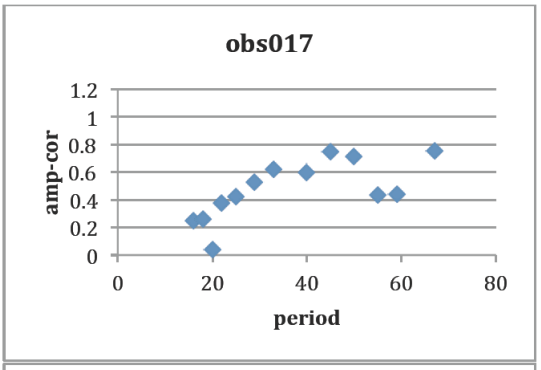
obs017
amp-cor
period

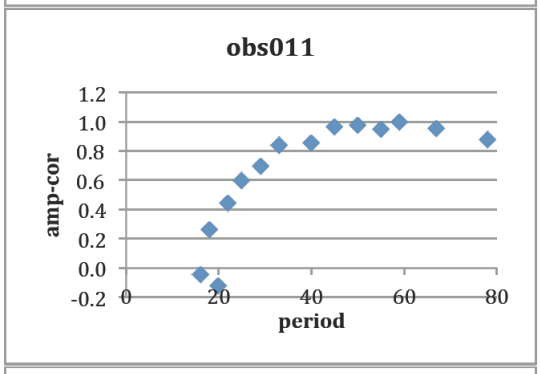
obs011
amp-cor
period

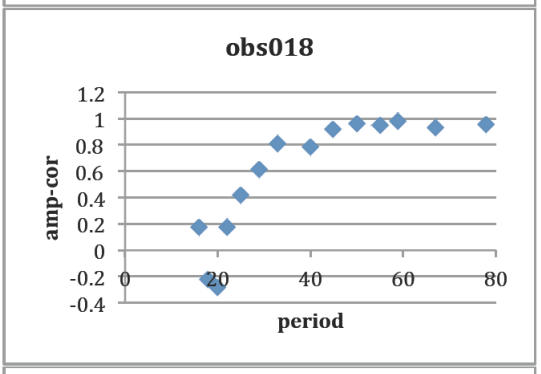
obs018
amp-cor
period

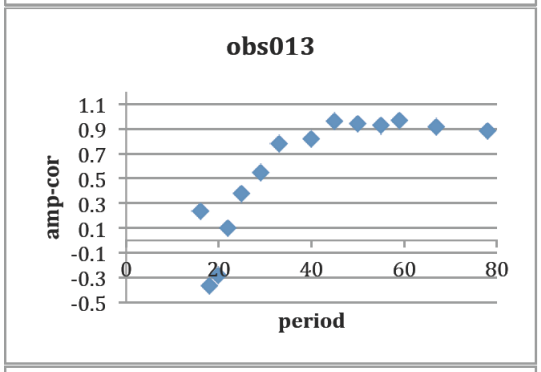
obs013
amp-cor
period

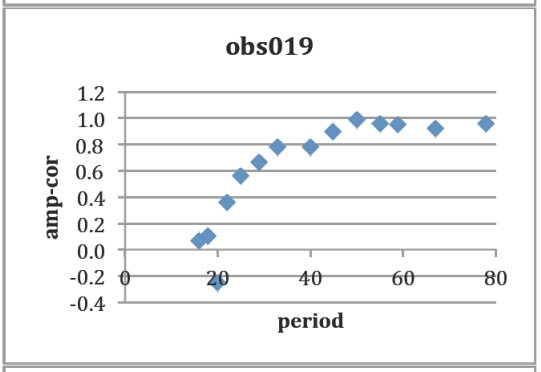
obs019
amp-cor
period

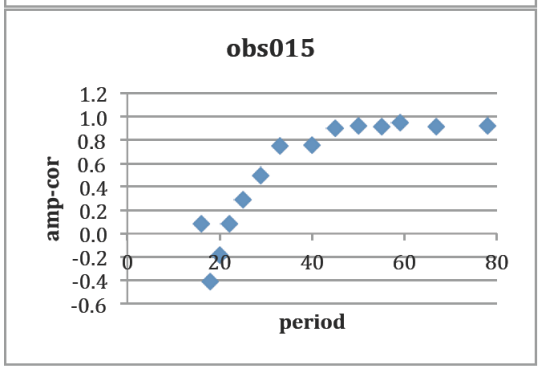
obs015
amp-cor
period

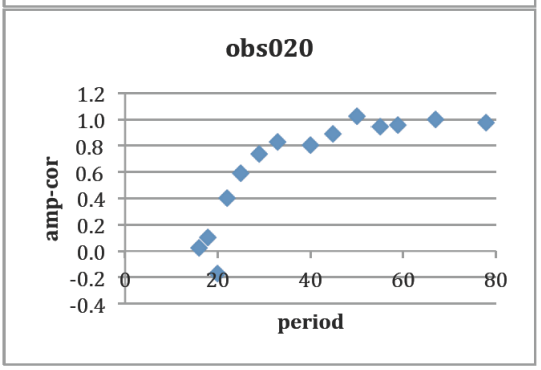
obs020
amp-cor
period

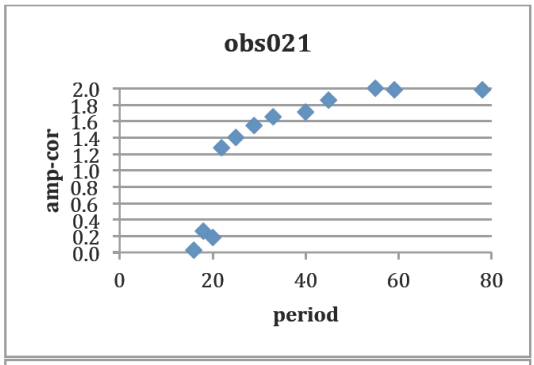
obs021
amp-cor
period

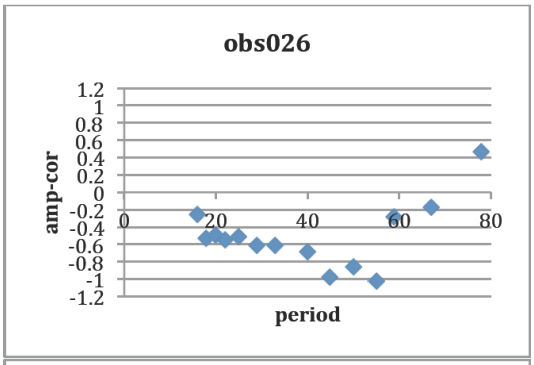
obs026
amp-cor
period

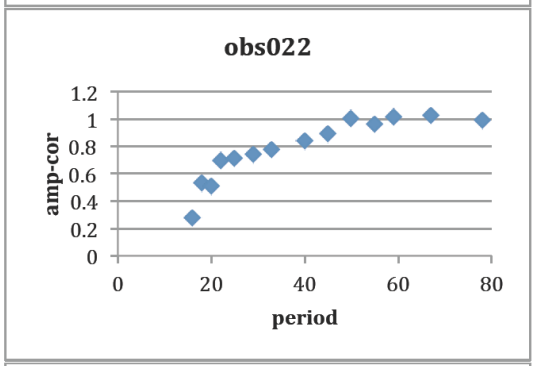
obs022
amp-cor
period

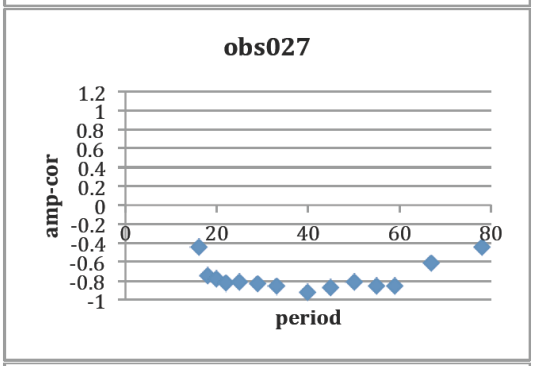
obs027
amp-cor
period

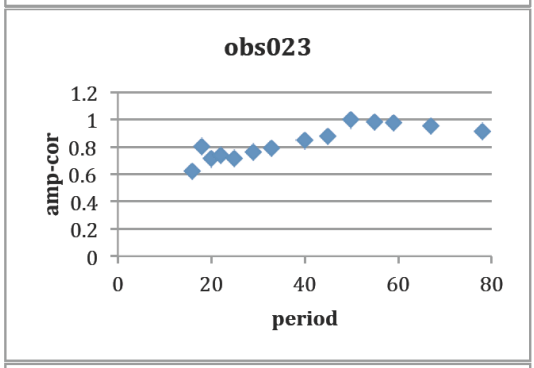
obs023
amp-cor
period

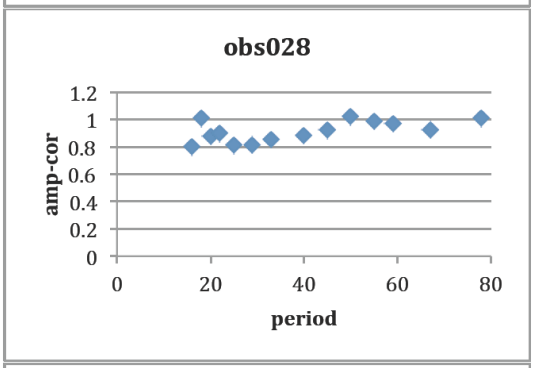
obs028
amp-cor
period

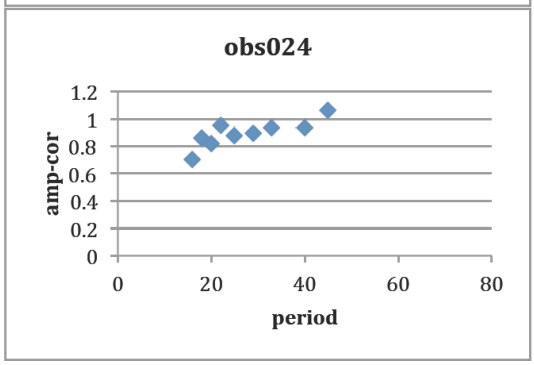
obs024
amp-cor
period

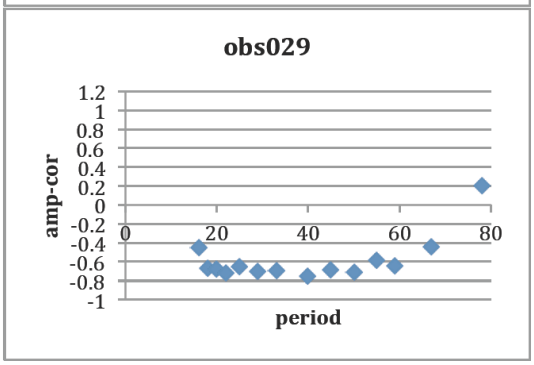
obs029
amp-cor
period

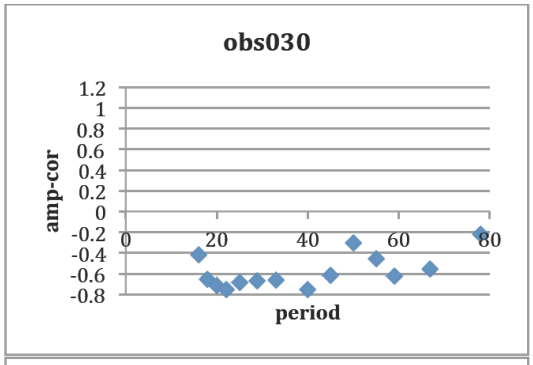
obs030
amp-cor
period

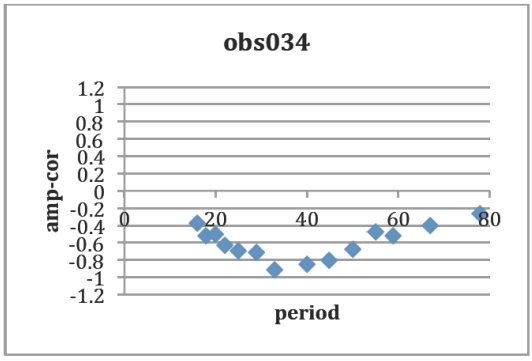
obs034
amp-cor
period

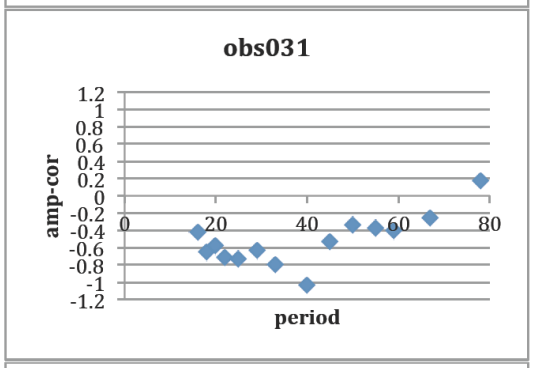
obs031
amp-cor
period

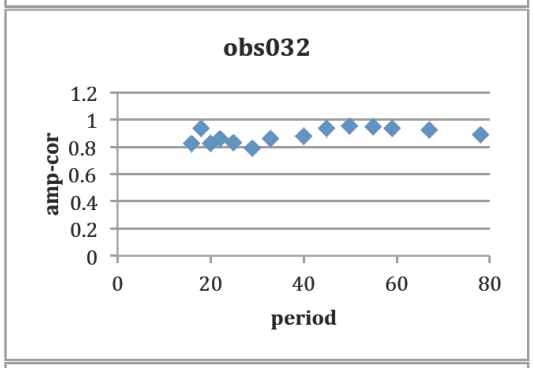
obs032
amp-cor
period

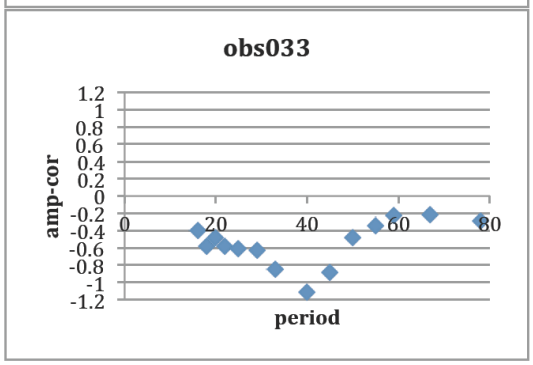
obs033
amp-cor
period

Land Stations

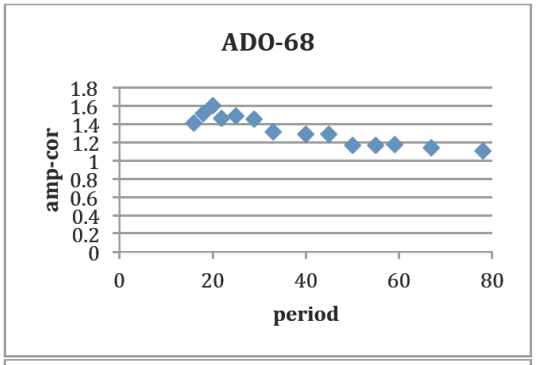

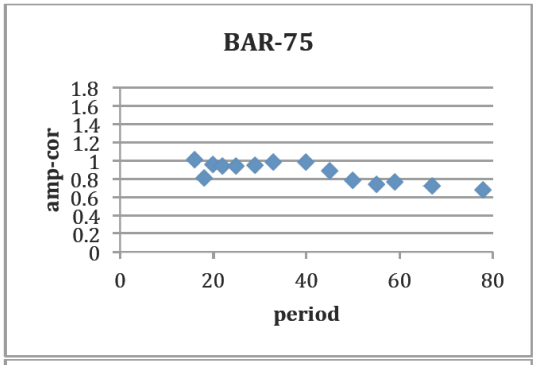

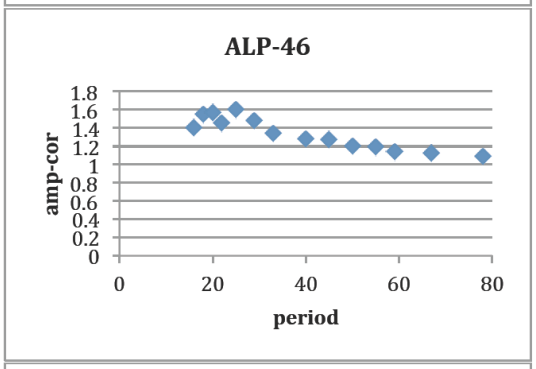

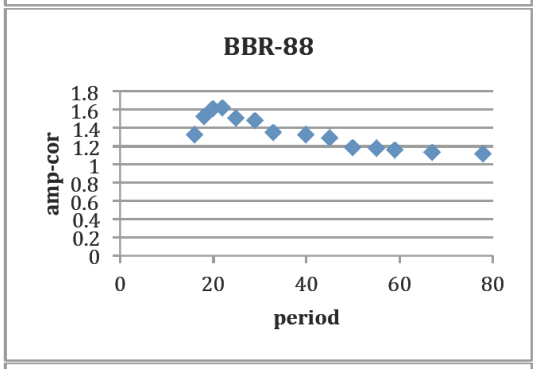

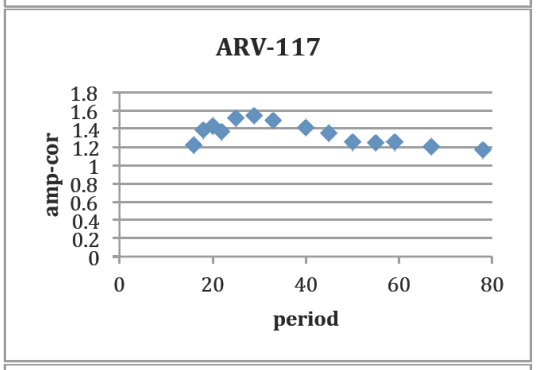

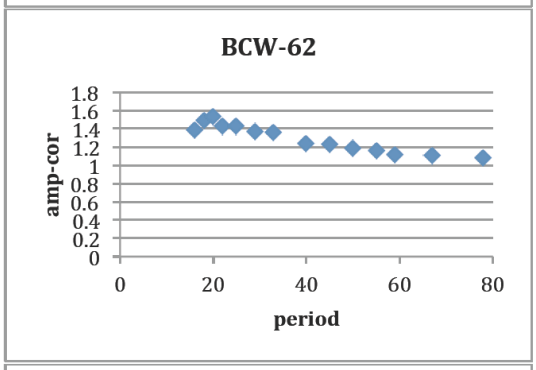

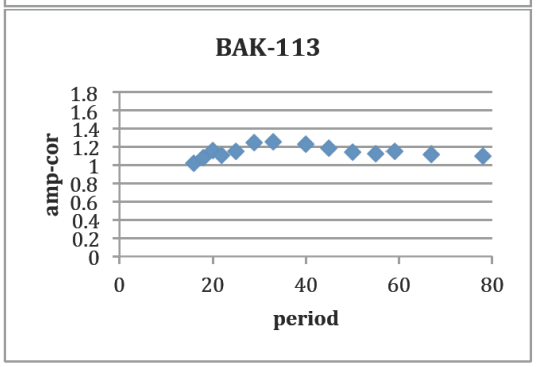

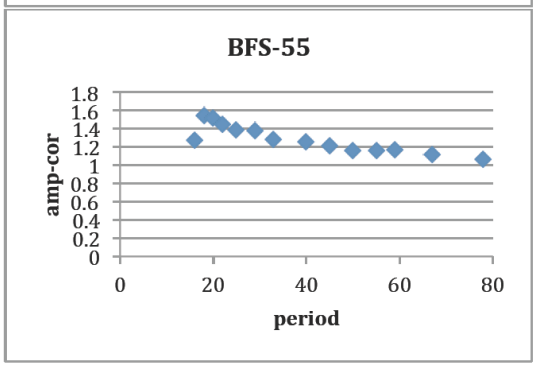

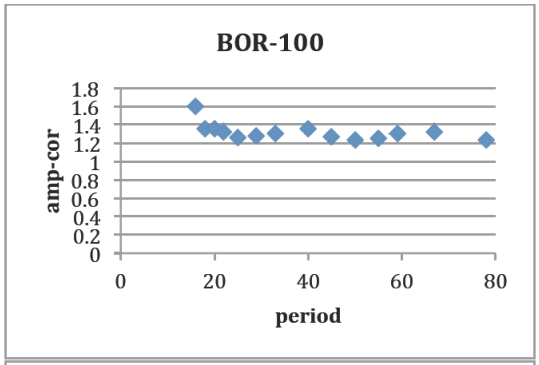
BOR-100
amp-cor
period

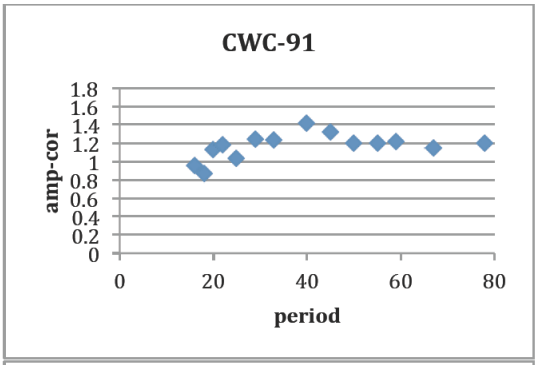
CWC-91
amp-cor
period

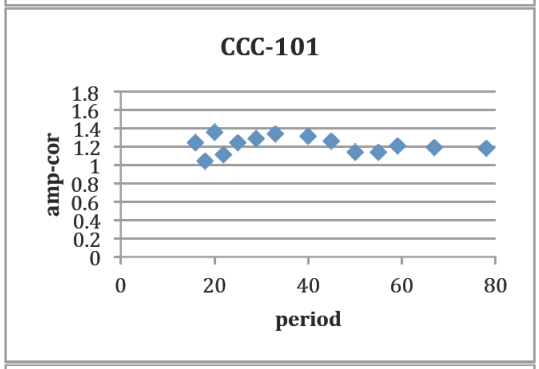
CCC-101
amp-cor
period

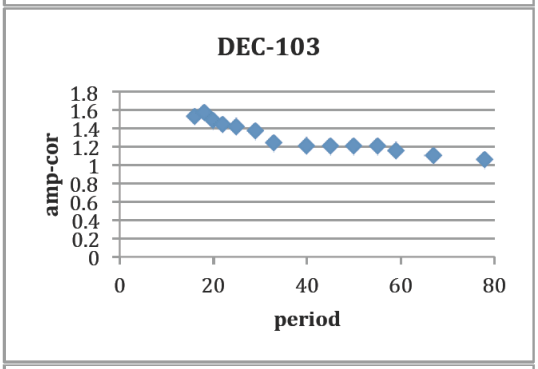
DEC-103
amp-cor
period

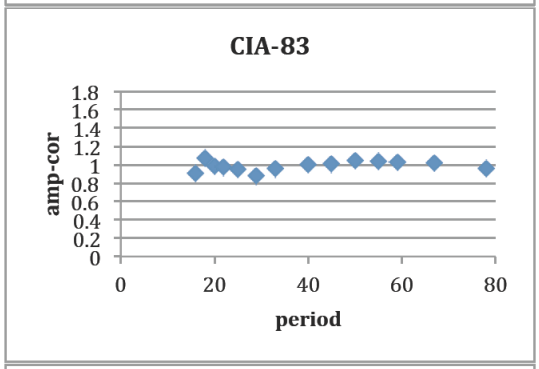
CIA-83
amp-cor
period

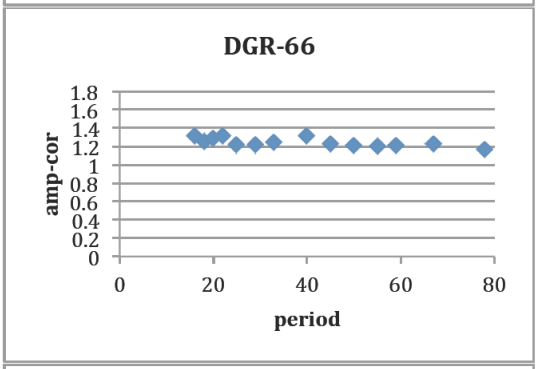
DGR-66
amp-cor
period

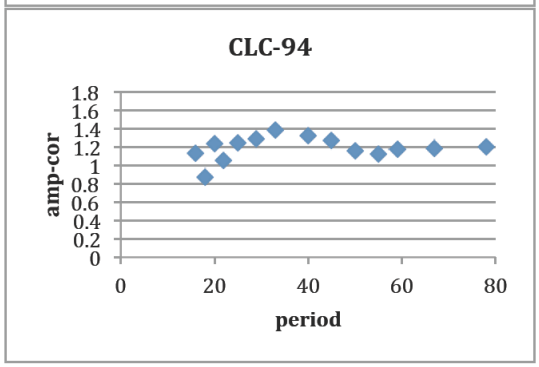
CLC-94
amp-cor
period

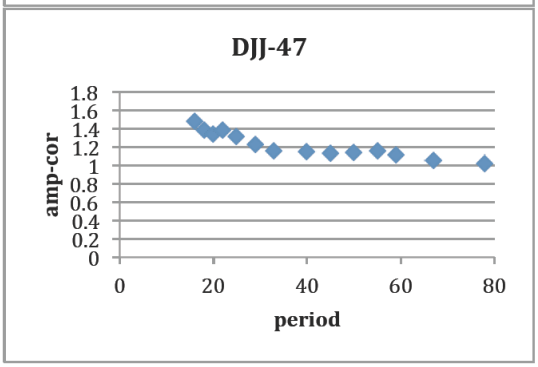
DJJ-47
amp-cor
period

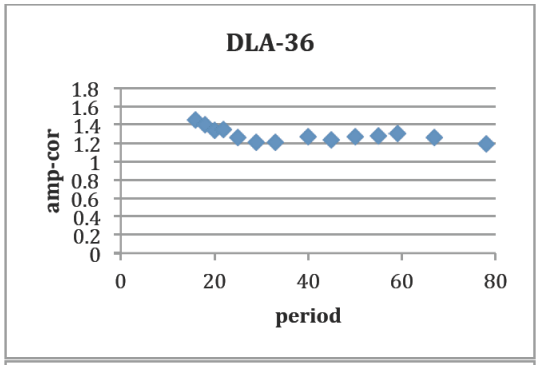
DLA-36
amp-cor
period

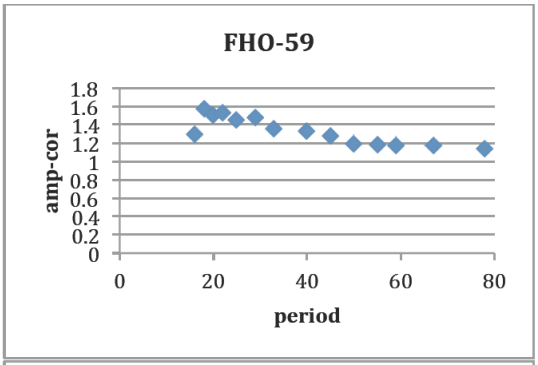
FHO-59
amp-cor
period

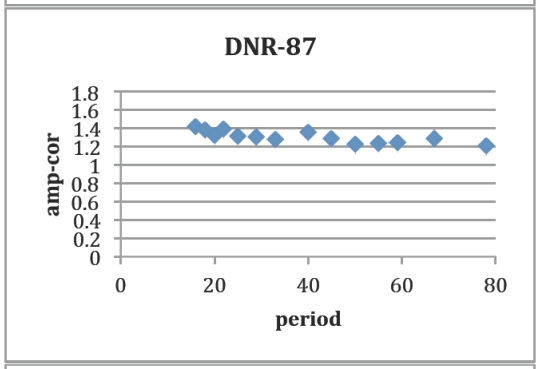
DNR-87
amp-cor
period

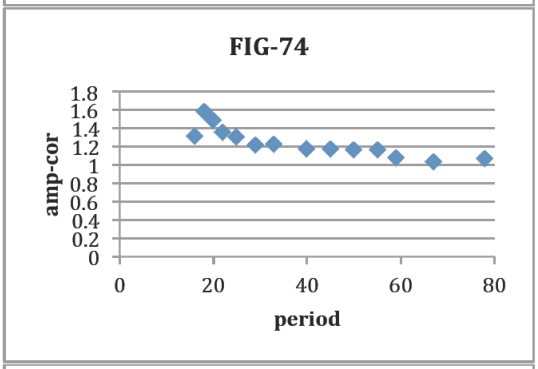
FIG-74
amp-cor
period

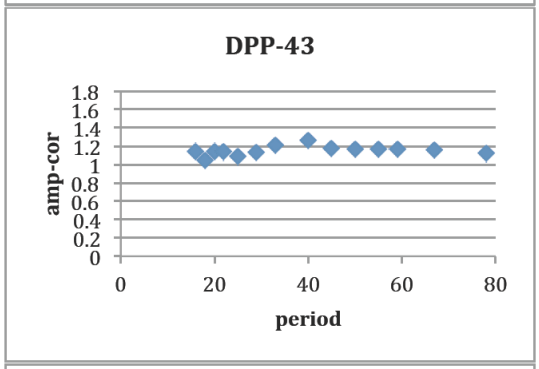
DPP-43
amp-cor
period

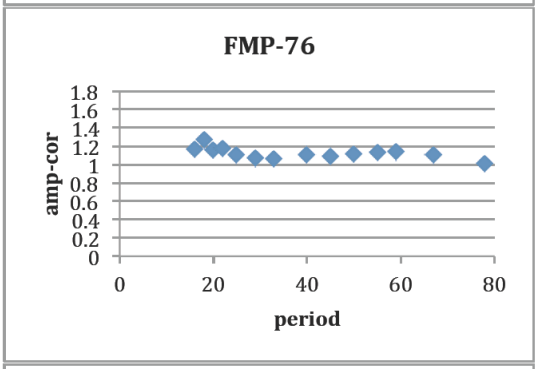
FMP-76
amp-cor
period

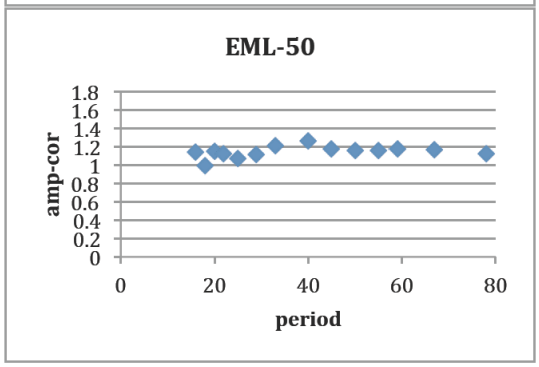
EML-50
amp-cor
period

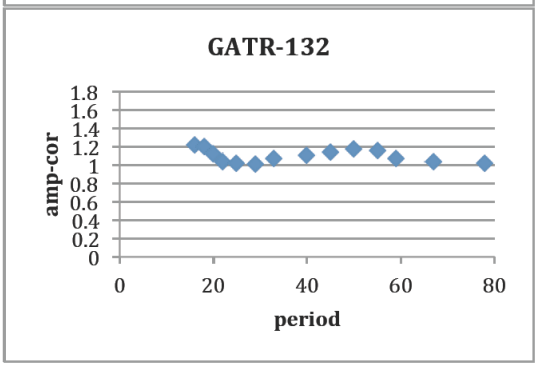
GATR-132
amp-cor
period

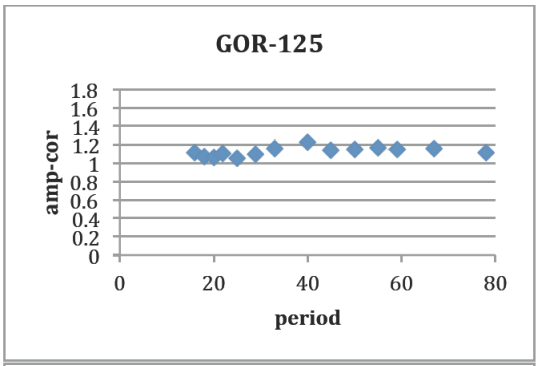
GOR-125
amp-cor
period

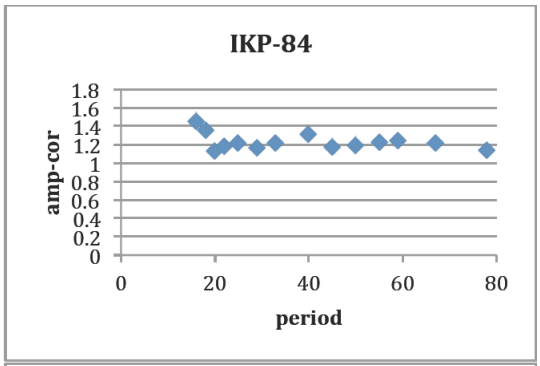
IKP-84
amp-cor
period

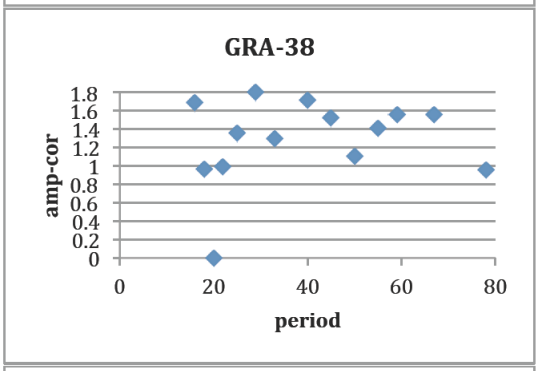
GRA-38
amp-cor
period

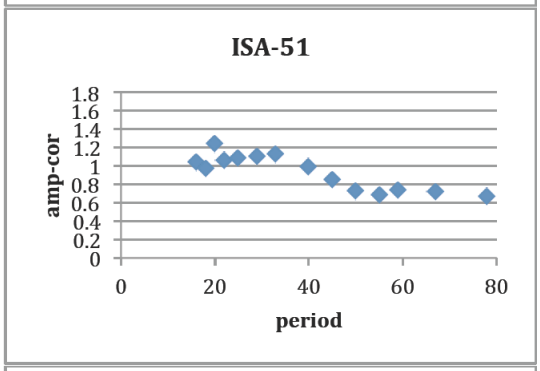
ISA-51
amp-cor
period

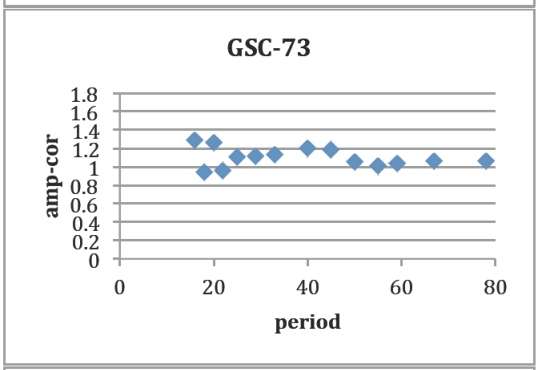
GSC-73
amp-cor
period

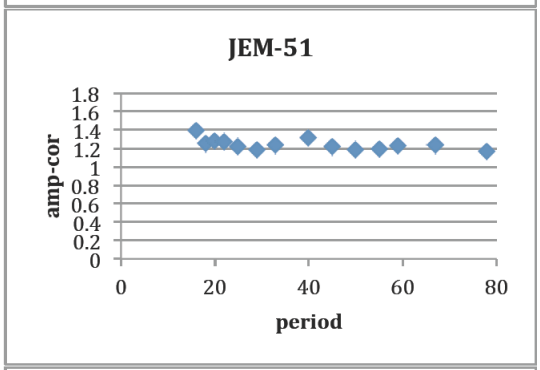
JEM-51
amp-cor
period

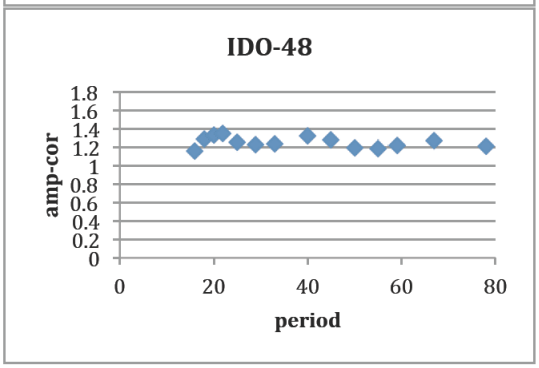
IDO-48
amp-cor
period

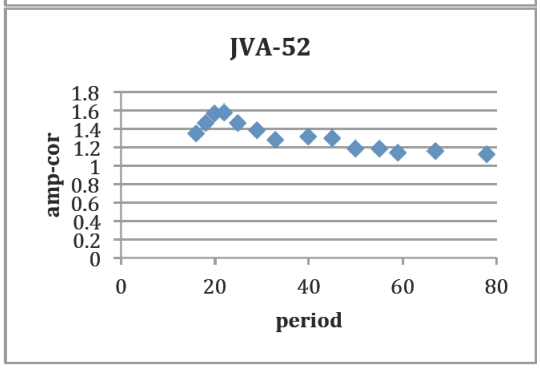
JVA-52
amp-cor
period

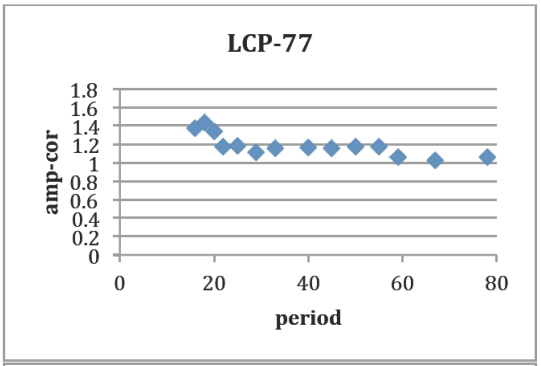
LCP-77
amp-cor
period

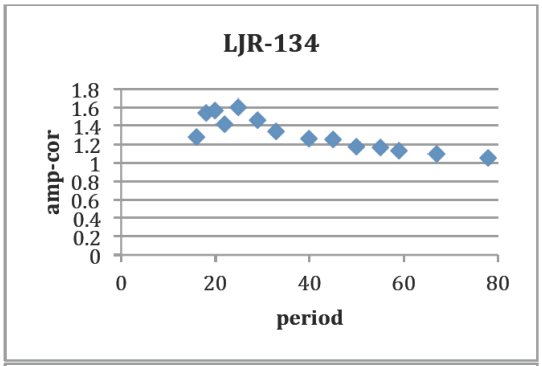
LJR-134
amp-cor
period

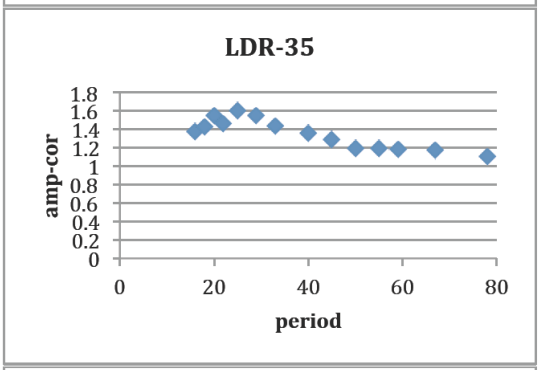
LDR-35
amp-cor
period

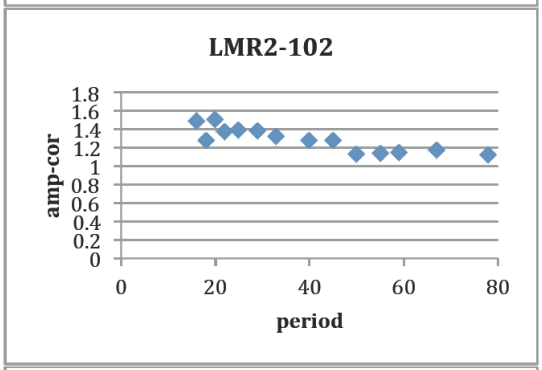
LMR2-102
amp-cor
period

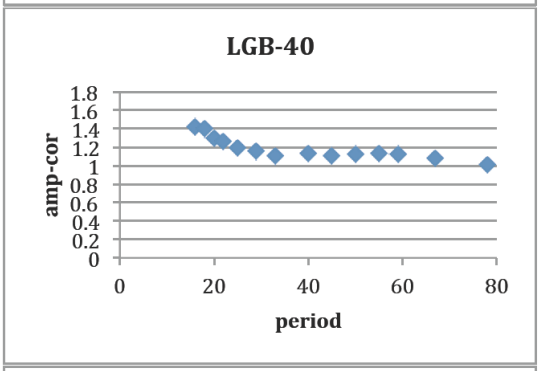
LGB-40
amp-cor
period

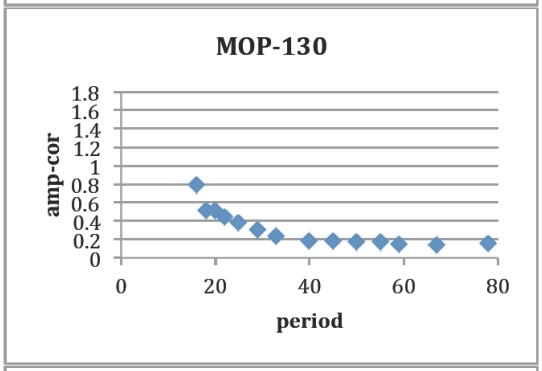
MOP-130
amp-cor
period

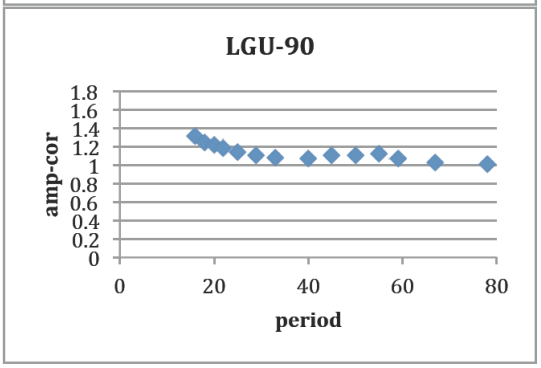
LGU-90
amp-cor
period

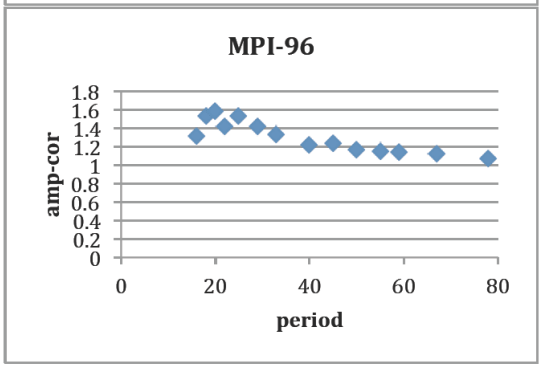
MPI-96
amp-cor
period

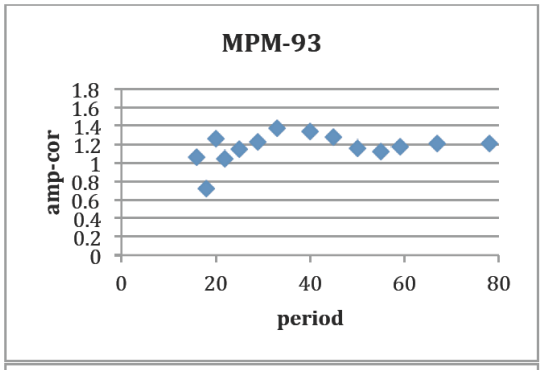
MPM-93
amp-cor
period

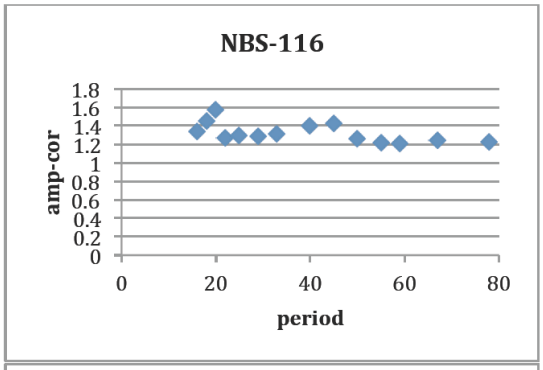
NBS-116
amp-cor
period

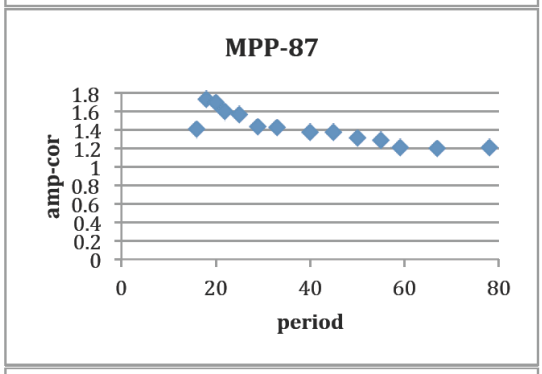
MPP-87
amp-cor
period

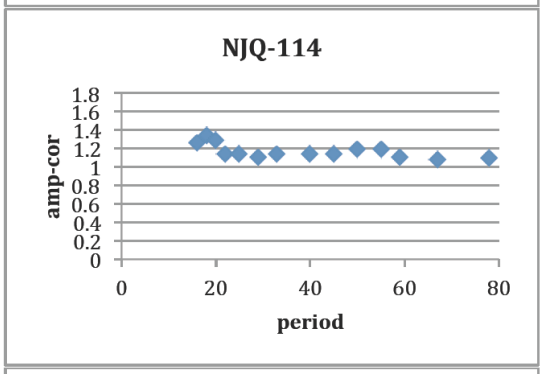
NJQ-114
amp-cor
period

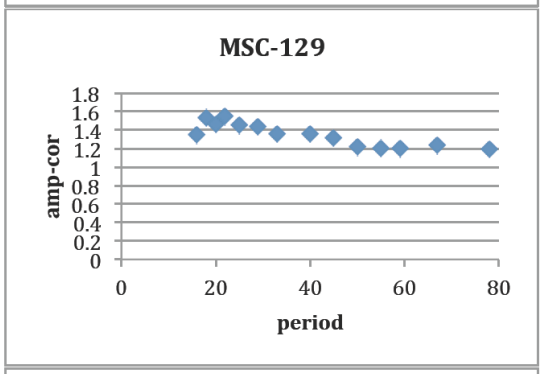
MSC-129
amp-cor
period

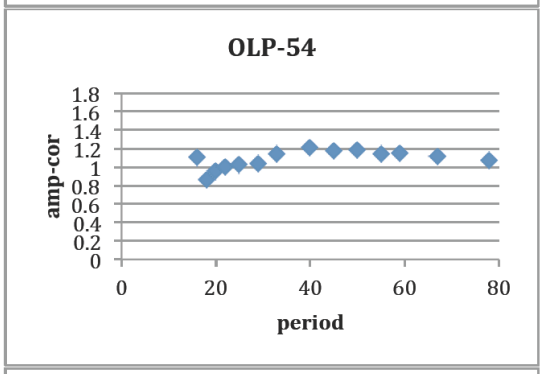
OLP-54
amp-cor
period

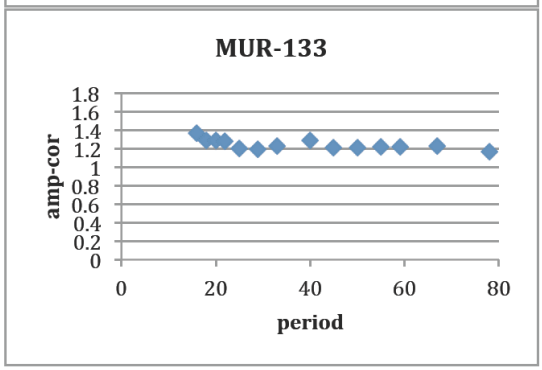
MUR-133
amp-cor
period

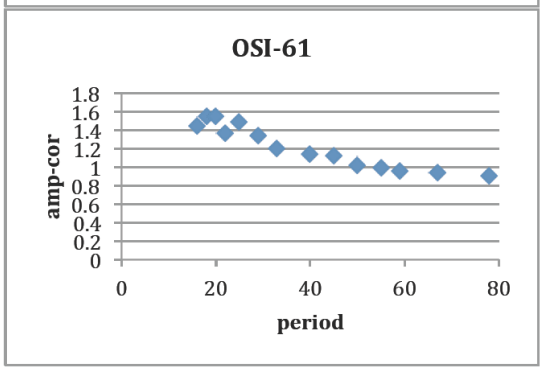
OSI-61
amp-cor
period

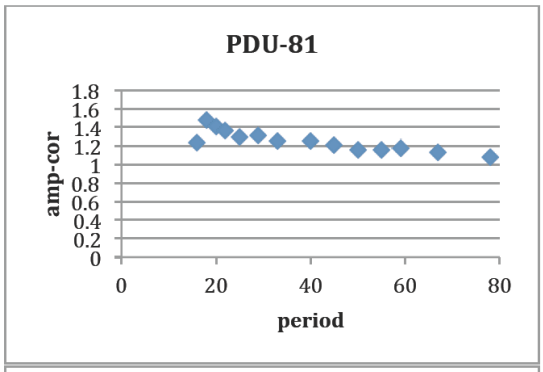
PDU-81
amp-cor
period

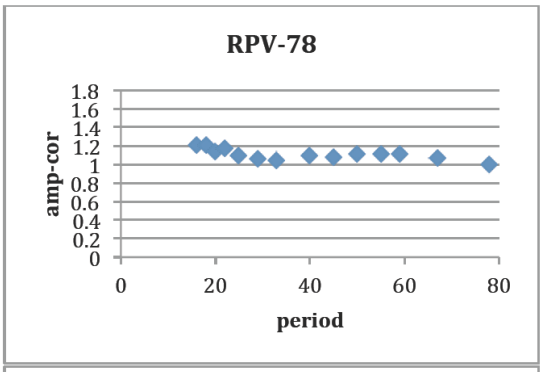
RPV-78
amp-cor
period

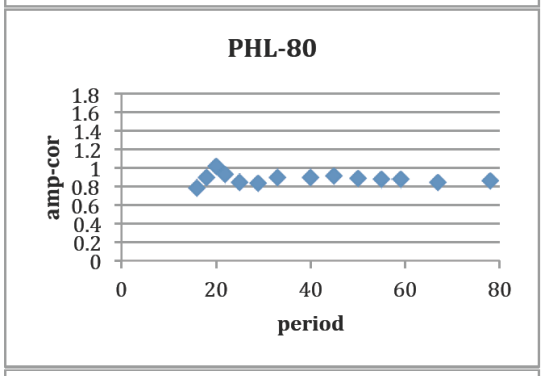
PHL-80
amp-cor
period

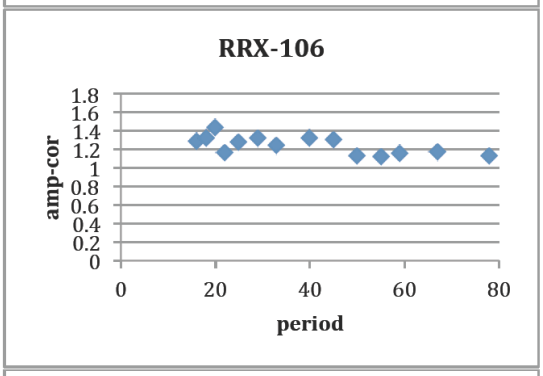
RRX-106
amp-cor
period

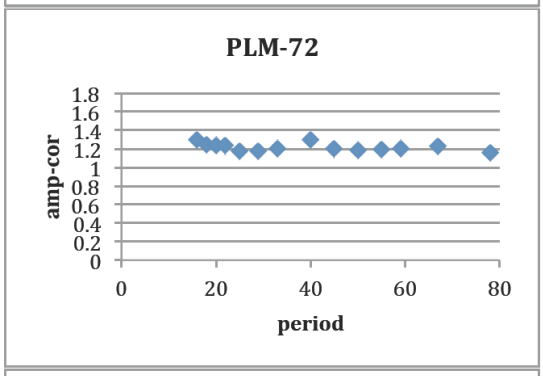
PLM-72
amp-cor
period

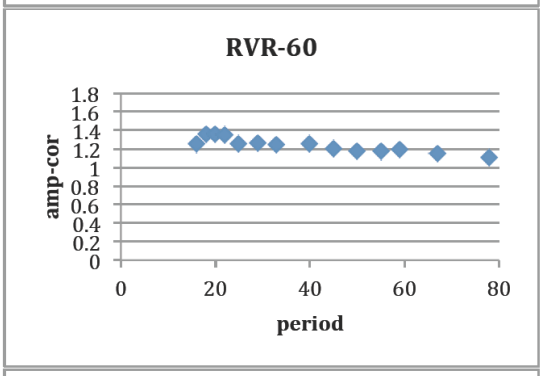
RVR-60
amp-cor
period

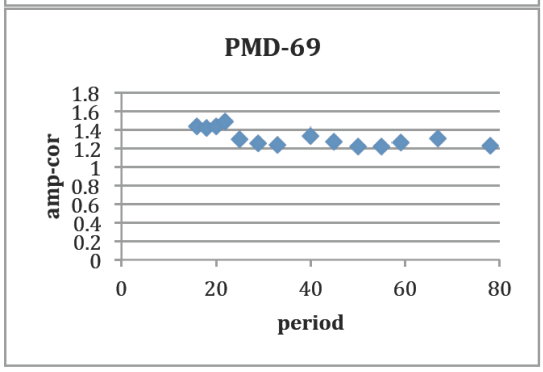
PMD-69
amp-cor
period

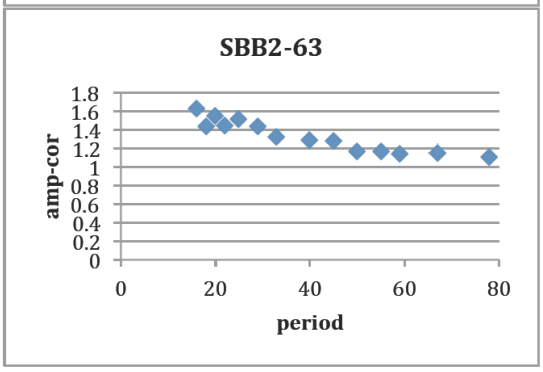
SBB2-63
amp-cor
period

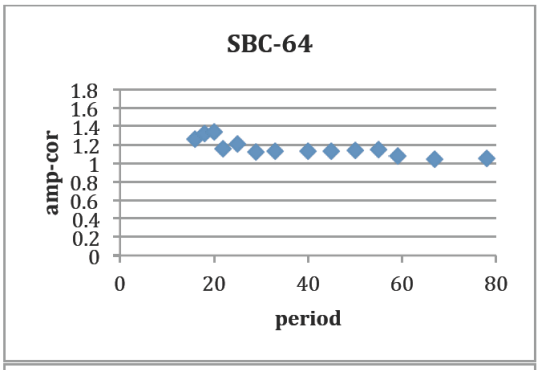
SBC-64
amp-cor
period

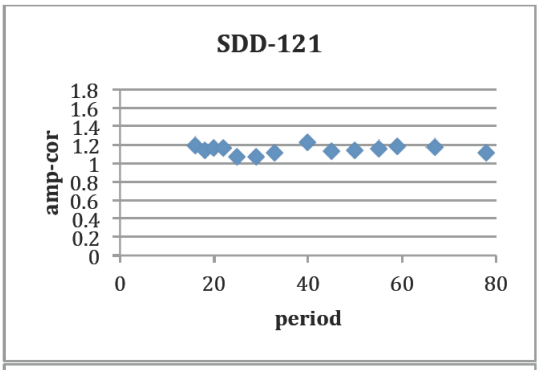
SDD-121
amp-cor
period

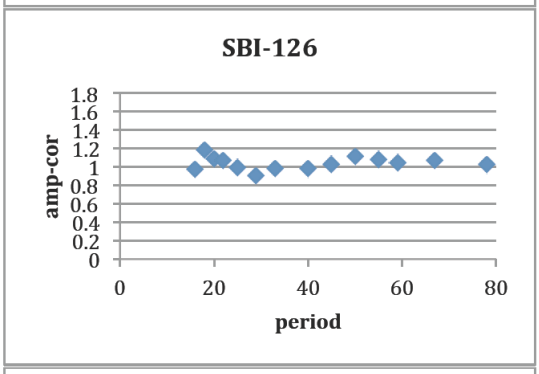
SBI-126
amp-cor
period

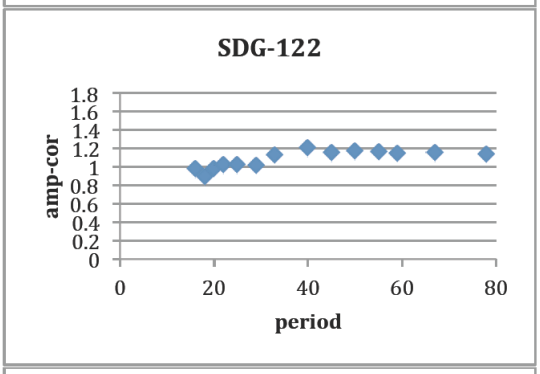
SDG-122
amp-cor
period

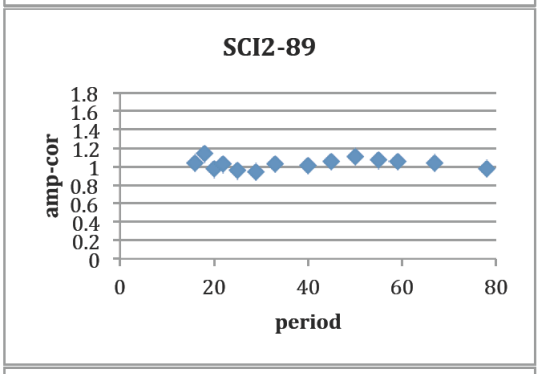
SCI2-89
amp-cor
period

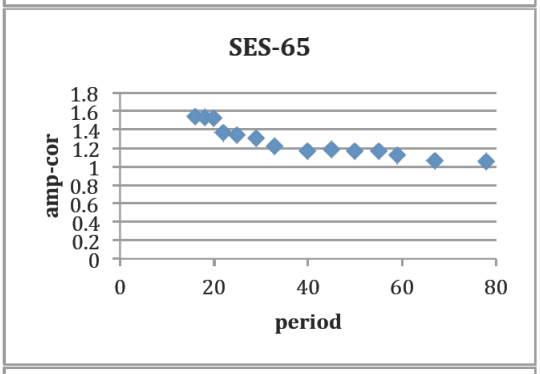
SES-65
amp-cor
period

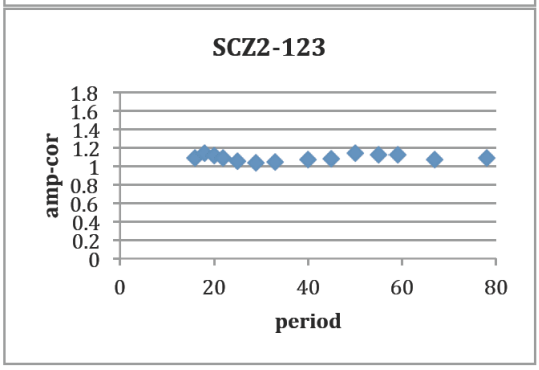
SCZ2-123
amp-cor
period

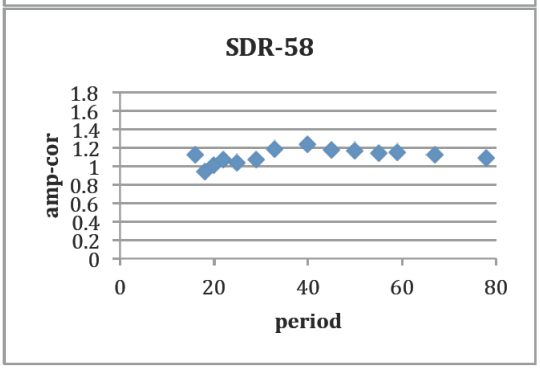
SDR-58
amp-cor
period

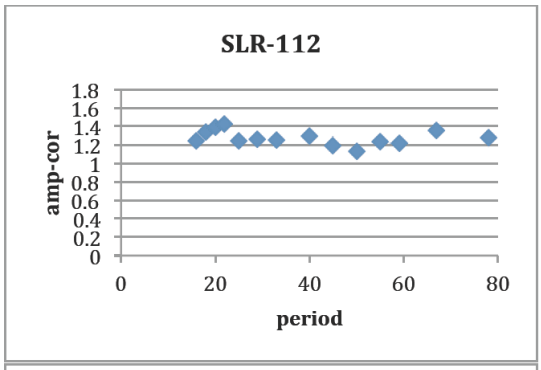
SLR-112
amp-cor
period

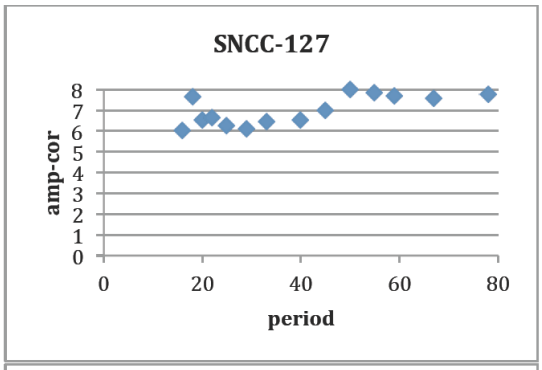
SNCC-127
amp-cor
period

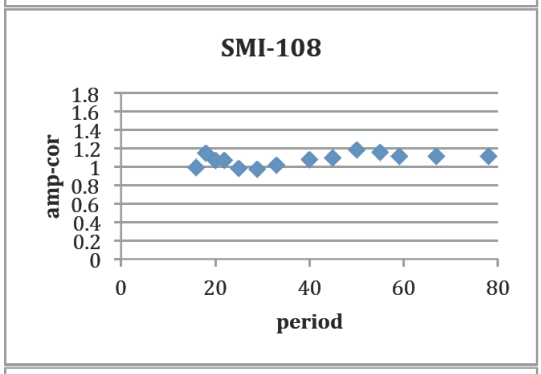
SMI-108
amp-cor
period

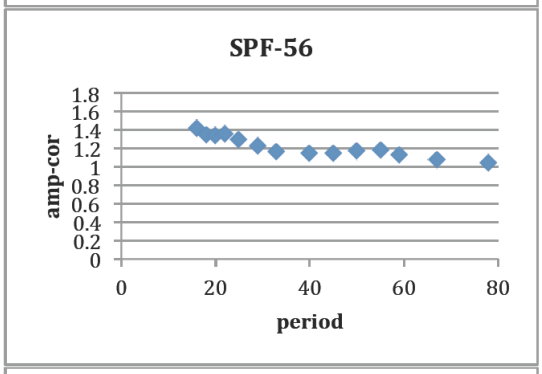
SPF-56
amp-cor
period

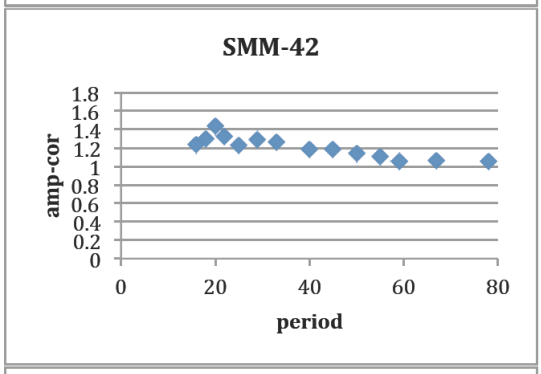
SMM-42
amp-cor
period

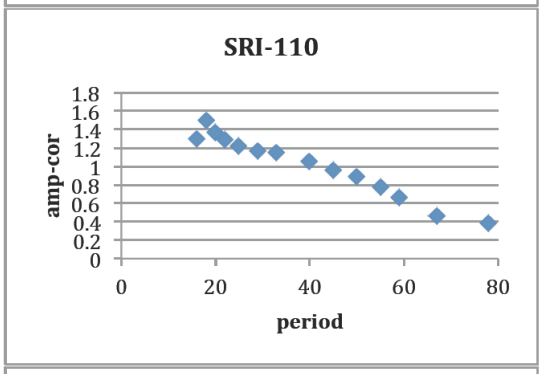
SRI-110
amp-cor
period

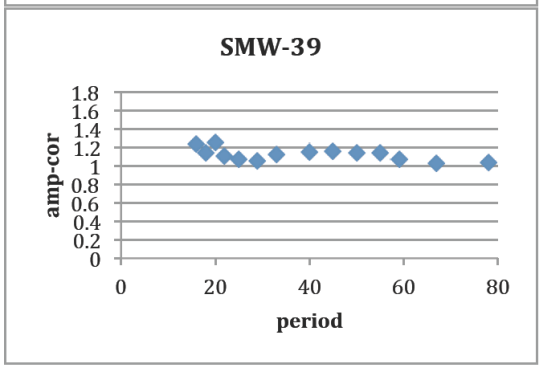
SMW-39
amp-cor
period

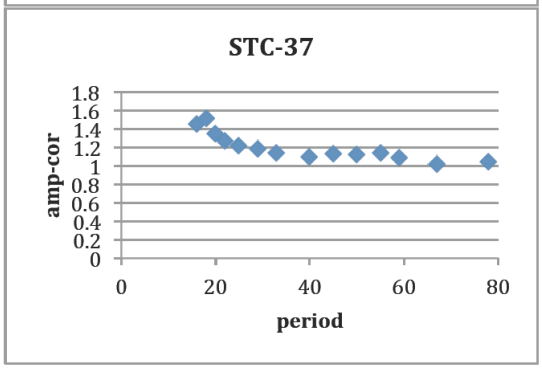
STC-37
amp-cor
period

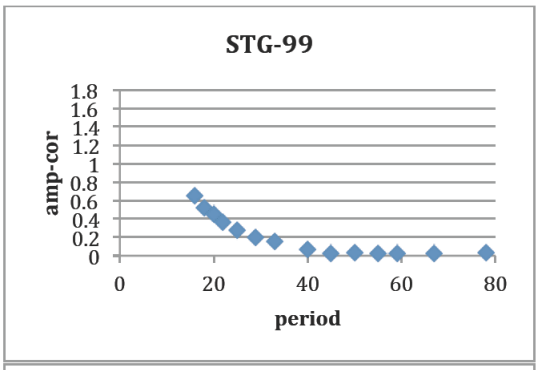
STG-99
amp-cor
period

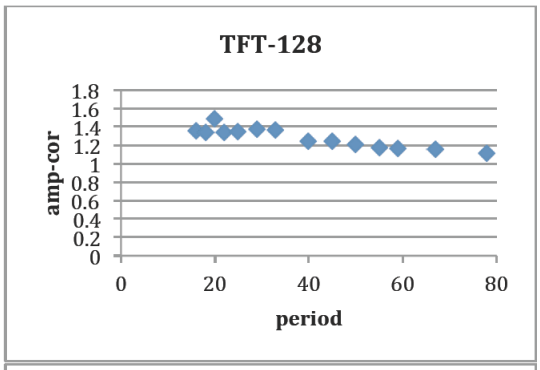
TFT-128
amp-cor
period

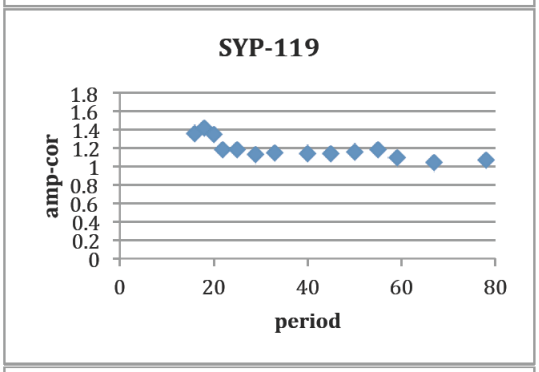
SYP-119
amp-cor
period

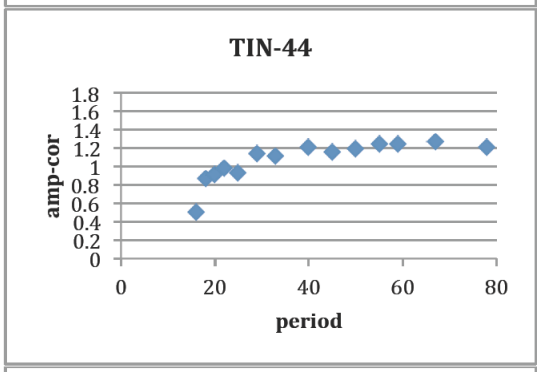
TIN-44
amp-cor
period

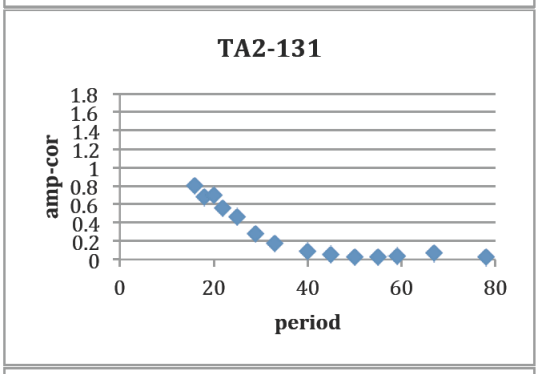
TA2-131
amp-cor
period

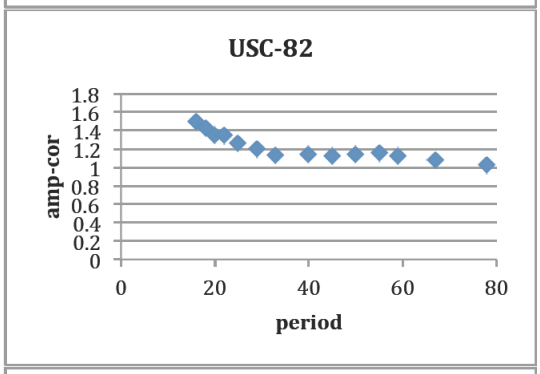
USC-82
amp-cor
period

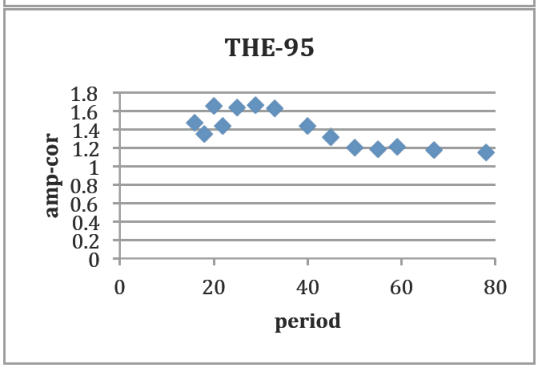
THE-95
amp-cor
period

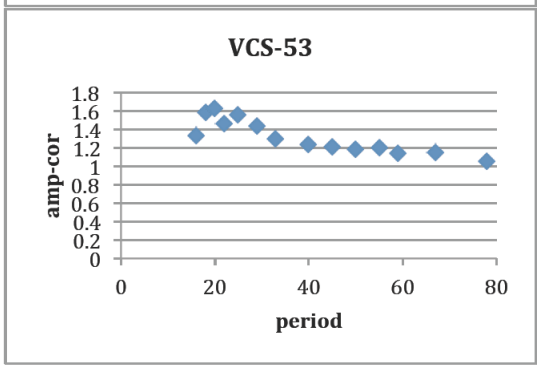
VCS-53
amp-cor
period

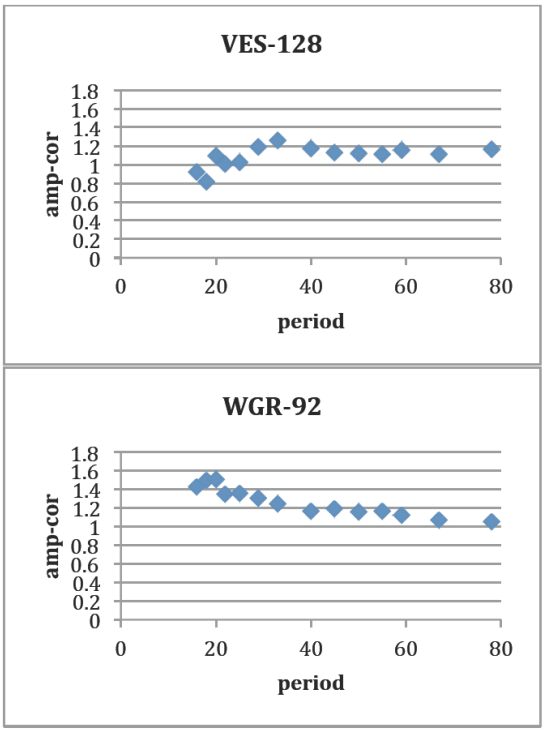
VES-128
amp-cor
1.8
1.6
1.4
1.2
1
0.8
0.6
0.4
0.2
0
0
20
40
60
80
period
WGR-92
amp-cor
1.8
1.6
1.4
1.2
1
0.8
0.6
0.4
0.2
0
0
20
40
60
80
period

Appendix B: 2D Maps

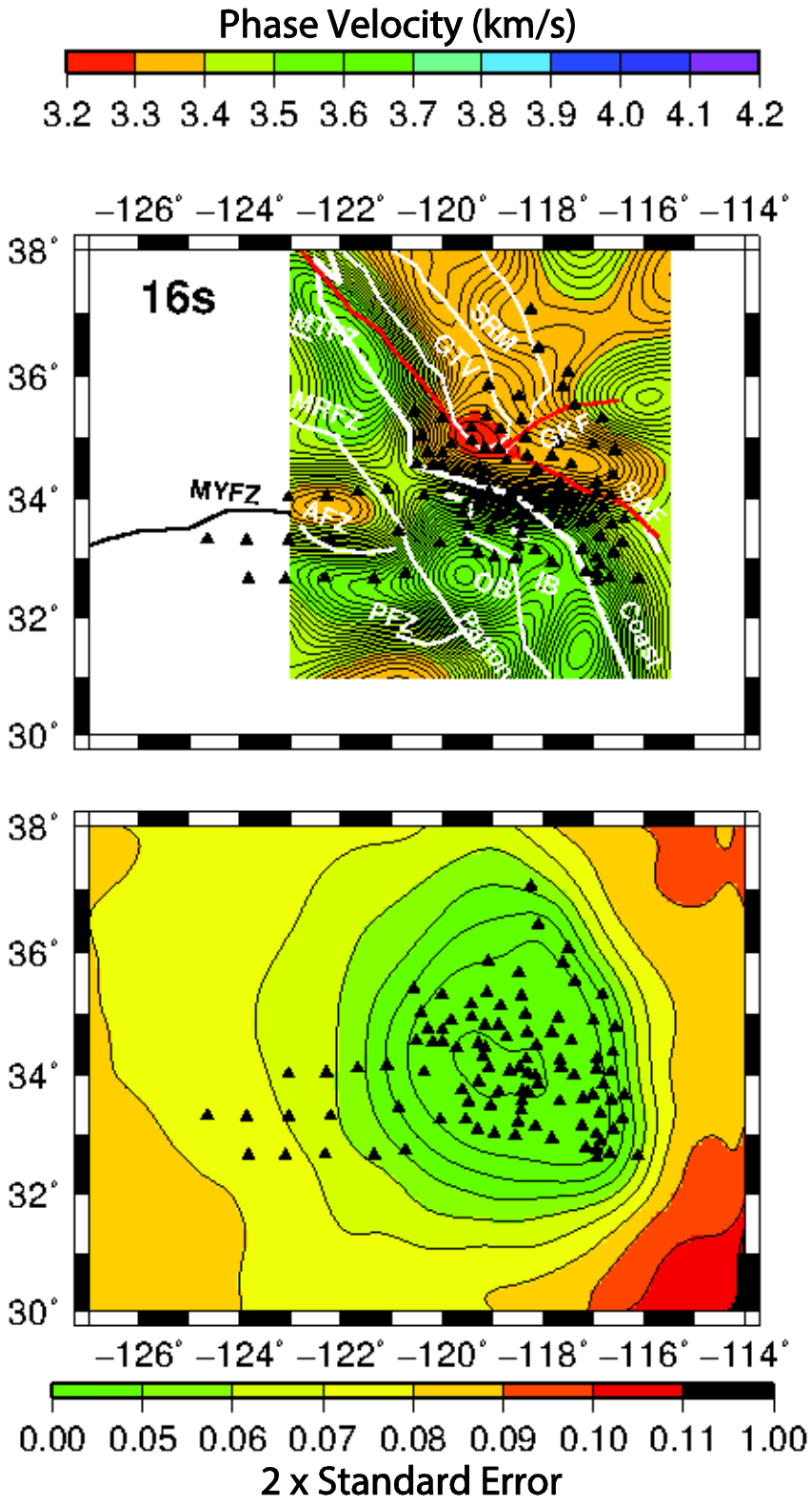

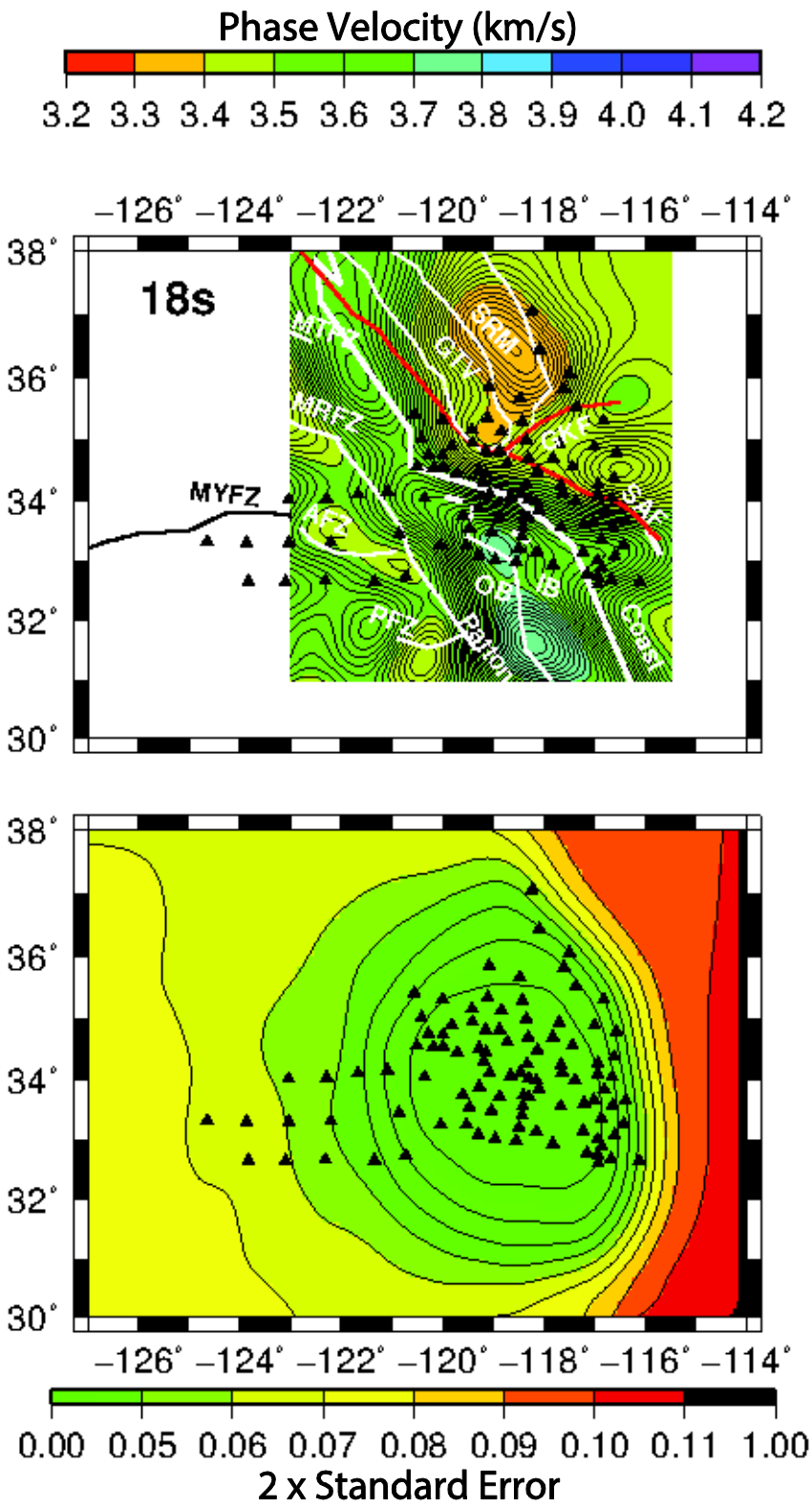
Phase Velocity (km/s)
3.2 3.3 3.4 3.5 3.6 3.7 3.8 3.9 4.0 4.1 4.2
−126° −124° −122° −120° −118° −116° −114°
38° 36° 34° 32° 30°
18s
MYFZ
MRFZ
SRMP
CTY
SAF
Coast
0.00 0.05 0.06 0.07 0.08 0.09 0.10 0.11 1.00
2 x Standard Error

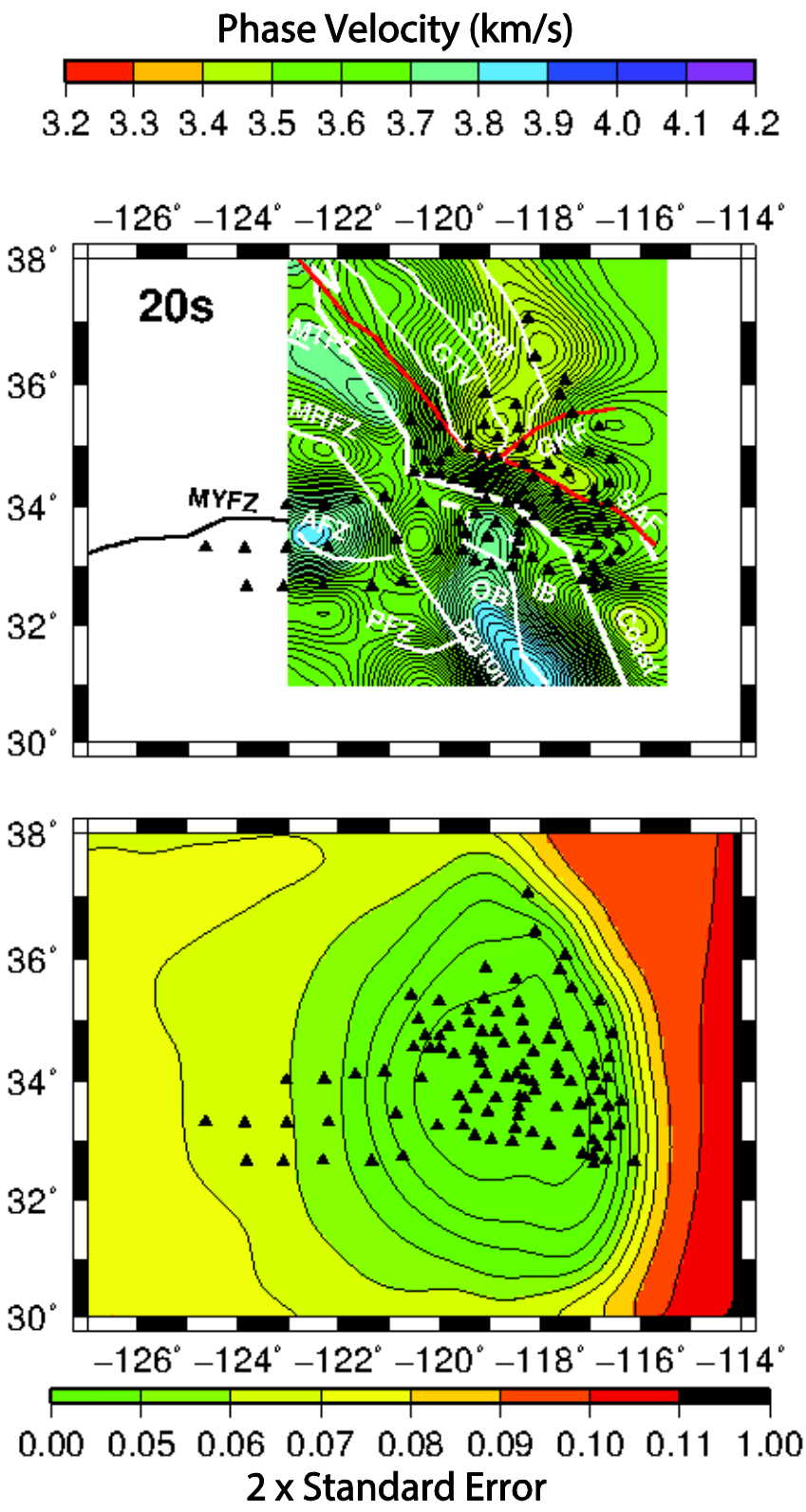
Phase Velocity (km/s)
3.2 3.3 3.4 3.5 3.6 3.7 3.8 3.9 4.0 4.1 4.2
−126° −124° −122° −120° −118° −116° −114°
38° 36° 34° 32° 30°
20s
MYFZ
0.00 0.05 0.06 0.07 0.08 0.09 0.10 0.11 1.00
2 x Standard Error

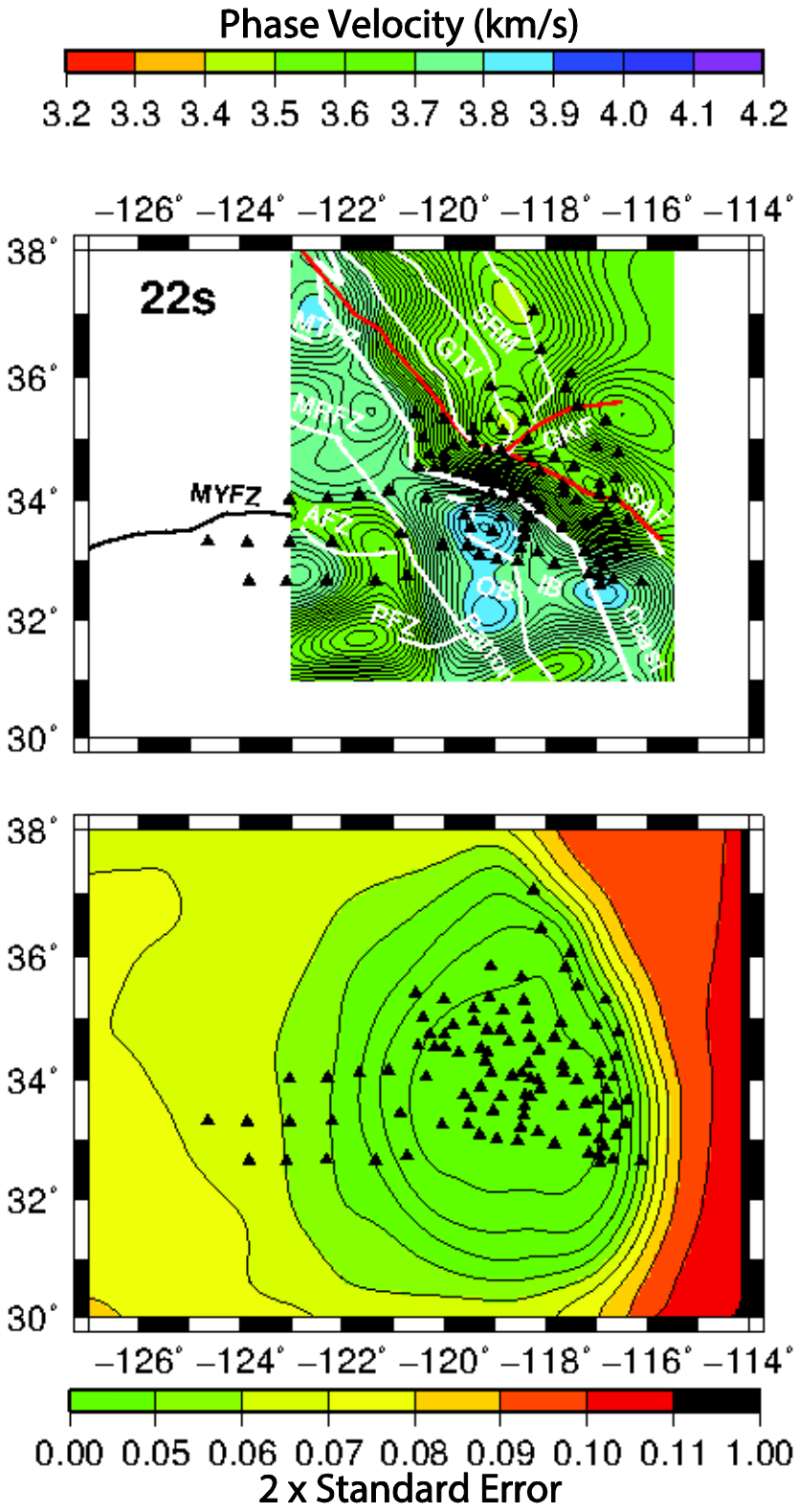
Phase Velocity (km/s)
3.2 3.3 3.4 3.5 3.6 3.7 3.8 3.9 4.0 4.1 4.2
−126° −124° −122° −120° −118° −116° −114°
38°
36°
34°
32°
30°
22s
MYFZ
SRM
GTV
GKF
SAF
AFZ
PFZ
0.00 0.05 0.06 0.07 0.08 0.09 0.10 0.11 1.00
2 x Standard Error

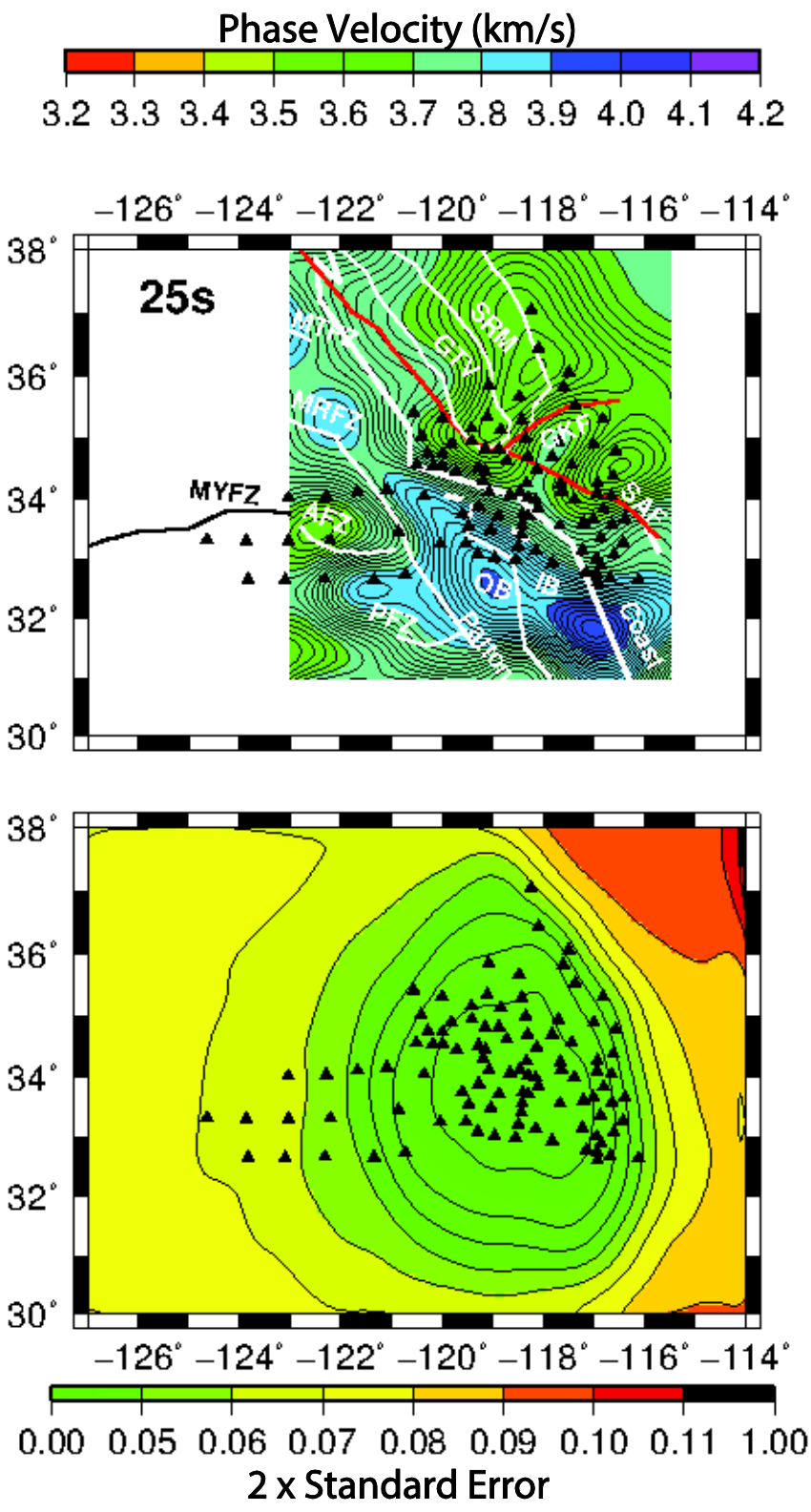
Phase Velocity (km/s)
3.2 3.3 3.4 3.5 3.6 3.7 3.8 3.9 4.0 4.1 4.2
−126° −124° −122° −120° −118° −116° −114°
38° 36° 34° 32° 30°
25s
MYFZ
MRFZ
GTS
SRM
RRG
SAF
AFZ
QB
JB
PFZ
Pamm
Crest
0.00 0.05 0.06 0.07 0.08 0.09 0.10 0.11 1.00
2 x Standard Error

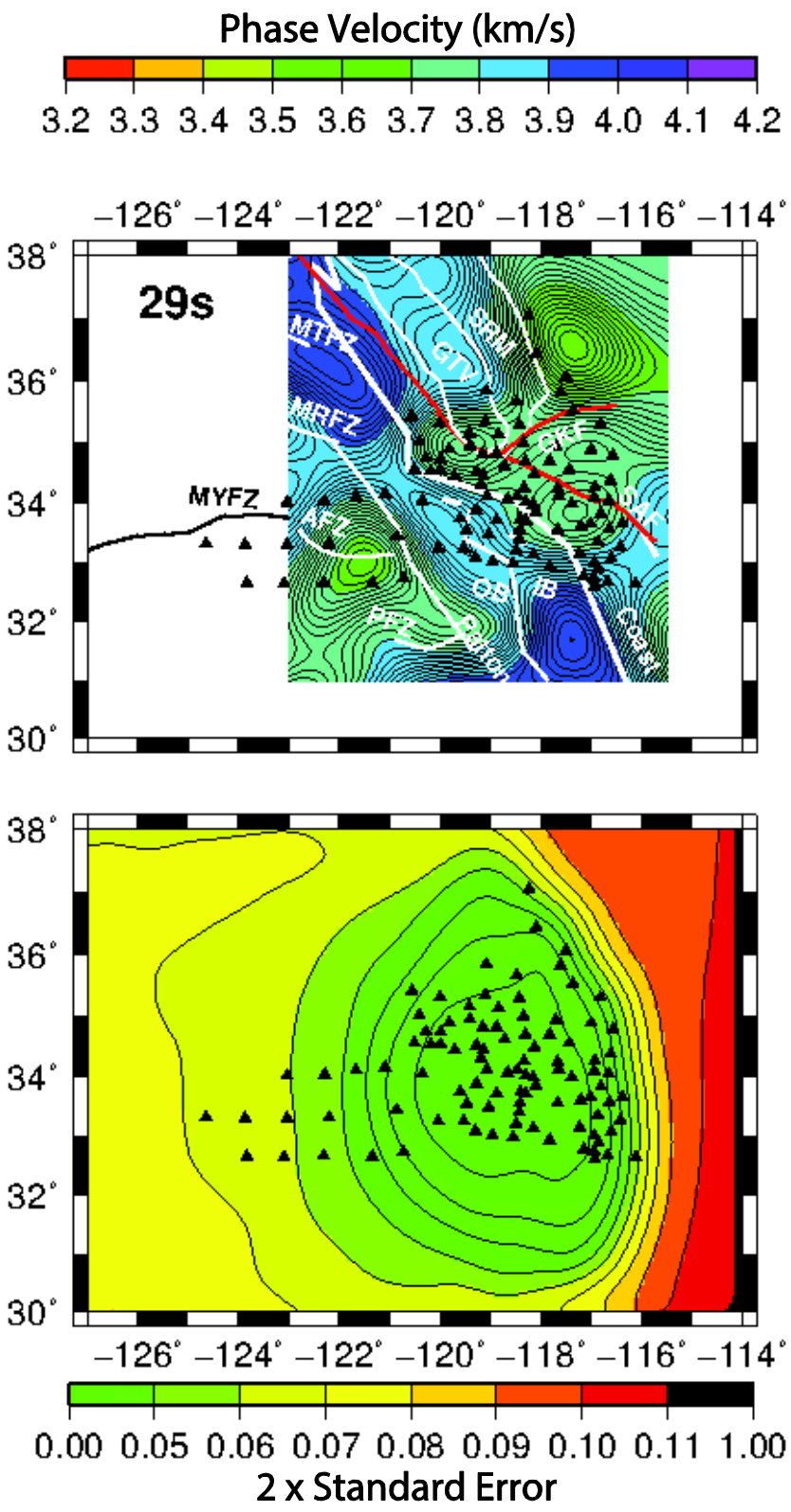
Phase Velocity (km/s)
3.2 3.3 3.4 3.5 3.6 3.7 3.8 3.9 4.0 4.1 4.2
−126° −124° −122° −120° −118° −116° −114°
38° 36° 34° 32° 30°
29s
MTFZ
MRFZ
MYFZ
AFZ
GTV
SRM
CTF
SAF
OSF
IB
PFZ
Coast
0.00 0.05 0.06 0.07 0.08 0.09 0.10 0.11 1.00
2 x Standard Error

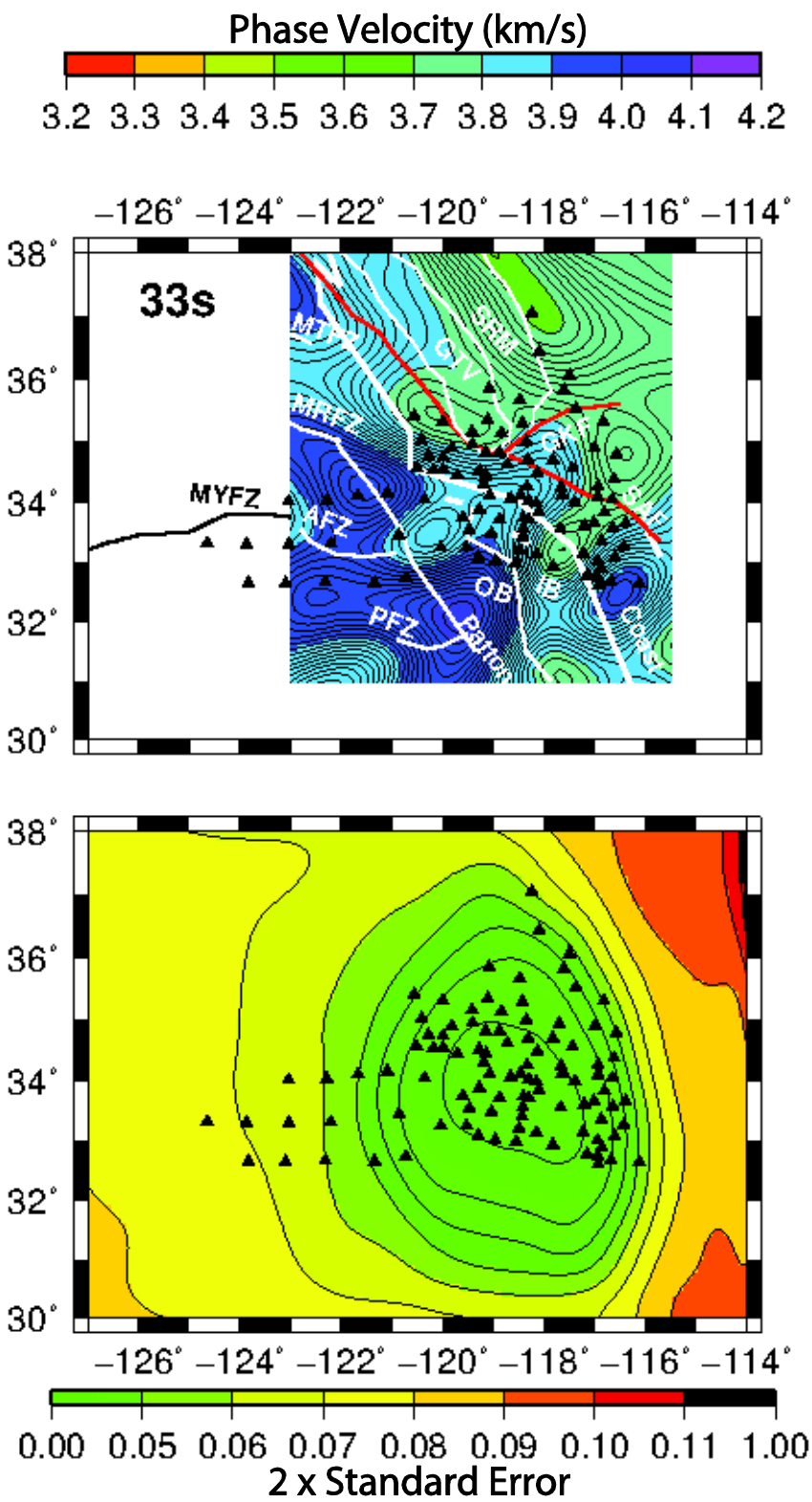
Phase Velocity (km/s)
3.2 3.3 3.4 3.5 3.6 3.7 3.8 3.9 4.0 4.1 4.2
−126° −124° −122° −120° −118° −116° −114°
38° 36° 34° 32° 30°
33s
MTFZ
MRFZ
MYFZ
AFZ
PFZ
CTV
SRM
OB
IB
Parton
0.00 0.05 0.06 0.07 0.08 0.09 0.10 0.11 1.00
2 x Standard Error

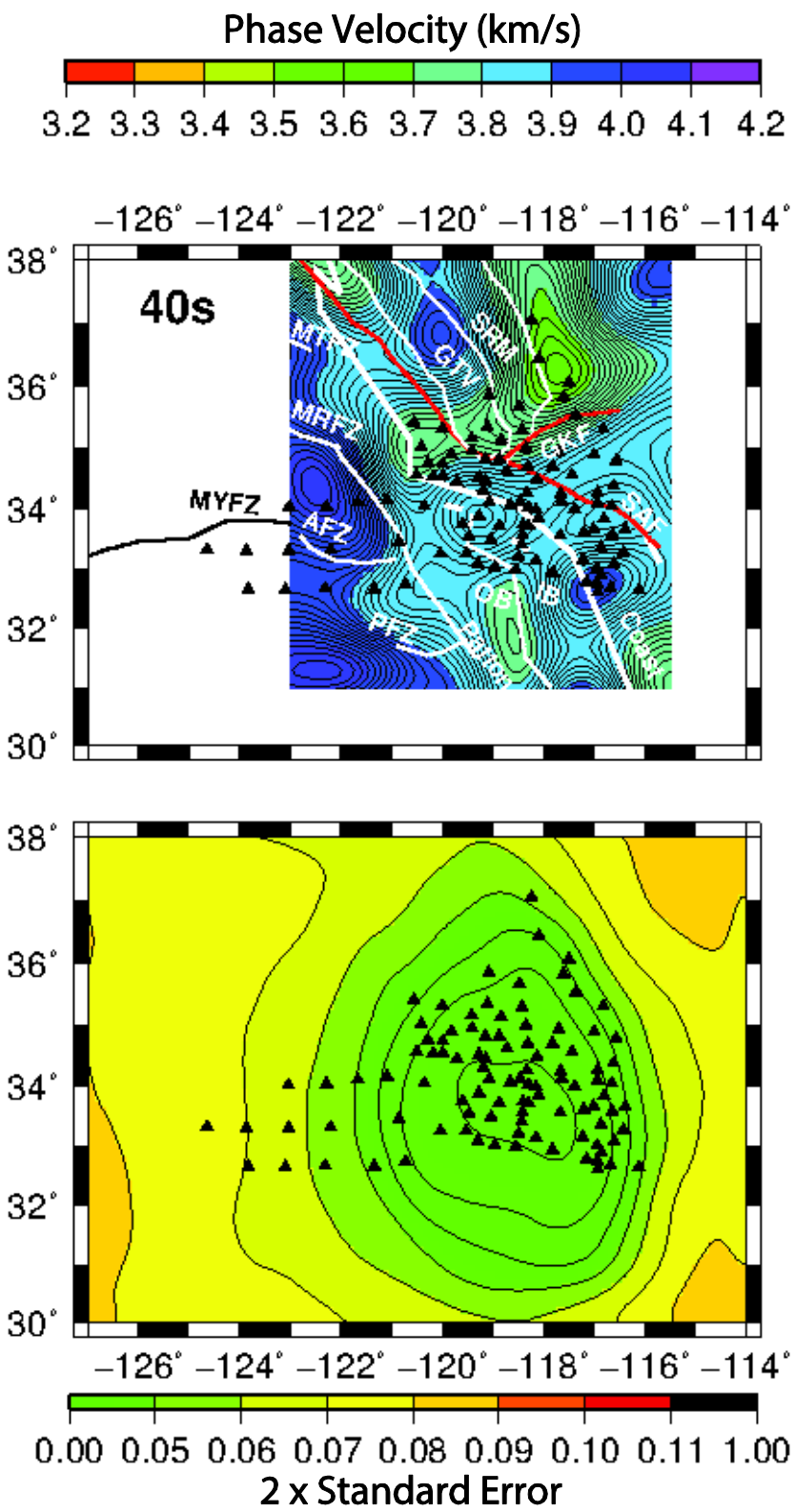
Phase Velocity (km/s)
3.2 3.3 3.4 3.5 3.6 3.7 3.8 3.9 4.0 4.1 4.2
−126° −124° −122° −120° −118° −116° −114°
38° 36° 34° 32° 30°
40s
MYFZ
AFZ
MRFZ
PFZ
CTV
SRM
CKF
SOF
0.00 0.05 0.06 0.07 0.08 0.09 0.10 0.11 1.00
2 x Standard Error

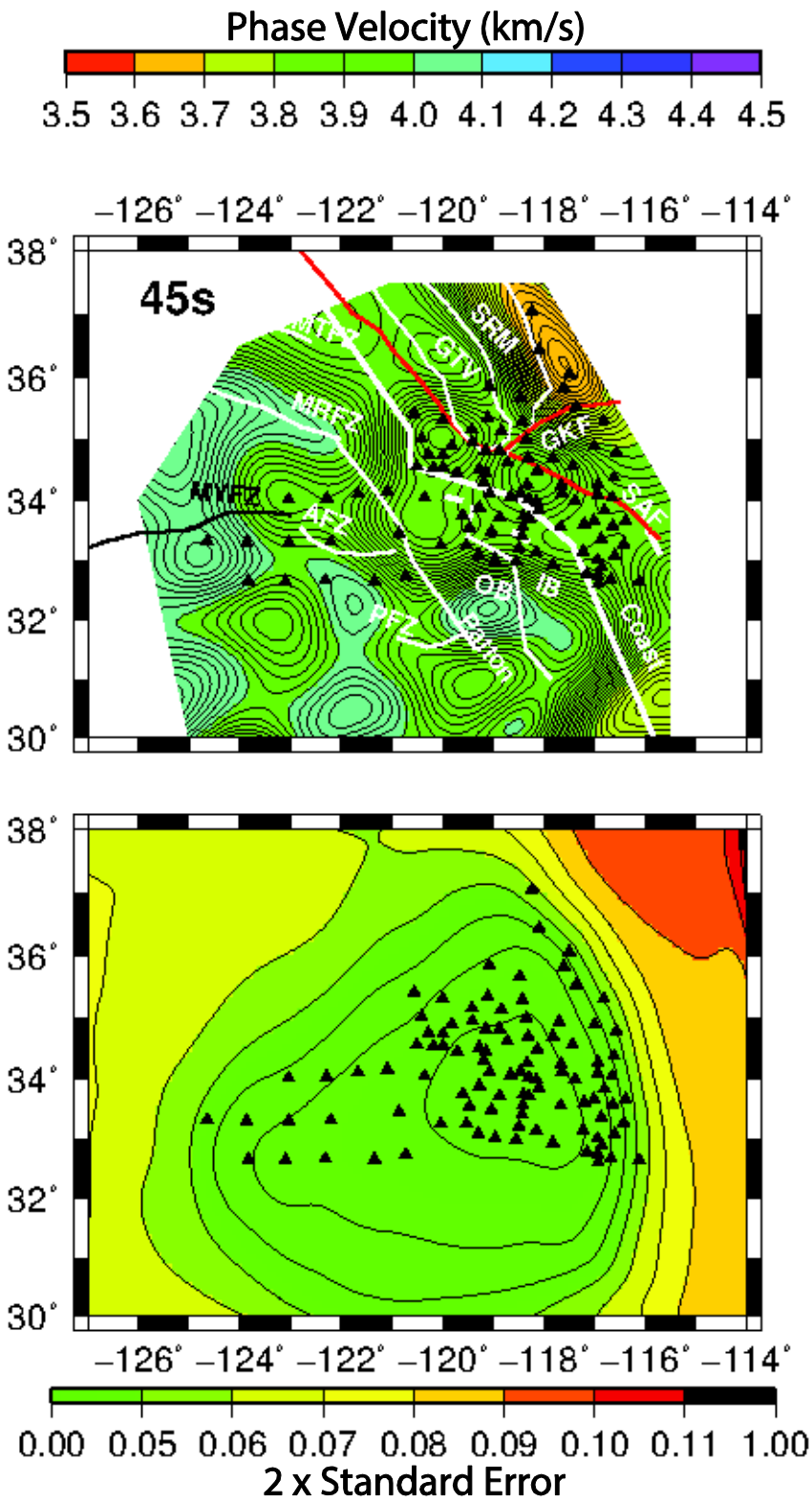
Phase Velocity (km/s)
3.5 3.6 3.7 3.8 3.9 4.0 4.1 4.2 4.3 4.4 4.5
−126° −124° −122° −120° −118° −116° −114°
38° 36° 34° 32° 30°
45s
SFM
GKF
MYFZ
AFZ
PFZ
Coast
0.00 0.05 0.06 0.07 0.08 0.09 0.10 0.11 1.00
2 x Standard Error

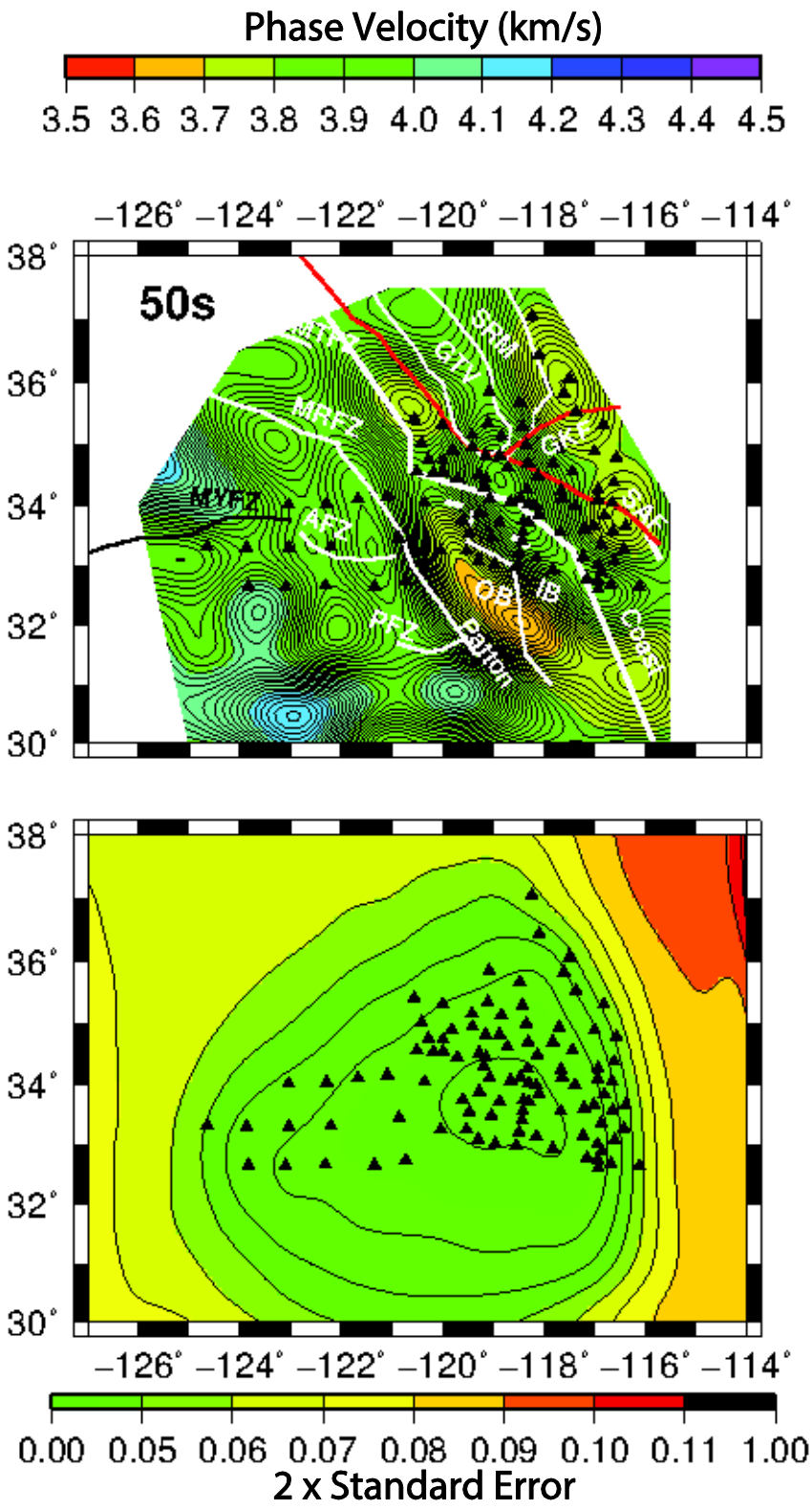
Phase Velocity (km/s)
3.5 3.6 3.7 3.8 3.9 4.0 4.1 4.2 4.3 4.4 4.5
−126° −124° −122° −120° −118° −116° −114°
38° 36° 34° 32° 30°
50s
MYFZ
MRFZ
AFZ
PFZ
Parton
OB
IB
Coast
GFZ
SAF
0.00 0.05 0.06 0.07 0.08 0.09 0.10 0.11 1.00
2 x Standard Error

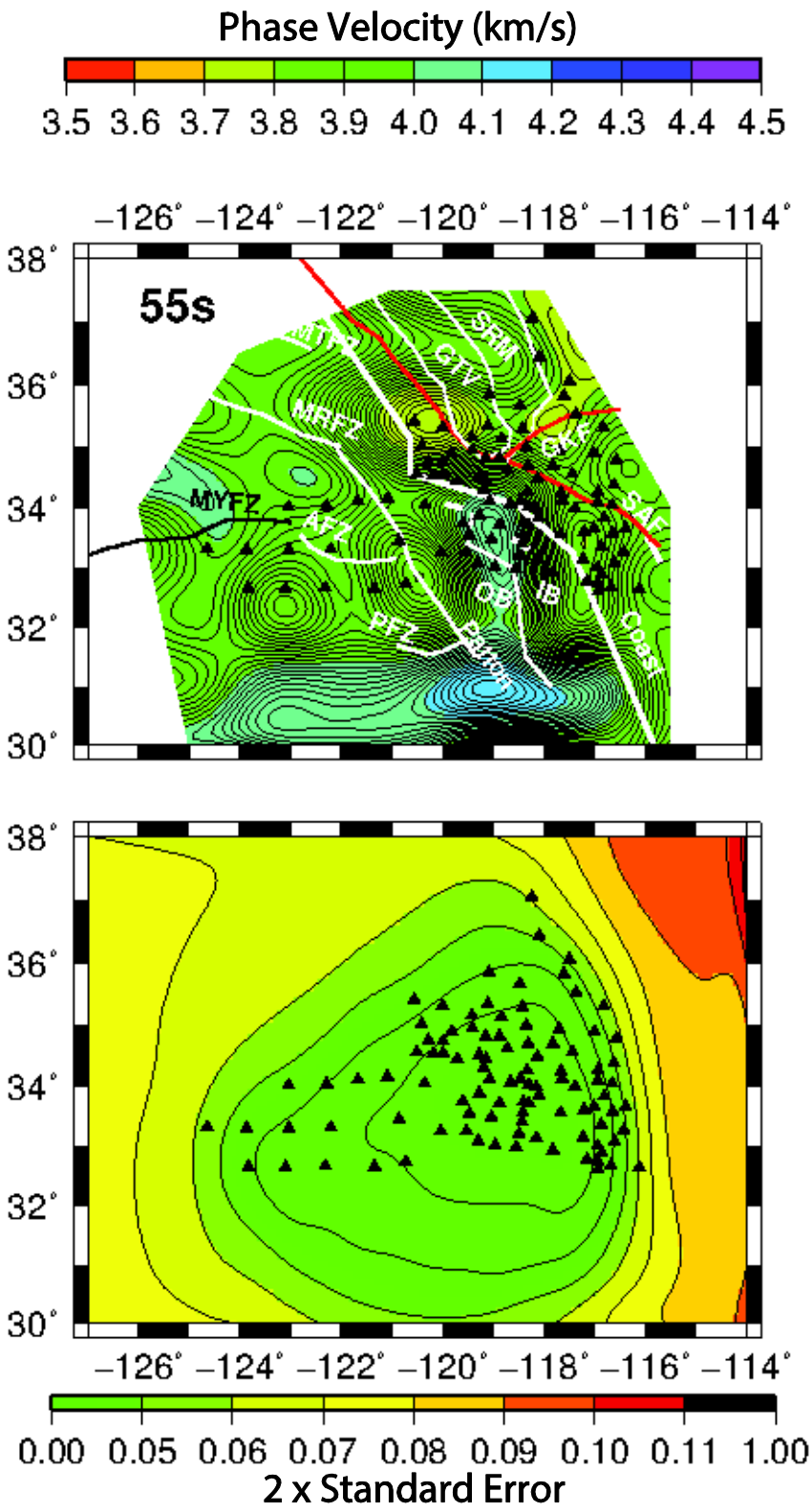
Phase Velocity (km/s)
3.5 3.6 3.7 3.8 3.9 4.0 4.1 4.2 4.3 4.4 4.5
−126° −124° −122° −120° −118° −116° −114°
38° 36° 34° 32° 30°
55s
MYFZ
MRFZ
AFZ
PFZ
CTV
SRM
SAF
IB
Coast
0.00 0.05 0.06 0.07 0.08 0.09 0.10 0.11 1.00
2 x Standard Error

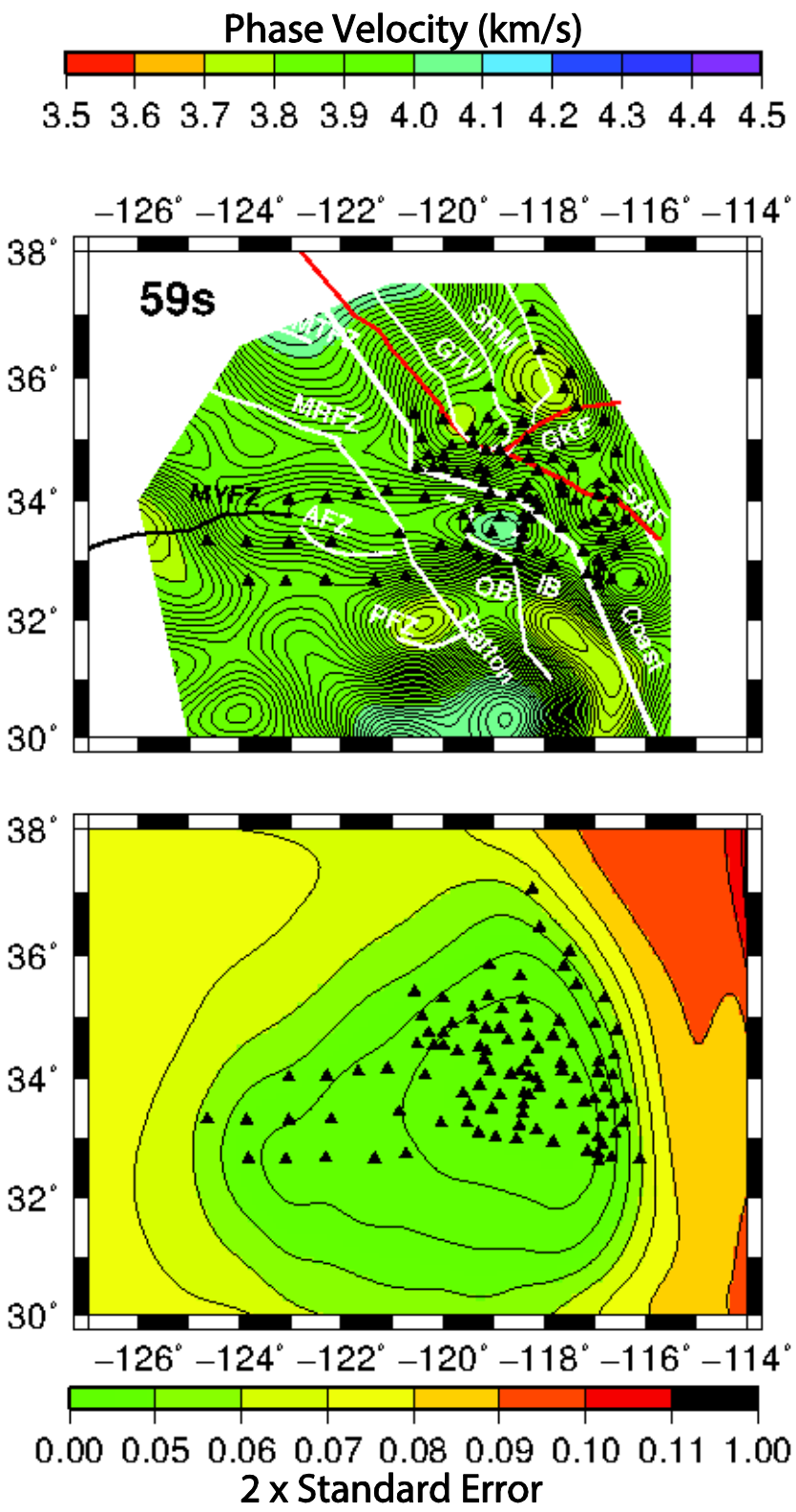
Phase Velocity (km/s)
3.5 3.6 3.7 3.8 3.9 4.0 4.1 4.2 4.3 4.4 4.5
−126° −124° −122° −120° −118° −116° −114°
38° 36° 34° 32° 30°
59s
MYFZ
AFZ
MHFZ
CTV
SRV
CKF
SRI
OB
IB
PRV
Parton
Coast
0.00 0.05 0.06 0.07 0.08 0.09 0.10 0.11 1.00
2 x Standard Error

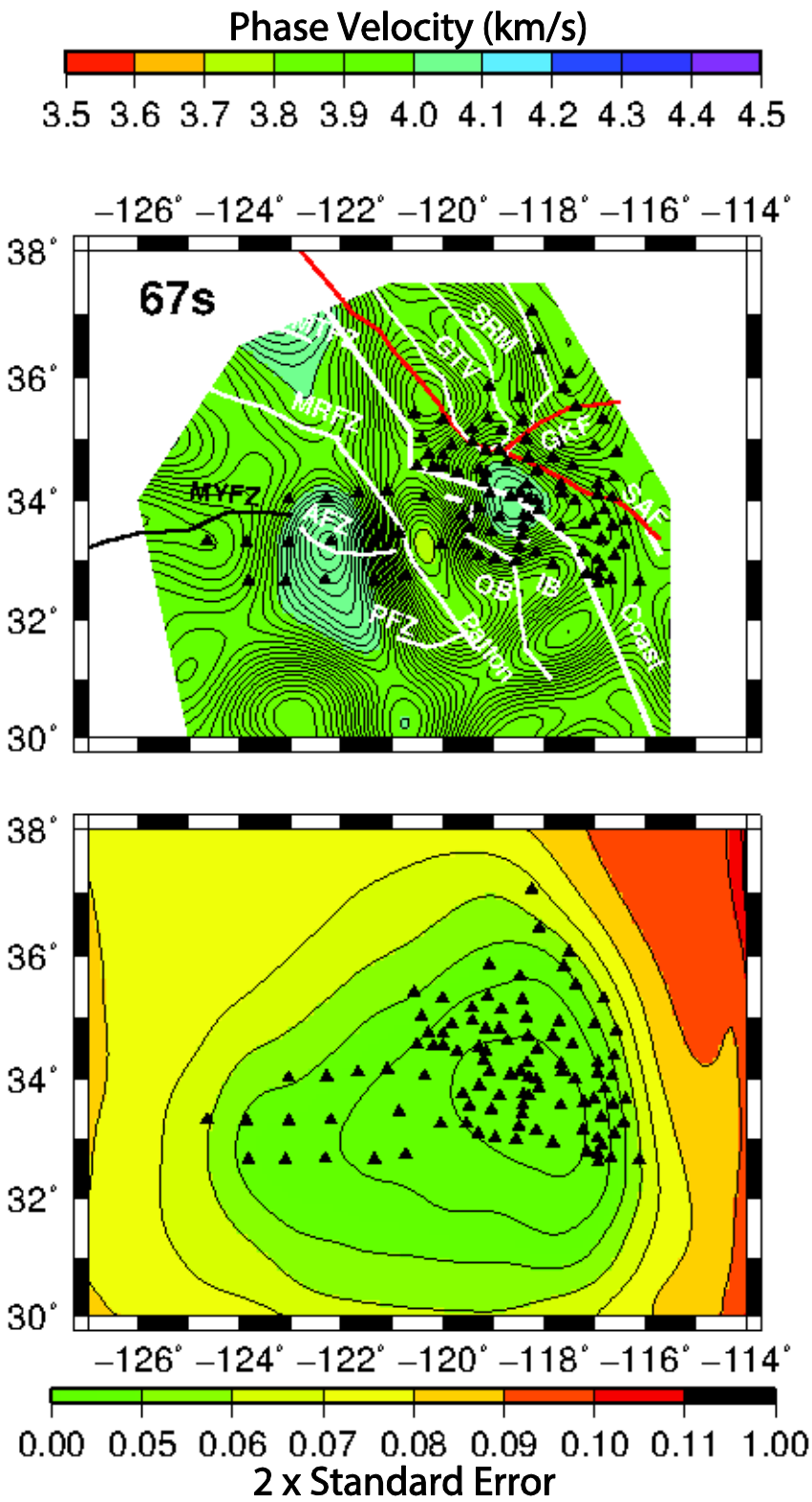
Phase Velocity (km/s)
3.5 3.6 3.7 3.8 3.9 4.0 4.1 4.2 4.3 4.4 4.5
−126° −124° −122° −120° −118° −116° −114°
38° 36° 34° 32° 30°
67s
MYFZ
MRTP
ETY
SRM
GRF
SAF
PFZ
Coast
0.00 0.05 0.06 0.07 0.08 0.09 0.10 0.11 1.00
2 x Standard Error

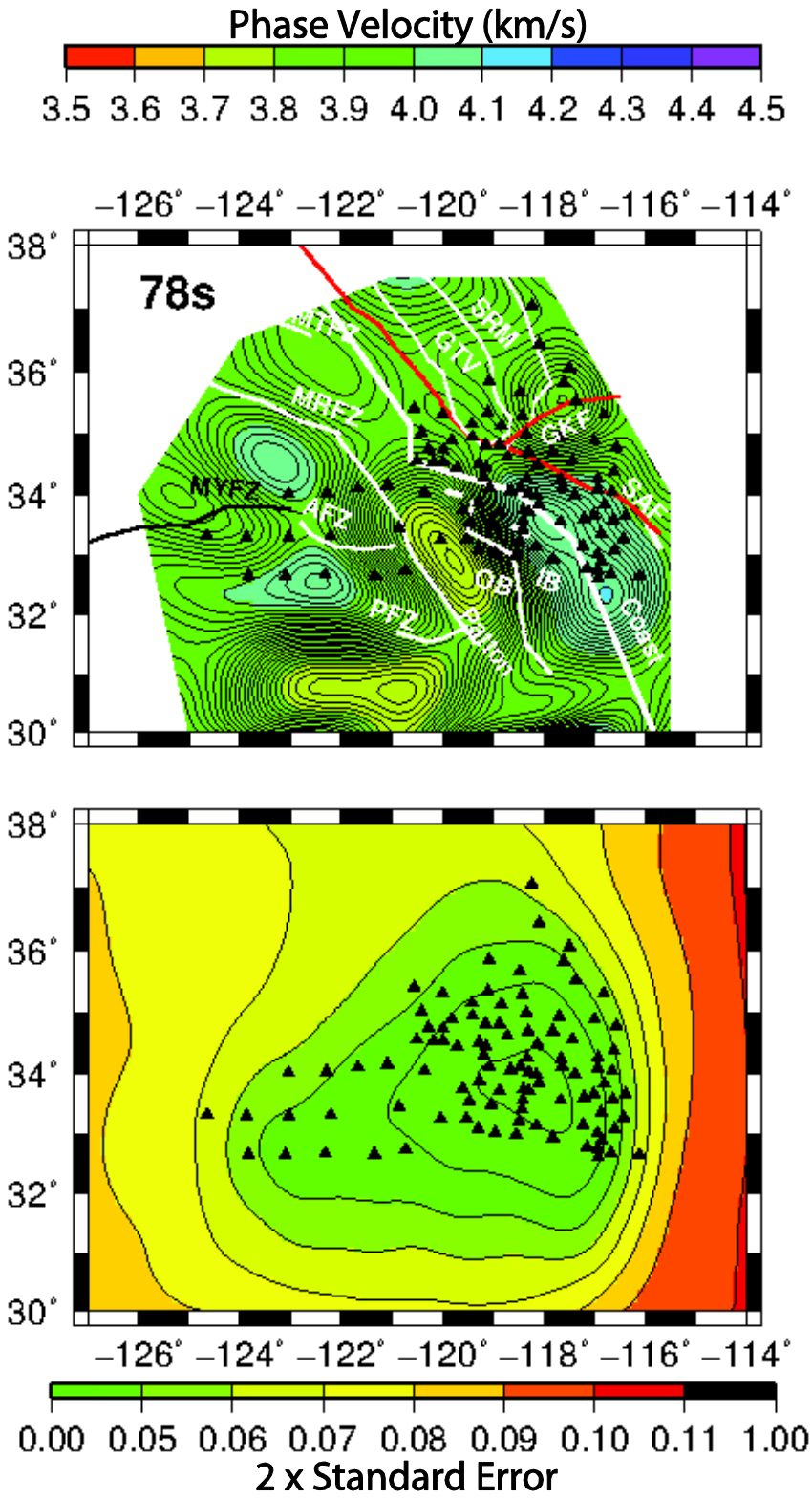
Phase Velocity (km/s)
3.5 3.6 3.7 3.8 3.9 4.0 4.1 4.2 4.3 4.4 4.5
−126° −124° −122° −120° −118° −116° −114°
38° 36° 34° 32° 30°
78s
MTFZ
SPM
GTV
MRFZ
GFF
MYFZ
ARZ
SAF
GB
IB
PFZ
Coast
0.00 0.05 0.06 0.07 0.08 0.09 0.10 0.11 1.00
2 x Standard Error

Appendix C: Seismograms

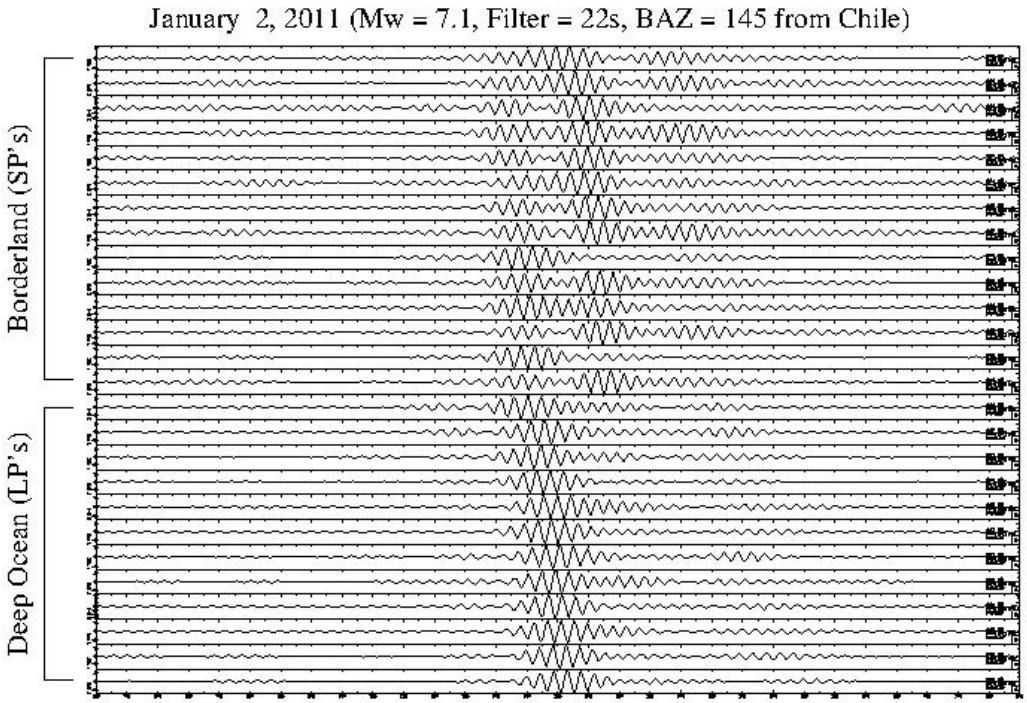

Figure C1: Seismograms filtered at 22s are shown for an event which originates from a SE back-azimuth (from Chile). The waveforms are notable different as they cross the Borderlands (top) compared to observations at more distant instruments in deeper water (bottom). This complex structure is likely due to scattering and multipathing through the sharp jumps in crustal structure between the continent, Borderland, and deep ocean sea floor We will investigate with this is causing distortion of the Rayleigh wave across the continental margin.

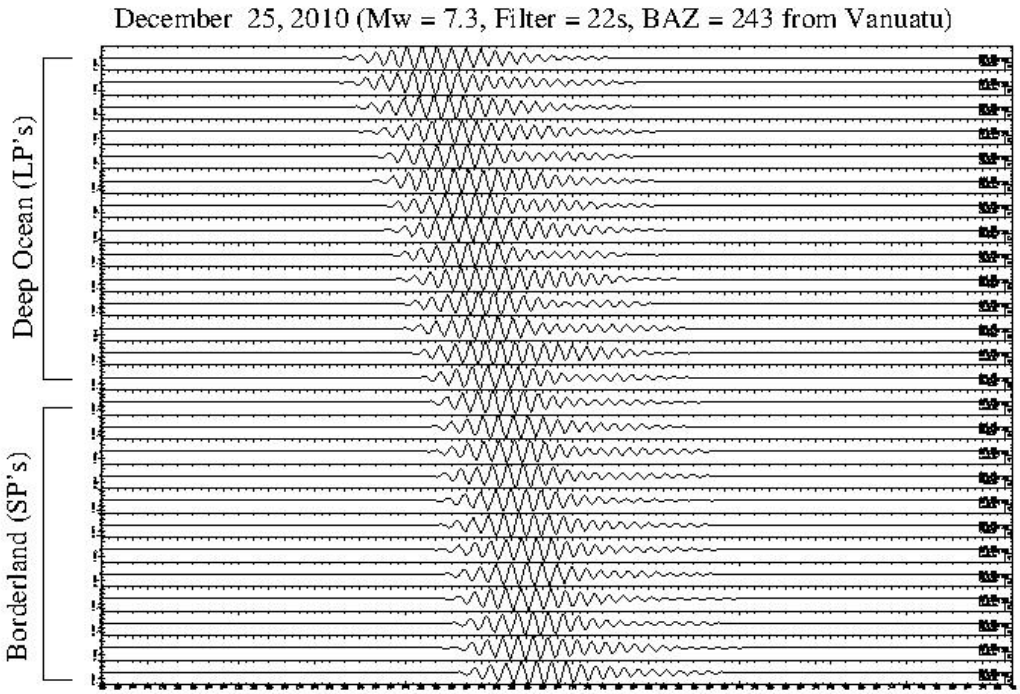

Figure C2: Seismograms filtered at 22s are shown above for our array. This event which originates from a SW backazimuth (from Vanuatu) displays normal moveout from the nearest (top) to the farthest station (bottom). The waveform of the Rayleigh wave is consistent across all Long period (LP) and Short period (SP) instruments.

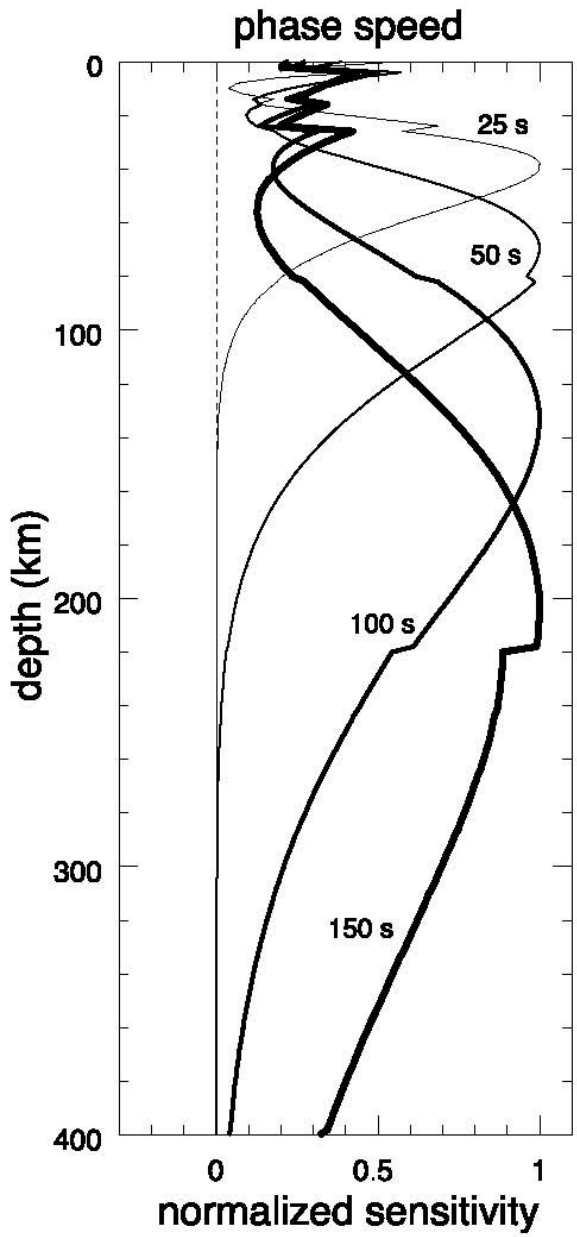

Figure C3: Rayleigh Wave Sensitivity to Earth Structure. Sensitivity kernels for periods of 25 s, 50 s, 100 s and 150 s. Each period has a peak sensitivity where this is 4/3 period. Each adjacent period has overlapping sensitivity within adjacent layers.